Universidad Politécnica de Madrid
Escuela Técnica Superior de Ingenieros Navales
Departamento de Arquitectura, Construcción y Sistemas Oceánicos y Navales

AMPLITUDE, FREQUENCY AND SYNCHRONIZATION ANALYSIS OF TENSION-LEG PLATFORMS UNDER VORTEX-INDUCED VIBRATION

Jerónimo Domingo Guijarro.
M. Sc. In Naval Architecture

Ph.D. Thesis

Supervisor: Prof. Luis Pérez Rojas
Ph.D. in Naval Architecture
Professor in Ship Theory

2021

Tribunal designado por la Comisión de Doctorado de la Universidad Politécnica de Madrid, en su reunión del día……………..de………………………de 20……..

Presidente: ____

Vocal:____

Vocal:____

Vocal:____

Secretario:____

Suplente:____

Suplente:____

Realizado el acto de defensa y lectura de la Tesis el día…………de…………………de 20……
En la E.T.S.I./Facultad……………………..

Calificación………………………….

EL PRESIDENTE LOS VOCALES

I would like to dedicate this thesis to my parents and sister.

Declaration of authorship

I hereby declare that, except where specific reference is made to the work of others, the contents of this dissertation are original and have not been submitted in whole or in part for consideration for any other degree or qualification in this or any other University. This dissertation is the result of my own work and included nothing which is the outcome of work done in collaboration.

Jerónimo Domingo Guijarro

April 2020

Acknowledgements

I would like to acknowledge Prof. Luis Pérez Rojas for giving me quality supervision and support through these years.

I want to that Mr. Héctor R. Díaz Ojeda for providing me with immensely helpful advice for the article publishing procedure.

I would like to thank Mr. Juan Enríquez for allowing me to use the company computers during the time windows that current firm projects left free.

Also, the “Escuela de Doctorado”, with all the professors involved deserves a special acknowledgment.

Finally, I would like to thank Ms. Rosa María Cárdenas and Mr José Antonio Cubillas, for keeping me informed of all the administrative requirements that, as a partial time Ph. D student, I was out of the everyday information.

Abstract

Offshore wind energy has become an important energy source that is reducing the fossil fuel energy consumption and many nations oil dependence. One of the most promising solutions for installations on medium depths seas is the Tension Leg (TLEG) platform. These platforms are provided with tension-legs, cylinders under tensile stress, as their mooring system. The tension legs must be calculated to withstand Vortex-Induced Vibrations.

Vortex-Induced Vibrations are a high hazard phenomenon for these platform structures that can lead to their failure and destruction. It is an extremely complicated phenomenon that links both flow and structure behavior as, at every instant, the results of flow feedback the structure behavior as well as this last one does it with the flow. A special case of VIV is that called synchronization. Synchronization, or lock in, is a VIV case where the vortex spreading frequency and the structure oscillation frequency are equal.

This interaction between flow and structure makes the VIV to depend on several direct parameters: geometric as leg length and diameter, fluid dynamic as the flow velocity and structural as the leg material density and Young´s modulus.

Computational simulation has become the tool, out of towing tanks, to analyze legs or risers since commercial computational links between the commercial fluid dynamic codes and their respective commercial structure calculus codes were developed back in 2006.

Several works have been developed, still limited in comparison to the required ones to analyze such multi-parameter phenomenon. In fact, currently, all the works have focused on vary the Reynolds number, for a certain riser, in low value ranges and without analyzing the rest of parameters, not allowing the generalization of such results to other risers.

The present work has focused on analyzing VIV by computational methods in a higher Reynolds number range of a larger riser, moving all parameters closer to the ones experienced by real facilities, analyzing the occurrence of synchronization and the effect of Reynolds number and the Young modulus.

A summary of the main results is:

The results point out the dependence of the oscillation amplitude with the Reynolds number and flow direction, the relationship between the flow and oscillation frequency and the action of the induced tension and the significant synchronization in the rigid cylinder case. A energy balance and a preliminary qualitative analysis of similar risers are also presented.

Keywords

Vortex-Induced-Vibrations, Synchronization, FSI (Fluid-Structural Interaction), frequency spectrum, flow-induced tension.

Resumen

La energía eólica marina se ha convertido en una fuente de energía importante capaz de reducir tanto el consumo de combustibles fósiles como la dependencia de las naciones del petróleo. Una de las soluciones de mayor interés para instalaciones de profundidades medias es la plataforma de tension leg, o plataforma TLEG por tener este medio de amarre. Estos elementos deben ser calculados para soportar Vibraciones Inducidas por Vórtices, o VIV por su acrónimo.

Las Vibraciones inducidas por vórtices son un fenómeno que supone una amenaza para la integridad de la plataforma. Es un fenómeno complejo en el que los aspectos fluidodinámicos y estructurales están interrelacionados y, a cada instante, se retroalimentan mutuamente. Un caso especial de VIV es el llamado sincronización. La sincronización es el caso donde la frecuencia de desprendimiento de los vórtices y la frecuencia de oscilación de la estructura se hacen iguales.

Esta interacción entre el flujo y la estructura hace que las VIV dependan de varios parámetros directos: geométricos, como la longitud y el diámetro de la leg; fluidodinámicos, como la velocidad del flujo y estructurales, tales como la densidad del material del que la leg está construida y su módulo de Young.

Las simulaciones computacionales se han convertido en la otra herramienta disponible para analizar legs y risers, además de los canales de ensayo, desde la aparición en 2006 de las aplicaciones comerciales que conectaban los anteriormente desarrollados códigos de fluidodinámica y de cálculo de estructuras.

Se han publicado varios trabajos en dicho campo, todavía en número bastante reducido. De hecho, actualmente, todos los trabajos se han centrado en variar el número de Reynolds, para un determinado riser, dentro de rangos de valores bajos, sin analizar el resto de los parámetros e impidiendo la generalización de dichos resultados a otros risers.

En el presente trabajo se ha analizado, mediante métodos computacionales, un riser de dimensiones y rango de numero de Reynolds mayores, acercándose a los de instalaciones reales, analizándose la aparición de la sincronización, así como el efecto del número de Reynolds y del módulo de Young.

Un pequeño resumen de los resultados de esta tesis es:

Los resultados muestran la dependencia de la amplitud de oscilación con el número de Reynolds y la dirección del flujo, la relación entre el flujo y la frecuencia de oscilación y el efecto de la tensión inducida, así como que la sincronización es importante para el caso del cilindro rígido. Se muestra también un balance de energía y un análisis preliminar cualitativo de risers parecidos.

Palabras clave

Vibraciones inducidas por vórtices, sincronización, Interacción Fluido-Estructura, espectro de frecuencia y tensión inducida por el flujo.

TABLE OF CONTENTS

Nomenclature

Greek Symbols

ε Strain

σ Stress

μ Dynamic viscosity of the fluid

ρ Density

ω_b Beam phase angular velocity

ω_c Cable beam angular velocity

Acronyms/Abbreviations

A_{xrms}/D Dimensionless in-line mean square amplitude.

A_{yrms}/D Dimensionless crossflow mean square amplitude.

A_{xrms}^{max}/D Dimensionless maximum in-line mean square amplitude.

A_{yrms}^{max}/D Dimensionless maximum crossflow mean square amplitude.

C Structural damping

C_D Drag coefficient

CF Acronym of Cross Flow (direction perpendicular to flow).

C_L Lift coefficient

C_m Added mass coefficient.

D Riser diameter (in m).

E Young modulus

EI Flexural rigidity (product of Young modulus and riser section inertia moment)

F Force

f_n	n^{th} frequency of the riser oscillation spectrum (in Hz)
$f_{n,beam}$	n^{th} frequency of a non-tensioned beam oscillation spectrum (in Hz)
$f_{n,string}$	n^{th} frequency of a tensioned string oscillation spectrum (in Hz)
I	Riser section inertia moment
k	Wavenumber
KC	Keulegan-Carpenter number
L	Riser length (in m)
M	Mass (in kg)
m_a	Added mass.
IL	Acronym of In-Line (flow direction)
m^*	Mass ratio, defined as: $m/(\rho\pi D^2/4)$
N	Vibration mode number
R	Riser radius (in m)
Re	Reynolds number
S	Surface (in m^2)
S_T	Strouhal number
t	Instant time
T	Tension
V	Uniform flow velocity (in m/s)
x	In-line displacement (in m)
x_{mean}	Mean In-Line displacement
y	Cross-Flow displacement

List of figures and tables

Chapter 1

1. Introduction

1.1 Motivation

Offshore platforms have been paid attention since the development of sea oil and gas platforms already in the 40´s of the XX century. Besides, the appearance of the sea wind turbines has created another field for platform design, Bachynski and Moan (2012), Copple and Capanoglu (2010), Fulton et al. (2007) and Henderson et al. (2010).

Boosted by the energy dependency that forces energy sources import, basically oil and gas, Spain joined from the first moment to the development of the wind power. First, the land-based wind power, later the sea based. The current situation for year 2019 will be analyzed in subchapter 1.2.

The offshore wind-power sector started to develop at shallow sea zones, where the wind turbines were just installed at the top of a mast fixed at the sea bottom. The sea shore where this can be done is a sea near the shore with small shore slope where, far away from the coast, the depth is still not large. The depth limit for wind-turbines clamped to sea bottom is 60 meters, Garrido (2015). But, as these locations are quite limited and have been already used, the need to develop wind turbines able to be installed at increasing deeper depths has erased. Such need has led to the design of different wind turbine solutions, solutions that will be shown and described in subchapter 1.3.

The increase of wind turbine installation depth produced the impossibility of clamping the wind turbine mast into sea bottom as masts would be of technical unaffordable length. Hence, the need of wind turbine installation in a platform appeared. But, with installation of wind turbines in platforms arose some technical challenges. These challenges are due to the limitations on movement amplitude and accelerations values of the blades and electric generators which are intrinsically linked to a dynamic system as a moored platform, Bachynski and Moan (2012), Fulton et al. (2007). Furthermore, the installation of blades and the generator at high positions increase the movement and acceleration amplitudes.

Besides, these technical requirements of limiting movements and accelerations must be fulfilled together with a main economical requirement –the kWh price cannot be as high as that produced from an oil barrel-. The requirement of a low kWh price leads to a need for reducing the costs of construction and maintenance of the structures, reducing material amount, etc. EWEA (2009), IRENA (2012).

The reduction of material amount can be accomplished just only with a better knowledge of the phenomena involved in the platform performance, to adjust the design safety factors.

Structural calculations to design the platform structure to withstand its own weight and located loads (auxiliary equipment weight) is a well-developed engineering field. That is not the case of structure vibrations and, more specifically, the Vortex Induced Vibrations (hereafter, VIV). This phenomenon consists of the appearance of vibrations in the structure due to the vortex shedding in an alternative way from the two extremes of the structure section diameter perpendicular to flow direction, as seen firstly by Von Karman, Blevins (1984). The pressure field upon the structure section due to this vortex spreading results in an alternative oscillating force upon the structure in both the flow direction and the cross directions. The oscillating nature of this force produces a self-sustained oscillating movement of the structure which can lead to its failure due to fatigue.

The VIV phenomenon in water has been analyzed in several research works in towing tanks and by computational methods, works that will be surveyed in subchapter 2.2. However, all of them considered risers of small dimensions and low Reynolds number ranges. Hence, VIV in close to real size facilities immersed in flows with Reynolds number values near those these facilities will experience have not been analyzed by computational methods and very scarcely, and with limited published results, in towing tanks.

This has been chosen as **the aim of this work: to analyze the response to the VIV phenomenon of a riser of characteristics (size) and in conditions (Reynolds number) as closer to the real ones as possible** after reviewing the cases found in bibliography for the sake of verification and validation.

The Reynolds number increase will be achieved by two ways: increasing the diameter D of the platform legs and increasing flow velocity. The increase of leg diameter forces to also increase the leg length L, as the ratio L/D must remain within the usual ranges 400 – 500, Resvanis et al. (2012), Bourghet et al. (2011), Xiao and Wang (2016).

With this study scenario set, it is proceeded **to solve the problem of analyzing the VIV phenomenon in all the diverse variables that characterize it; these are: oscillation frequency, amplitude and mode, vortex shed frequency, and the analysis of the synchronization occurrence through the effects that characterize it: the oscillation and vortex shedding frequencies becoming equal and the lemniscate shaped orbital trajectories.**

Two aspects not defined in previous VIV knowledge are assessed: first, the link between flow, represented by the Reynolds number and, hence, dependent of the product of velocity and diameter VD, and the structure response to the drag force produced by the flow, which depends on the product of diameter and second power velocity V^2D. The drag force deforms the riser in the flow direction. Also, it is counteracted by a tension field in the riser. The VI-vibrations are superposed to the deformed and tensioned riser, not to the undeformed and non-tensioned one. But the vibration frequency changes with the tension (any string of a music instrument is a clear example of this effect). The link between the flow and the change of vibration frequency has been named as flow-induced force and has been analyzed in the present work. Also, an attempt has been done to analyze different models to estimate, with an acceptable accuracy, the leg structure frequency in an analytical way, without requiring time costly simulations or towing tank tests.

Finally, the different parameters affecting VIV are listed and a preliminary analysis of the effect of the tension leg construction material (through its Young modulus as parameter) has been assessed. Further work regarding this parameter would require experimental work to allow results validation.

To develop this analysis a computational method that solves both the fluid field and the structure analysis has been used. This method was done by using the commercial tool ANSYS.

Finally, in the last chapter **the main results will be summarized. These are: the similarities and differences between low Reynolds number and high Reynolds number cases and the different aspects of these last ones.**

1.2 Renewable energy sector in Spain

Renewable energies are all those which origins are a natural source. They are clean resources and almost inexhaustible. There is a wide variety of renewable energy sources and, roughly, the different types can be distinguished in function of the achieved final energy obtained from them: electric energy, thermal energy, and bio-combustibles. There are different sources of renewable energy, IDAE (2019) according to the natural resources used for the energy generation:

- Bio-combustibles.
- Biomass
- Wind energy
- High enthalpy geothermic
- Low enthalpy geothermic
- Marine: marine wind power (windmills installed offshore), tidal power (coast water dams filled during high tide and released during low tide) and wave power.
- Mini-wind energy: small wind power installations.
- Hydraulic
- Solar photovoltaic
- Solar thermal
- Solar thermoelectric

The renewable sector in Spain should be analyzed from two different points of view: first, the renewable energy production, and second, the market sector for Spanish companies as manufacturers of products and services abroad.

The renewable energies have an uneven distribution in Spain. In the electric sector, Spain has been a reference in the integration of renewable energies into the electric system. In this way, despite the last years stop, more than a 32% of the electricity produced in Spain was of a renewable type in the year 2017. Focusing on the renewable energy generation in the peninsula, it was the 33.7% with maxima of 42.4% (2014). Nevertheless, the lower use of renewable sources for both thermal and transport sectors made that the global energy percentage was much lower. In the global energy amount in Spain, the renewable energies decrease its percentage in the primary energy consume a 0.2% in 2016, returning to the 13.9% of the total and falling to the third position. This was the second consecutive decline in the analyzed historical series after the strong decrease of 3.1% in 2015.

In the rest of technologies different behaviors can be observed. Oil has maintained its first position during the whole studied period until current day. Nevertheless, a negative tendency in the oil consume has been detected as its percentage has decreased in a 5.3% during these last years. In the year 2016 it represented a 44.2% of the total with an increase of a 4.2% in respect to previous year, growth that exceeds the one occurred in 2015 and that supposes a change of tendency (all data from former two paragraphs from REE, (2018)).

The beginning of the electric car commercialization in 2019 (1.39% of the cars sold in Spain in 2019 were electric cars, caranddrive.com 18/06/2020) allows expecting the reduction of oil in the future.

Natural gas decreased its contribution along the series until the year 2016, when it grew a 1.8%, reaching a 20.3% of the total, REE (2018).

The nuclear energy showed growths and decreases alternating during these years, until reaching a 12.4% in the year 2016, with a year increase of 2.2%, REE (2018).

In the case of the coal, its share in the global primary energy production depends almost exclusively on the different policy developed by the different governments, without following any type of trajectory. A demonstration of such behavior was the growth of a 24% in the year 2015 followed by a decreasing of a 28% in 2016, representing an 8.5% of the total, REE (2018).

The consumption of primary energy in Spain decreased a 0.3% in 2016, REE (2018).

In terms of final energy, the renewable energies represented a 15% of the total consumption in 2016. This value increases in respect to 2015, when it reached a value of 14.7%, due to the increase of the renewable energies share, mainly the hydraulic energy for electricity generation, which increased from 8.4% in 2015 to 8.8% in 2016, which represents an increase of the 7.1%, REE (2018).

The thermal renewable technologies increase its contribution a 1.6%, representing a 6.3% of the total. The consumption of the final energy grew a 2.3%, together with the decrease of a 0.3% of the primary energy consumption, show the improvement in the energy use efficiency in Spain. The gross final energy, reference index for the fulfillment of the European objective of achieving a value of 20% in the year 2020, reached a 17,4% in 2015 (last complete available value), a figure near to that of 2014, when it supposed a 17,3%, REE (2018).

Spain has a remarkably high dependency on fossil combustibles. This energetic dependency from import registered its historical maximum in the year 2008, when it reached 81.3%. Thanks to the energy generation with renewable sources this dependency has been decreasing year by year until the year 2013. In the years 2014 and 2015 the dependency grew, due newly to a lower generation from the renewable sources. In the year 2016, again decreasing, reaching a 72.3 %. This means that, without considering the nuclear energy, which is regarded as native independently of which is the country of origin of the material used as combustible, our country is located near 20 percentage points above the average of the 28 countries of the European Union, which dependency reached a 54% in 2015, last available data, REE (2018).

The renewable technologies are fundamental tools to solve this serious problem of energetic dependency being clean energy sources and practically native all of them (Figure 1.1), Eurostad (2017).

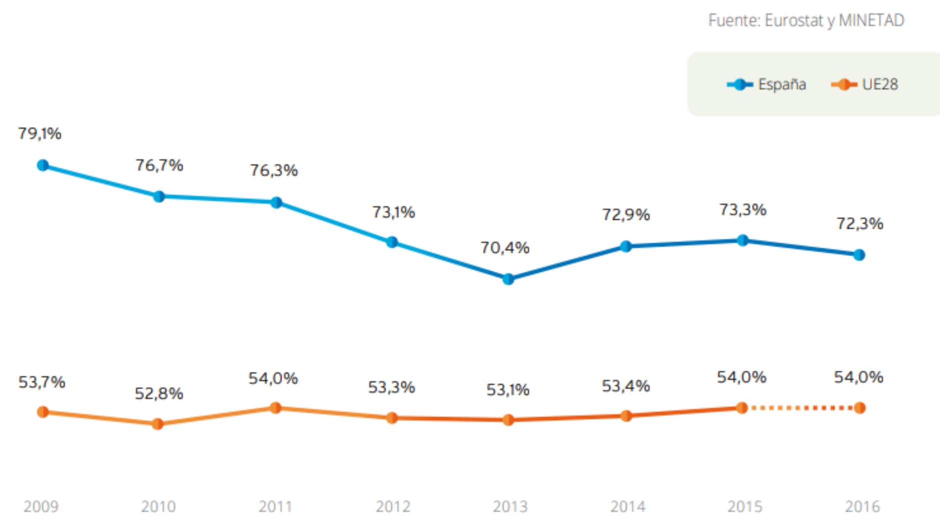

Figure 1.1: Spain and EU28 energy dependence, Eurostat (2017).

In the last years, the wind power has had an important settlement in Spain. This has occurred in installed power as well as in own-generated technology and R+D+I. In fact, Spain is one of the countries in the world with more wind-power kilowatts installed, IRENA (2019).

During the year 2011, the wind power energy supplied approximately a 16% of the electricity consumed in our country, with an installed power over 21600 MW.

During the year 2011, another 1050 MW of new power were installed, which represented a growth of a 5.1% in respect to the former year, being in percentage the smallest growth in the history of the wind power technology in Spain.

The objective that is registered in the "Plan de Energías Renovables 2011-2020" is of 35750 MW. From this whole amount, 750 MW correspond to marine wind-power, IDEA (2011), so an important development in terms of installed power is still to be done. Objective that, finally, will not be achieved, as 2018 ended with a 17.3% of renewable energy power, even decreasing from the 17.5% of 2017, Energías Renovables, (2019).

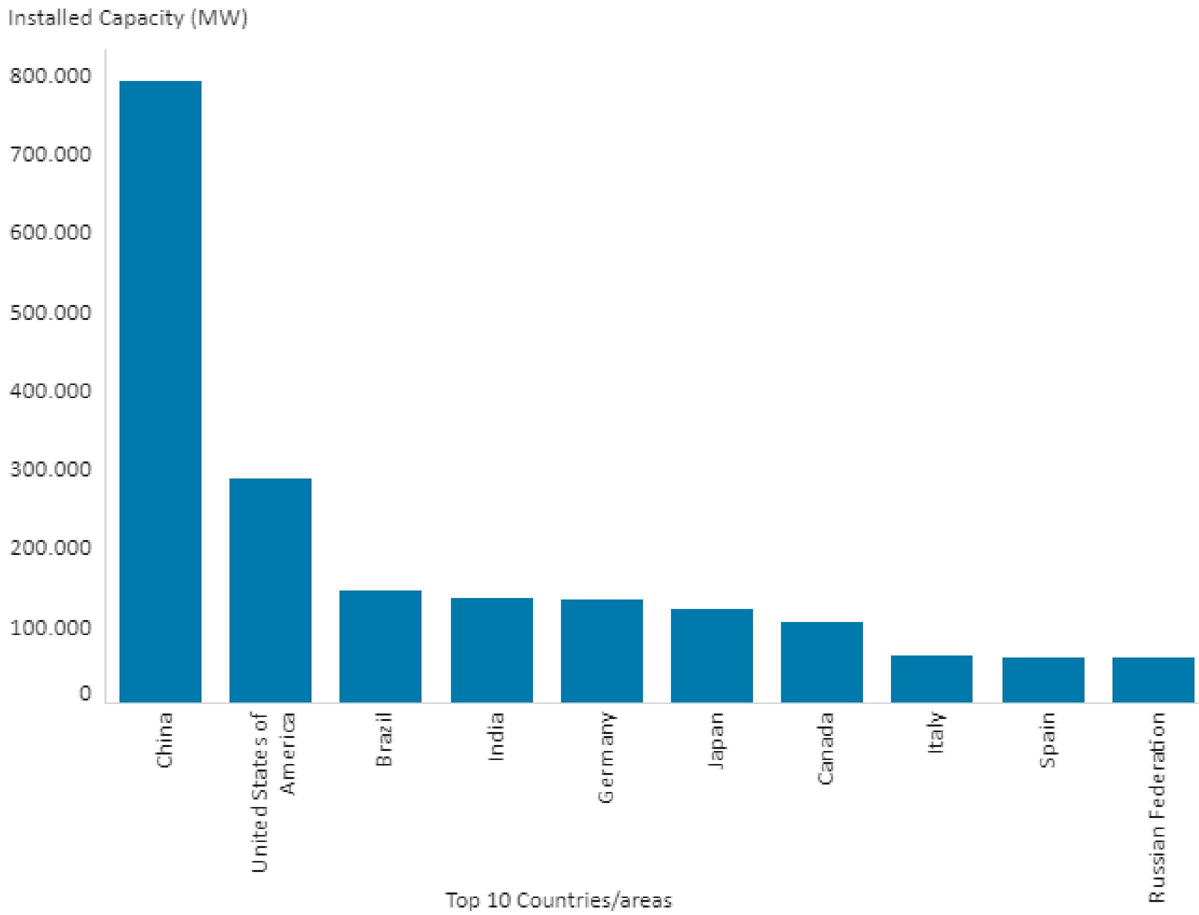

Figure 1.2: Renewable energy installed capacity by country. IRENA (2019).

Figures 1.2 to 1.4 show: the renewable power installed by country (figure 1.2), the total wind power installed (figure 1.3) and offshore wind power (figure 1.4), respectively, with data of 2018, surveyed by IRENA in 2019. It is observed that Spain occupies the 9th in total renewable energy, the 5th in wind power and it is not between the 10 first countries in offshore wind power.

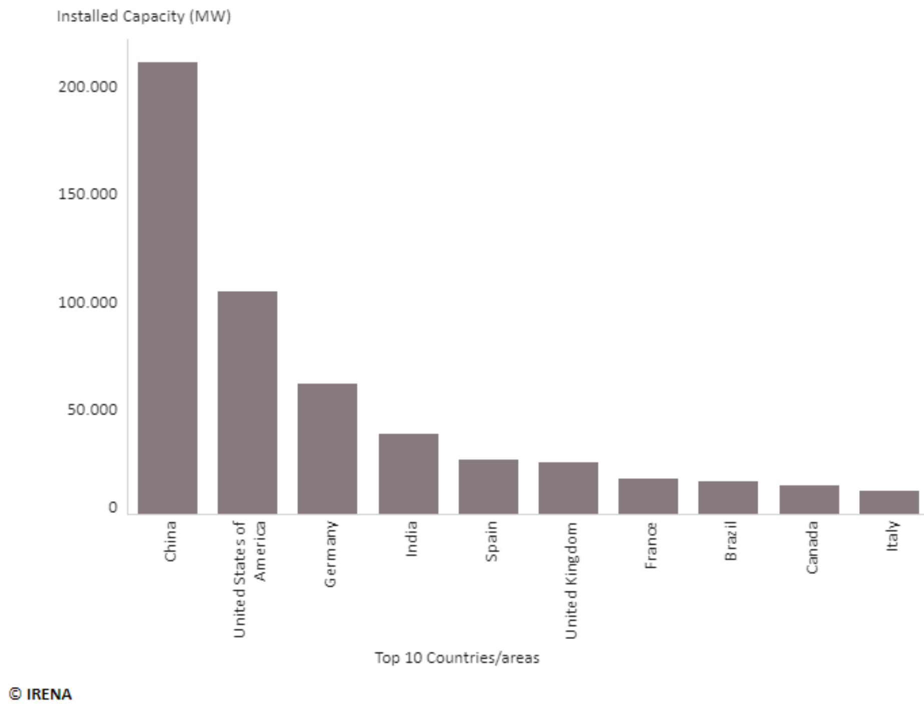

Figure 1.3: Wind power installed capacity by country. IRENA (2019).

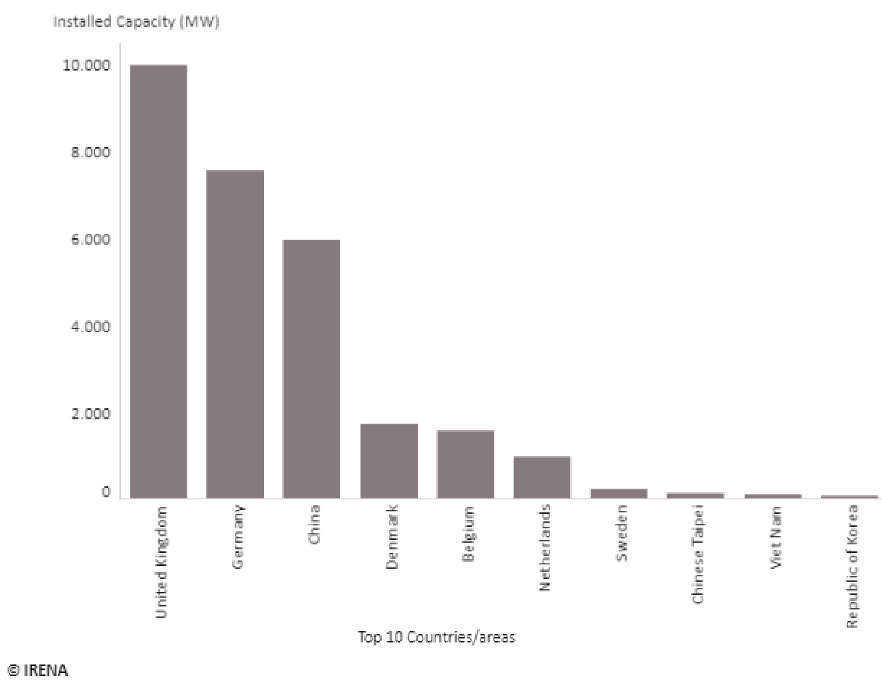

Figure 1.4: Offshore wind power installed capacity by country. IRENA (2019).

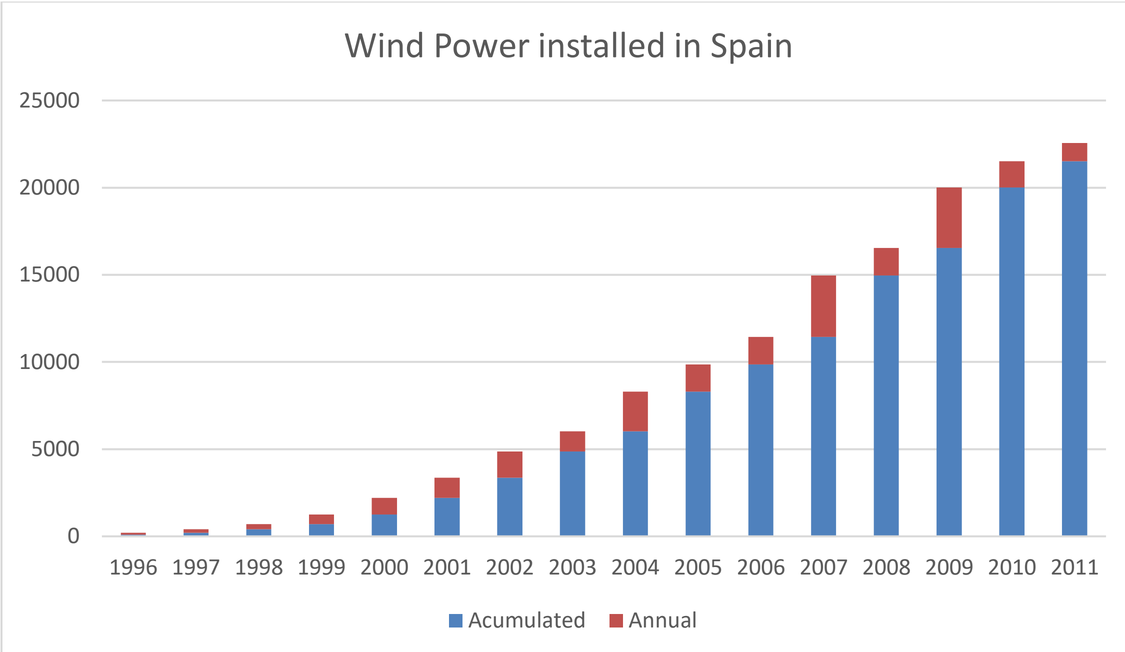

Figure 1.5 Wind power installed in Spain. Sources: CNE, MINETUR, REE and APPA.

At European scale, in the year 2011, the installed power was near 94 000 MW and, from them, 3800 MW were marine wind power, IRENA (2019).

In the range by countries Spain (23 GW) is in second position in the EU-27, meanwhile at worldwide scale is in fifth position, only behind China (221 GW), U.S.A. (96.4 GW), Germany (59.3 GW) and India (35 GW), IRENA (2019).

The marine wind power installation show advantages when comparing to inland installations, mainly, The Future of Energy (2016):

- The energy of the marine winds is higher than in the coast.
- Due to be located far from the coast, the visual and acoustic impacts are lower than in the inland wind power installation. This allows a greater exploitation of the existing wind power resource, with larger machines and the use of more efficient wing geometric

model. In the same way, the lower surface roughness at the sea favors the use of lower towers.

- It supposes a larger employment creation in the stages of manufacturing, installation, and maintenance, due to the higher complexity during installation and exploitation.
- Possibility of integration with other marine installations.

Nevertheless, these installations show also important drawbacks in respect to the inland ones, which are limiting its development:

- Inexistence of electric infrastructures,
- More severe ambient conditions,
- More difficult and expensive evaluation of the wind power resource and
- Higher inversion ratios and exploitation costs, needing specific technologies for the construction and foundations, transport, and installation at high sea, launching of submarine electric networks and operation and maintenance works.

The wind generator power per machine is higher at sea than that of the inland turbines. Meanwhile the inland ones, limited due to topography and transport have an averaged consolidated power per machine near 3 MW with a clear tendency to increase the rotor diameter to obtain a better exploitation of the installation, at sea, the new development for marine wind power fields are composed by wind generators of unitary power over 5 MW. A 10 MW wind turbine has been installed in the Canary Islands in April 2019. Following this installation, the company Equinor would invest 860 M€ to reach the 200 MW of installed power, webpage of REVE (Revista Eólica y del Vehículo Eléctrico) (2019a).

Possibly, the main challenge for the high sea installations remains being to reduce the costs of the foundations, of which several systems exist: mono-pilot, tripod, of gravity and floating.

The mono-pilot installations are the most used for waters of medium depth (until 25 meter), the gravity installations are used with low depths (less than 5 meter) and the tripod installation for higher depths (until 50 meter), webpage of Iberdrola (2019).

Primary energy consumption

	2015		2016		2016/2015
	(ktep)	Percentage (%)	(ktep)	Percentage (%)	Variation (%)
COAL	**13686**	**11,1**	**10442**	**8,5**	**-23,7**
PETROLEUM	**53711**	**43,2**	**54663**	**44,2**	**2,7**
NATURAL GAS	**24553**	**19,9**	**25035**	**20,3**	**2,0**
NUCLEAR	**14934**	**12,1**	**15260**	**12,4**	**2,2**
RENOWABLE ENERGIES	**16644**	**13,5**	**17213**	**13,9**	**3,4**
Hydraulic	**2420**	**2,0**	**3130**	**2,5**	**29,3**
Other renowable energies	**14224**	**11,5**	**14083**	**11,4**	**-1,0**
Wind power	4242	3,4	4205	3,4	-0,9
Biomass and waste	5801	4,7	5659	4,6	-2,5
Urban Solid Waste	252	0,2	243	0,2	-11,8
Biomass	5288	4,3	5185	4,2	-1,9
Biogas	262	0,2	231	0,2	-11,8
Biofuels	977	0,8	1023	0,8	4,7
Geothermic	19	0,0	19	0,0	3,1
Solar	3185	2,6	3177	2,6	-0,2
Photovoltaic	711	0,6	693	0,6	-2,4
Solar thermoelectric	2196	1,8	2190	1,8	-0,3
Solar thermal	277	0,2	293	0,2	5,8
NON RENOWABLE WASTE	**252**	**0,2**	**243**	**0,2**	**-3,7**
ELECTRIC BALANCE	**-11**	**0,0**	**659**	**0,5**	**-5863,8**
TOTAL	**123209**	**100,0**	**123485**	**100,0**	**0,2**

Figure 1.6. Spain primary energy consumption. Source: MINETAD/IDAE. Data of June 2017.

Spanish companies have also manufactured offshore technology for national and foreign markets. An important part of the sea wind park platforms of jacket type to be installed on the English cost of the North Sea have been built in Spain. Among the most important contracts are those of:

- Dong Energy: Denmark company for British market (signed May 2016), four jackets. El park has an area of 407 square kilometers, has already 174 turbines of 7 MW each developed by Siemens, Lavozdigital.es (2016).

- Tennet: German-Dutch company for the North Sea, sea wind park Dolwin 6 (signed July 2017). Lavozdigital.es (2017),

These contracts share the technologic developments used also in oil and gas platforms. This synergy allows that achieving offshore wind power contracts helps to also achieve oil and gas contracts and the other way around. Cases of oil and gas projects like those of wind power projects are:

- Statoil (from 2019, Equinor): Norwegian for Norwegian market, building an 8000-ton structure for the sea oil of Johan Sverdrup at the North Sea. (Signed October 2015), Lavozdigital.es (2020).
- Maersk Oil and Gas: Danish company, building two jackets for a gas installation at the North Sea, Lavozdigital.es (2020).

As a data of this industry development is worth to say that, only in the Asturias region, 50 companies manufacture for a value 5000 million Euro per year in the sea wind power field and keep 15000 employees, webpage of Energias Renovables (2018).

In floating wind power there was only one field, the Hywind, in Scotland, of 30 MW, property of Statoil (Norway) until the year 2019. Then, in the Canary Islands the first semi-submersible platform, 10 MW power, has been launched and it has been commissioned that, in the year 2025, a total of 200 MW of sea wind-power will be installed, webpage of REVE (Revista Eólica y del Vehículo Eléctrico) (2019b).

Hence, according to data, Spain has an important renewable energy sector that provides a high percentage of the consumed energy although still oil dependency is high, due basically by car fleet. However, electric car market started in Spain in 2019. The target is that this market would reduce oil consumption and pollutant emissions. To do so, electric energy generation must be increased.

1.3 Offshore wind technologies

Focusing on the technical items of sea wind generators, the main topic comes from the design and building up of a supporting structure of the wind turbines themselves. This structure must connect the generator in the surface with the sea bottom, that is, mooring it, and it must do it in a safe way, facing any sea condition that might appear, and in the most possible profitable way.

In the case of sea zones with shallow waters, the structures fixed due to gravity or clamped to the sea bottom as, in example, the jacket technology, are the indicated solutions, webpage of Iberdrola (2019).

But, to capture winds at higher speeds and during the longest possible time periods as well as to avoid the drawbacks of the near-to-shore wind-mill fields, it is necessary to move to deeper seas. In these seas the shallow water mooring solutions are not feasible from the economical point of view. The platforms must be of some floating type.

Such a challenge has led to the development of three different types of floating platforms, candidates to be the definitive solution: the spar platform, the semi-submergible platform, and the tension-leg platform.

1.3.1. Spar platforms

The spar buoy or spar platform consists of a steel or concrete cylinder that floats vertically, with low water plane area and ballasted with water and/or solid ballast which results in a weight-buoyancy stabilized structure with a large draft.

The first spar platform, the “Brent Spar” was designed to storage crude oil products and installed in the Brent Field in June 1976 and operated by SHELL. In the field of sea wind energy, it was used, for first time, for the pilot sea wind mill 2.3 MW Hywind Demo, property of Statoil (sold to Unitech in January 2019) and installed 10 km off the Norwegian coast at a 220-meter sea depth in September 2009. Its concept was used to install the first floating wind farm of 30 MW in Scotland waters. The figure 1.7 shows a representation of the Hywind generator, webpage of Equinor (2020).

The concept is quite simple. This type of platform gets stabilized due to its own weight being its gravity center located extremely low under the flotation center. Thus, it has a long righting arm and, hence, short oscillation periods and high accelerations. On the other side, the drag due to the sea tides is high as it presents a large frontal surface to them. The Hywind wind-generator is moored by means of catenaries.

A concrete-made design representing an important cost saving has been presented in the project of the platform WindCrete, webpage of Windcrete (2015).

Fig. 1.7 Hywind wind-generator of the spar type.

1.3.2. Semi-submersible platform

In this design, one single or several wind-generators are installed upon a semi-submersible floating platform. This type of platform is stabilized by means of floating columns, this is, a large value of displacement is obtained with large floating columns. The main advantage of this type of platform is its particularly good stability when facing waves. Figure 1.8 shows a semi-submersible platform with three columns and three wind-generators. There are many cases when only a single wind-generator is installed on a platform of this type. The semi-submersible platforms can be moored with catenaries or with tension legs. The first semi-submersible platform was installed 5 km off the coast of Aguçadora, north of Porto, Portugal at the end of

2012, with a power of 2.0 MW. It was a test plant to develop the Windfloat project, webpage of EDP (2020).

The success of the Aguçadora wind-turbine project promoted the Windfloat 25 MW project started to produce electricity in January 2020, located 20 km off Viana do Castelo in 100 m depth waters. Windfloat is a Portuguese-Spanish consortium with EDP being major owner (54.4%) and Repsol, the third with a 19.4%. Platform was built in El Ferrol shipyard from July to October 2019, webpage of NS Energy (2020).

Its main withdraw is that it is the most expensive type of the three. But, to avoid this disadvantage, they can be built with several turbines per platform, as in the case of the Spanish first floating wind power platform, installed in the seas of the Canary Islands in April 2019, which has installed two 6 MW turbines, REVE (Revista Eólica y del Vehículo Eléctrico) (2019b).

Fig. 1.8 Semi-submersible platform with the floating columns and three wind-generators.

1.3.3. Tension leg platform

This type of platform takes its name of its mooring lines, which are tension legs. In fact, this type of platform is a combination of the two formerly presented. In this case, a single wind-turbine is installed upon a low-drag column of spar type submersed totally or partially. In this design the platform (buoy and extensions) is designed to obtain enough floatability and to bear the total displacement of the system given the required pre-tension to the tether system. In figure 1.9 can be observed a model of tension leg platform.

An advantage of this platform is its low drag meanwhile its drawback is its design requirements to achieve a good stability against the heeling moment.

The first TLP floating wind turbine is operated since 2008. It is a 80-kW turbine installed 21 km off the southeast cost of Italy in waters 113-meter-deep and property of Blue H Technologies, Huber, F. (2008).

No production-scale TLP has yet been installed, but there are some developments carried out like the one led by IBERDROLA, webpage of Iberdrola (2014).

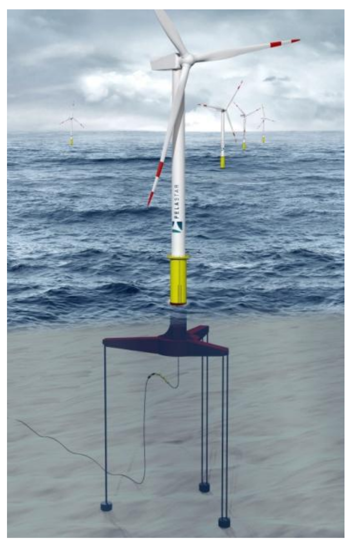

Fig. 1.9 Model of tension-leg platform.

1.4 Station keeping

To keep the position of the floating structures in the sea and retrain its motions and accelerations is known as station keeping and is a main aspect of its performance and integrity. Marine structures are exposed to environmental loads such as waves, winds, currents, and tides. The mooring system has as function to keep the structure in its position despite all the commented loads. In the offshore industry several types of mooring systems have been used successfully. Some of these types can be utilized also to wind generator floating platforms, in example the catenaries, the taut-leg and the tension leg, webpage of Offshore Mooring Lines (2020).

1.4.1. Catenaries system

The catenaries mooring system is the most used system in shallow waters. It gets its name from the shape of the free hanging line as its configuration changes due to vessel or platform motions. At the seabed, the mooring line lies horizontally; thus, the mooring line must be longer than the water depth. A image of the catenary system can be seen in figure 1.10.

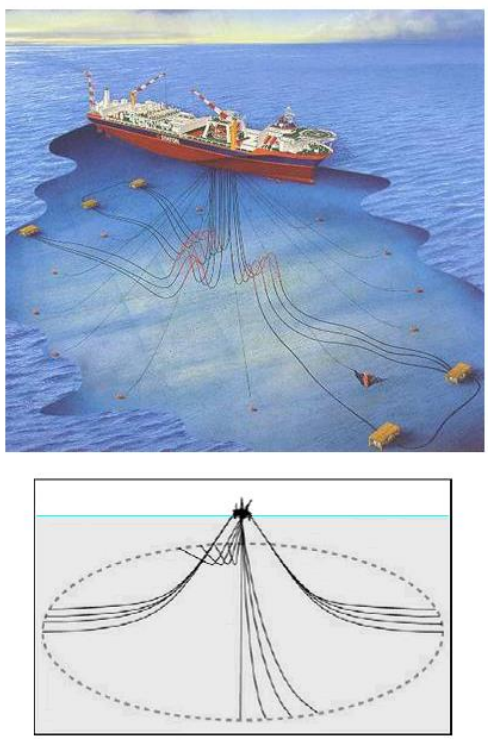

Fig. 1.10 Representation and scheme of catenaries mooring system.

Catenary lines get their restoring force through the weight of the chain or the steel shackles.

Increasing the length of the mooring line also increases its weight. As water depth increases, conventional catenaries systems become less and less economical.

The catenaries main drawback is the great area of sea bottom required, what is denoted as "footprint". For this reason, the small footprint mooring systems are preferred for marine wind-generator platforms. The system with smallest footprint is the tension-leg, webpage of Offshore Mooring Lines (2020).

1.4.2. Taut-leg system

The taut (stretched very tight) leg system or taut-leg system is characterized by the mooring lines being pre-tensioned until they are taut. The lines are connected to the platform and go in a straight line to the bottom. This is only possible with light lines; therefore, modern polyester lines are needed to achieve this. These lines are known to have a large axial resistance and good fatigue properties. The line forms a 30 to 35-degree angle with the seabed where it meets the anchor (suction piles or vertically loaded anchors to counteract the force vertical component).

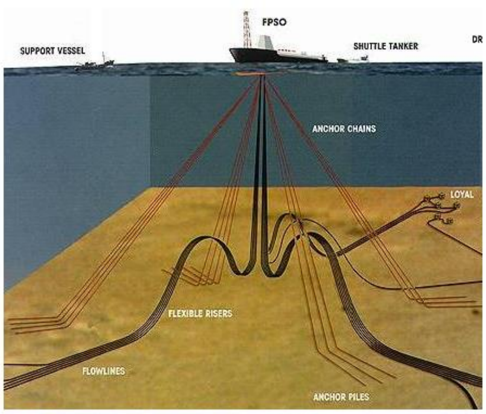

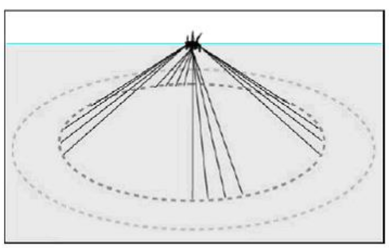

Fig. 1.11 Representation and scheme of taut leg mooring system.

In the taut leg system, the restoring forces are created through axial elastic stretching of the mooring line rather than geometry changes. The restoring forces are determined by the stiffness and elasticity of the mooring line. The taut line has a much more linear stiffness than the catenaries system, what gives the advantage that the offsets under mean load can be controlled better and the total mooring line tensions are smaller. A further advantage of the taut-leg system is the better load sharing between adjacent mooring lines. A representation of the taut-leg system can be observed in figure 1.11.

There is a semi-taut mooring system based on the combination of taut lines and catenaries lines and is used in deep water.

A design of marine wind power platform with taut leg mooring was developed by a consortium of the Massachusetts Institute of Technology and the gas and electricity Italian company ENEL, Sclavoulus et al. (2010).

1.4.3. Tension leg system

The tension leg mooring system consists of a group of parallel tethers attached to a floating body and to the sea bottom in their two extremes. The buoyancy of the floating structure is larger than the total structure displacement and the difference between the two is the buoyancy reservoir which produces the tension in the tethers. At the same time, the floating structure must have a shape that reduces as much as possible its drag when facing tides and it is required to be wide enough as to have the maximum possible righting moment. A representation of the taut-leg system can be observed in figure 1.9.

The platform moored by means of tension legs remains quite restricted to vertical movement, heave, and to pitch and to roll, but allows the horizontal movement, surge, due to wind and waves. Also, the anchors on the sea bottom are exposed to strong vertical forces. For this reason, very often suction anchors are used to withstand these strong vertical forces.

In marine wind generator platforms usually is used the system of three tension legs, Bachinski and Moan (2012).

In the marine wind generator platforms with tension legs the main drawback is the stability against "overturning". Usually, tethers are clamped to the bottom of the floating structure. The floating structure gravity center is above the buoyancy center or the distance between both is quite short and, although this also produces a long balance period and, therefore, small accelerations, it supposes a critic problem for the wind generator as its weight and horizontal force act in a point above the buoyancy center. For this reason, the platform is not stable enough when facing overturning moment, webpage of University of Strathclyde (2020).

1.5 VIV on tension leg mooring systems.

VIV can appear in the three types of mooring systems showed in the former chapter, Huang (2013). But, in the present document the focus will be pointed out on the tension leg platform, due to be regarded as the optimal solution as having the lowest footprint on the seabed; just the area of the platform itself, and require less mooring material, as the mooring length is just the sea depth. To this shorter mooring system, a pontoon with low buoyancy is added, where the tension-legs are connected on its bottom and the windmill place on its top. Hence, the designers can define models where, correctly balancing the pontoon arms and main body sizes, the draft is reduced, the platform stability is not affected, and buoyancy is enough. Therefore, the tension-leg system allows the platform to be smaller than in other design types. Also, all its elements can be built onshore and transported to installation position floating, without needed to be lift to a carrier-ship.

Fig. 1.12 Schemes of TLPWT showing the variation on design variables: sea-surface mast diameter, pontoon size and number of tension legs, Bachynski and Moan, (2012).

Figure 1.12 shows the different design variables of a Tension Leg Platform Wind Turbines: the mast diameter at the sea-surface: a larger diameter increases the platform displacement and buoyancy but also the waves load; the pontoon size, a larger pontoon increases the platform displacement but also the tides and currents load. Finally, the number of tension legs is related to possible safety margin in case of one of them gets damaged.

A tension leg platform design is aimed for intermediate deep waters –the logical step from the already developed installations for shallow waters: sea wind turbines clamped to the seabed, and the large depths-, and must fulfill the following requirements:

- The floating structure (pontoon) must be located at a depth where the local waves amplitude is small enough even for big waves. This depth ranges from 15 meter to 45 meters for a sea depth of 150 m, Bachynski and Moan (2012). This is possible as the wave amplitude decreasing with depth is fast, becoming negligible at a depth of half the wavelength.
- Must leave above the sea surface only the wind generator mast, being this one of the minimal possible diameters that fulfills the structural requirements. Some designs, listed

in next section 1.6, propose to replace the mast by a crossed bar structures as jackets, as with these structures the requirements for wave load resistance can be minimized. Furthermore, decreasing mast diameter minimizes the tension leg variation of tension due to the sea depth variation produced by the tidal.

Regarding these two considerations, it is possible to suppose that the forces due to tides on long tension legs for deep seas might result in stronger forces that those of the waves upon the mast or jacket limited length.

On the other hand, the calculus of the structure against breaking is well posed, once the loads to which the structure will be facing are known. But the VIV calculus has more uncertainty as the value of the cyclic load, its frequency, and the number of cycles that the structure can bear, what will define the structure lifespan, are more difficult to be determined.

Consequently, VIV appears as the phenomenon with greatest interest for platform design.

1.6 Design of a tension-leg platform and VIV fatigue.

The Tension Leg Platform Wind Turbine concept is promising for intermediate water depths because the limited platform motions are expected to reduce the structural loading on the tower and blades compared to other floating concepts, without requiring the large draft of a spar or spread mooring-system of a semi-submergible. Several tension-leg platforms for wind turbines have been designed, as:

- Concept Marine Associated (CMA): it has “jacket” type column at sea surface to reduce wave loads and is moored by ropes, Fulton et al. (2007)
- MIT/Enel (Italy): taut-leg mooring, Sclavoulus et al. (2010).
- MIT/National Renewable Energy Laboratory (NREL), Matha et al. (2010)
- University of Maine, Robertson and Jonkman (2011), Stewart et al. (2012)
- Gloster Associates, Moon III, W.L. and Nordstrom, C.J. (2010).
- GL Garrad Hassan, Henderson, A.R. et al. (2010)
- Nihei (Japan), Nihei, Y. et al. (2011)

- IDEAS: jacket type column and taut legs. Copple and Capanoglu (2012)

All the designs, but the CMA design, have steel pipe made tendons ranging from 3 to 8.

The platform displacements range from 846 tons (Nihei) to 12 187 (MIT - Enel).

The TLEG platform column diameter, at sea-surface, ranges from 4.5 to 18 meter.

Pontoon volume is negligible for the MIT - Enel and MIT/NREL designs.

But being the TLEG platforms focused on intermediate depths (100 – 250 m), loads due to currents grow significantly compared to those of shallow waters. Also, being tensioned, they do not have the degree-of-freedom of the catenaries, that can freely oscillate increasing their length laying on the seabed to adapt themselves to the currents without a large increase of their tension.

These circumstances, together with the fact that the sea currents are perpendicular to leg axis, makes that the vibration phenomenon known as Vortex-Induced Vibrations, VIV, supposes a higher risk for tension-leg and taut-leg types of mooring system than for the catenaries system, Huang, (2013). Hence, analyzing VIV in tension-leg platforms is required.

1.7 What is hence V.I.V?

Any structure of a given volume, immersed in a flowing fluid, might experience VIV. With the aim of explaining what the VIV are, the classic problem: that of an oscillating circular cylinder, will be considered. This was also the first observed case and given explanation, as high industrial chimneys fell in a direction perpendicular to the wind, Strouhal (1878), Rayleight (1879). Afterward, no further investigation was carried out until problem arises on drilling risers of oil and gas platforms and large onshore structures as bridges and stadiums during the ‘40s and manily ´50s and ´60s of the XX century: Scrutton (1955, 1956, 1965), Vichery and Watkins (1962), Bishop and Hassan (1964) and Feng (1968).This problem is also the one that corresponds with the case of the tension legs platform, Meneguini et al. (2004) Vandiver et al. (2006) Holmes et al. (2006) and Lie et al. (2008).

Fig. 1.13. Von Karman Vortex Street. Blevins (1984).

Upon a fixed non-moving nor vibrating cylinder appears an oscillating force induced by vortex shedding in the following way. The cylinder is located perpendicular to the flow, see figure 1.13. Blevins (1984). Hence, flow meets at every point of the cylinder axis a circular section. This circular section has a diameter perpendicular to the flow direction. In the two extremes of such diameter vortex appear alternatively when flow Reynolds number reaches the value 5. The shedding occurs in a way that, when on one of the extremes the pressure reaches a maximum and, consequently the velocity a minimum, the opposite occurs in the other extreme. This asymmetric and periodic flow is known as Von Karman Vortex Street.

The pressure difference upon the cylinder section creates a net force. As the vortex shedding points are not exactly the ones perpendicular to the cylinder section, as a small variation up- or downflow appears, both force components arise: one in the flow direction and the other in the perpendicular one, being this last one more significant. If the Reynolds number varies, also the vortex pattern does, producing at different Reynolds number ranges a different vortex shedding regime as figure 1.14 shows.

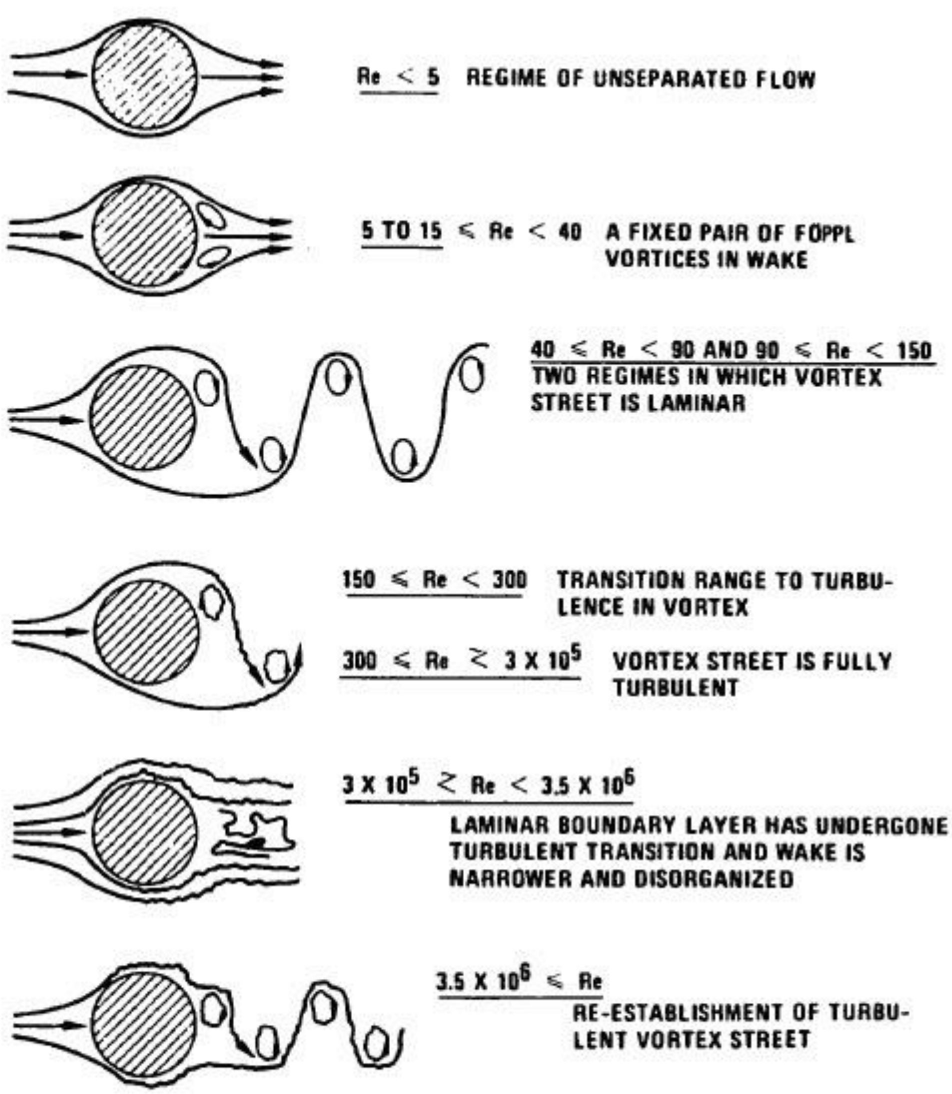

Fig. 1.14. Fixed cylinder vortex shedding regimes, Blevins (1984).

The vortex shedding regimes of a fixed and rigid circular cylinder vary with the Reynolds number, that is, with flow velocity and cylinder diameter for a given fluid. For low velocity values (Reynolds numbers Re < 5) the flow around the cylinder remains without shedding. When the Reynolds number varies from 5 to 40, a couple of fixed vortices appear. For a Reynolds number value between 40 and 90, the vortex street is laminar, this is, the fluid streamlines follow oscillating trajectories but without being broken into eddies. The transition range, in which vortices change from a laminar flow to a turbulent one, has been observed in the Reynolds number range of 150 to 300. From a Reynolds number range from 300 to 3E+5, the vortex street is fully turbulent. In the Reynolds number range from 3E+5 to 3E+6, the laminar boundary layer becomes turbulent, and the wake is narrow and disordered. When the Reynolds number exceeds the value of 3E+6, a street of turbulent vortices is again established. These vortex shedding regimes can be observed in figure 1.14, Blevins (1984).

The vortex shedding frequency is, therefore, related with the flow velocity. This relationship is given by the Strouhal number which is defined as:

$$St = \frac{fD}{V} \tag{1.1}$$

Where:

f is the vortex shedding frequency for a quiescent body (also called Strouhal frequency).

D is the cylinder diameter and

V is the flow bulk velocity.

Besides of the former parameters, the Strouhal number also depends on the cylinder surface roughness and the bulk flow turbulence intensity.

But, if the body is not rigid but flexible, or is rigid but not fixedly installed, the response to such oscillating forces is vibrations of the cylinder in both the inflow and flow transversal directions and the vortex shedding regimes of figure 1.14 are no longer valid.

If the cylinder is rigid but not fixedly installed, that is a rigid cylinder that cannot deform but with its extremes connected to a fixed wall by means of springs (oscillation displacement proportional to force) and dampers (oscillation velocity proportional to force), the vortex shedding regimes in this case are shown in figure 1.15, Williamson and Roshko (1988). This type of vibration is known as Vortex-Induced Vibrations, VIV, and its vortex shedding regimes vary with both the flow velocity and the movement amplitude. Both the flow velocity, U, and oscillation amplitude, A, are given in dimensionless form in figure 1.15.

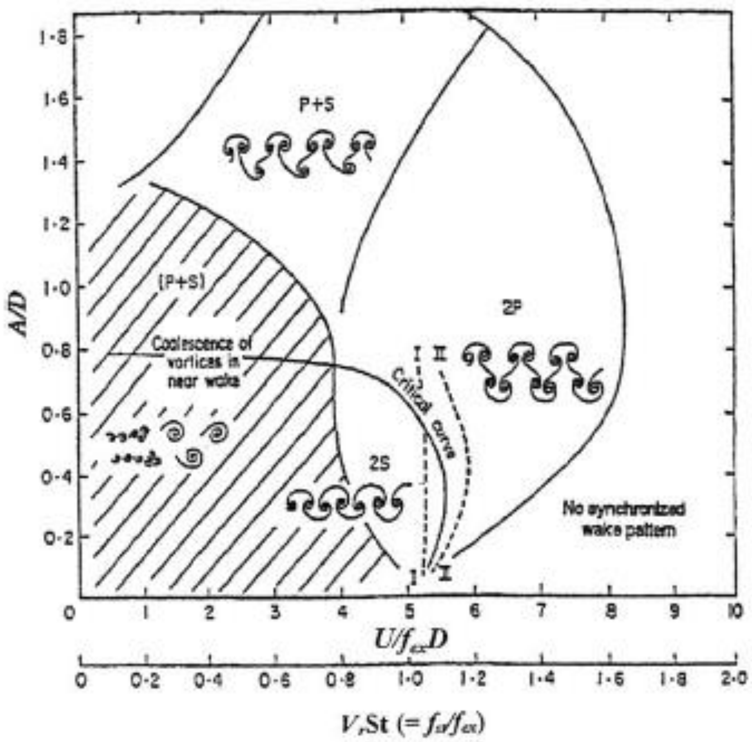

Fig. 1.15 Vortex type map, Williamson and Roshko (1988)

For an elastically mounted rigid cylinder experiencing small enough oscillation amplitudes, as the zone of small y-axis values of figure 1.15 shows, vortices remain shedding in a similar pattern than fixed cylinders (y = 0, corresponding to *A/D* = 0 in figure 1.15). In this case, vortex shedding frequency is the same that the Strouhal frequency and the structure oscillation frequency is also the Strouhal frequency.

However, as flow velocity increases in a way that the vortex shedding frequency gets closer to the rigid cylinder structure natural frequency, which is a single-value frequency defined by cylinder mass and its fixing system: stiffness of the springs and damping coefficient of the dampers, the vortex shedding frequency becomes suddenly “adjusted” to the structure natural frequency. This phenomenon is a VIV critical condition named synchronization or “lock-in”, and supposes a structure high risk condition, as the response is amplified. Solutions for this phenomenon are two: the incorporation of strakes along the cylinder: a helicoidally welded plate, Holmes et al. (2006), Vandiver et al. (2006), and to design the risers in a way that their structure natural frequency is much different of that of the expected Strouhal number. Strakes are an expensive solution used currently as the structure and hydrodynamic frequency separation is not yet available.

However, despite the interest of the figure 1.15, this one indicates that, for certain flow velocity upon a cylinder of some diameter and natural frequency, the oscillation amplitude might vary in a wide range, even maintaining the same vortex shedding patron. This can be observed, for example, in the case of a dimensionless velocity value of value 6, the dimensionless amplitude might vary from 0.2 to 1.8. Logically, it will exist more factors that determine at which dimensionless amplitude the dynamic balance is reached. These factors are:

- Geometric parameters.
    - Cylinder diameter
    - Cylinder length
    - Cylinder surface roughness.
- Fluid-dynamic parameters:
    - Fluid density
    - Fluid viscosity
    - Bulk flow velocity
- Structural parameters:
    - Body mass (without added mass)
    - Body structural damping
    - Body stiffness

The structural parameters show some peculiarities. For example, to calculate the effect of the mass a factor named mass ratio should be used instead of the body mass. The mass ratio is defined as the structure mass divided by its displacement. This, for an immersed body is clearly the ratio between the body and the fluid densities.

In the same way, the effect of damping is given by the damping ratio. Unluckily, there are no models to calculate the structural damping factors.

Finally, there is the case of flexible cylinder, that is the case that really takes places in nature. In this case each cylinder spanwise section has, in any instant, its own displacement, velocity and acceleration. Also, any cylinder section is displacing and turning with refer to an adjacent one as function of its own mechanical characteristics, that form the elasticity matrix of the elastic body. Hence, body has no more a single natural oscillation frequency, but a frequency spectrum. The flow will excite one these frequency spectrum values, the one closest to the vortex shedding frequency and, in some cases, these flow and body frequencies will shift to became equal, taking place in such case the synchronization in a flexible body.

1.8 Synchronization.

Synchronization is regarded as the structure most dangerous VIV condition and was firstly analyzed by Cincotta et al. (1966). His studies, as all those from ´60s to the end of XX century, paid attention to an elastically mounted rigid cylinder: Vickery and Watkins (1962), Bishop and Hassan (1963), Feng (1968), Hartlen and Currie (1970), Umemura et al. (1971), Skop and Griffin (1973), Blevins (1974), Sarpkaya (1979), Bearman (1984) and Khalak and Williamson (1999). According to this last research work, synchronization is a self-sustained oscillation that occurs for flow velocity values that made the vortex shedding frequency equal to the elastically mounted structure natural frequency.

Other definitions of VIV have been given, all based on the elastically mounted rigid cylinder. Leonard and Roshko (2001) defined the synchronization as the situation with zero damping and sinusoidal movement and takes place when the “effective” elasticity is zero, where the effective elasticity represents the net effect (the difference between mass and stiffness).

Another definition, proposed by Dahl (2008), is that of the situation of flow instability at Strouhal frequency where structure oscillates and the vortex shedding frequency gets coupled with the structure oscillation frequency. As the body oscillation amplitude increases, also the frequency band width increases. This property is named wake capture. The wake capability of capturing the structure oscillation frequency produces a significant change in the added mass effects which, in turn, can change the natural oscillation frequency to an “effective” one. This natural “effective” frequency depends on the flow velocity. Hence, synchronization is a dynamic equilibrium defined by the flow and structure frequency coupling and energy balance.

Hence, in the synchronization regime, when a structure vibrates at its natural frequency and get close to constant and sustained oscillation amplitude, the structural vibration movement rules the vortex shedding frequency. From this it can be deduced that:

- The linear relationship (according to the Strouhal number definition) between the velocity and vortex shedding frequency is not correct in the synchronization regime.
- The structure keeps a vibration frequency until the moment that a significant force at a different frequency distorts it.
- As the structures are lighter and with lower stiffness the synchronization band is wider. This can be the case of tension-legs if there are of hollowed cylinder type. This type of tension-leg is sometimes used to produce buoyancy already with the legs and reduce the required pontoon size.

Known these items, the question of what determines the amplitude value for certain reduced velocity remains. According to what has been observed experimentally, the vibration amplitude has a main parameter depending on what is the ratio between the excitation frequency and the structure natural frequency, Williamson and Govardhan (2004):

- If the ratio is <1, the main parameter is the stiffness.
- If the ratio is >1, the main parameter is the mass.
- If the ratio is approximately 1 (resonance), the main parameter is the damping.

Besides, experimental results also showed that there are several modes of vortex shedding in the synchronization regime:

- When the mass/damping ratio is high, two modes appear, known as initial range and lower range.
- When the ratio mass/damping is low, a third one appears, named upper range.

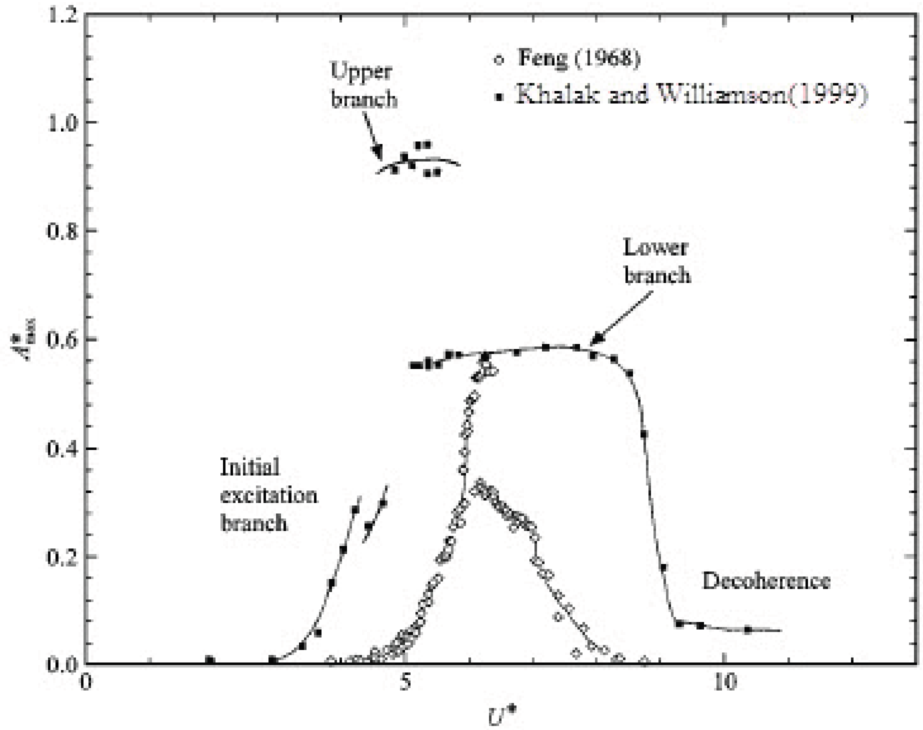

Fig. 1.16. Comparison of data obtained in air, Feng (1968) and water, Khalak and Williamson (1999). (Khalak and Williamson, 1999).

Figure 1.16 shows the two curves associated to the experiments of a rigid cylinder elastically mounted in air, Feng (1968). It can be observed how synchronization starts at a reduced velocity value of 5 that corresponds to an excitation frequency value equal to the natural frequency. From this value above the amplitude grows until reaching a maximum at a reduced velocity value of 6 and, above this value, it decreases suddenly. These discontinuities in the vibration mode produced by the vortex shedding are also a characteristic of the phenomenon, characteristic that has prevented a mathematical formulation that contains the different vibration modes.

In the case of the results in water, figure 1.16, three branches are observed, Khalak and Williamson (1999). In fact, the third branch (denoted in the graphic as Upper branch) appears as a stretch of larger amplitude between the two lower stretches in a way that, if it would have the same amplitude that the third branch, the curve would be approximately continuous as in the case in air. It must be also observed that there are points of different amplitudes for the same reduced velocity value.

This third branch, being the one with larger amplitude and the same frequency, is the one of larger energy and displacement and the most dangerous for the cylinder fixing system integrity.

Hence, in the synchronization condition the oscillation frequency is that of the structure and the vortex shedding frequency changes to become equal to the structure one. A possible explanation of such frequency adjustment is that the vortex induced forces can produce a change in the effective added mass which, in turn, makes the effective natural frequency closer to the wake frequency. At the end, the vortex shedding frequency gets totally adjusted to the structure natural frequency producing the synchronization.

Other important experimental observations have been the following ones:

- The synchronization band width decreases as the Reynolds number increases.
- The mass ratio has no influence in the response peak amplitude (as in this range the main parameter is the damping).
- The response peak amplitude increases as Reynolds number increases.
- The other factor affecting the amplitude is a factor related with the damping but not the damping itself.

But, as above commented, all these results have been obtained for the case of an elastically mounted rigid cylinder which natural frequency is a single value determined by the cylinder mass (with the added mass in the case of being immersed in water, as in air this value is negligible) and the value of the stiffness of the springs that connect it to the fixed points. Differently, the case of interest is that of a flexible cylinder. The flexible cylinder has a spectrum of natural frequencies, one for each vibration mode and synchronization can occur for any of these frequencies. The knowledge about VIV in flexible cylinders is much less developed than for the case of the elastically mounted rigid cylinder. The difficulty of the phenomenon, where body stress and strain play an important role and are linked to the fluid flow, together with the required size of the bodies to experience realistic VIV behavior, have limited the works devoted to it. On the other hand, the importance of the phenomenon, as more and more offshore installations are built, confirms the importance of study it further.

1.9 Final considerations.

The need of using clean energy sources has yield to the development of systems that produce such types of energies. Possible, the most developed one would be the wind energy, as indicates the fact that, for wind-power installation pioneer countries, the in-land installation has reached the possible maximum as wind-generators have been already installed in all the possible suitable zones.

The logical next step (due to room and wind sources) has been the offshore installation. The development of the first development niche, the one for shallow waters, with the wind-generator mast clamped at the sea bottom is at full development currently. However, the sea zones that fulfill the shallow water requirement are few, what is forcing the development of deep-water technologies, technologies that, due to the different working conditions (not fixed elements in the sea), force to develop elements that withstand such conditions: platforms where wind-generators are installed.

Among the different platform types, the ones named Tension Leg Platforms seem to be a good solution as there are not excessively stable (hence, avoiding the appearance of high accelerations at the generator nacelle, as it occurs with the spar platform type) neither being so high costs as the semi-submergible ones.

With the increasing platform installation depth, the sea tides (which act upon most or even the whole sea depth) become more important than the waves (which act only near the sea surface). This aspect does not indicate that waves should not be considered in the platform design, but there are known solutions to reduce its effect as, in example, jacket type masts.

The importance of tides is that they produce a phenomenon that can even destroy the platform. This is a phenomenon that produces forces that, being of smaller magnitude than those that the platform can withstand, repeated in a cyclic manner at certain frequencies, can lead to the installation destruction by losing their mooring system: tension legs or risers. This phenomenon is the VIV.

Furthermore, VIV calculations are far more complex than those of static loads (structure and equipment weight loads) which calculation procedures are already developed with accuracy (general structural analysis).

Despite the great effort carried out in the analysis of such phenomenon in the last years, its great difficulty makes that still exist many uncertainties about riser behavior and accurate calculus for engineering purposes. For example, and it is a clear main task for the research community, is necessary to analyze this phenomenon with its parameters in the ranges that the risers experience in the real installations. Also, there is a need to find the riser behavior when changing one of its parameters, besides the Reynolds number, which is the only one commonly investigated. This is a basic step to develop the required knowledge to design installations with lower safety margins and, therefore, economic viability. In this work, these parameters are closer to the real installation´s ones but those have not been reached as there is no experimental results to compared with.

Based on these facts, this work has surveyed the current situation in the VIV field for offshore wind power in this first chapter and assessed some objectives to investigate about it. These objectives are listed in the following subchapter 1.10.

To carry out the work to achieve these objectives a methodology has been required. This methodology is indicated in the subchapter 1.11.

1.10 Objetives of the study

Regarding the review of the subject carried out in this chapter, the objectives of the present Ph.D. thesis are:

1. To analyze VIV at higher Reynolds number than those found in the bibliography, and closer to real facilities values, and compare them to results at lower Reynolds numbers.

2. To analyze the influence of the Reynolds number in the riser vibration response.

3. To clarify the effect of the flow in the change of structure frequency spectrum.

4. To find the lift and drag coefficients as function of the Reynolds number and to compare them with those found by other authors.

5. To analyze synchronization at higher Reynolds numbers and to check the different riser vibration characteristics that defines a vibration situation as synchronization.

6. To propose a method to calculate the structure frequency spectra incorporating the effect of the flow.

7. To propose a method to calculate the riser vibration amplitude.

1.11 Methodology of the study

To achieve the objectives numbered in the previous section, the following tasks have been carried out and are reported in the next chapters as follows:

1. A review of the numerical modeling of the flow around a riser and of the riser oscillating behavior as well as a brief mathematical formulation that poses the hydrodynamic and structural problem and the governing equations are given in chapter **2**.

2. The riser response as function of the hydrodynamic parameter: the Reynolds number, is analyzed in chapter **3**.

3. The interaction between the flow and the vibration response and the physical phenomenon that connects them is analyzed in chapter **4**.

4. Lift and drag force coefficients are found and compare to those of other authors in chapter **5**.

5. The synchronization phenomenon is analyzed by means of its different characteristics in chapter **6**.

6. Chapter **7** shows VIV results when changing the main structural parameter: Young´s modulus.

7. Chapter **8** summarizes the thesis main outcomes and suggests future work.

Chapter 2

2. Physical and numerical modeling.

2.1. Introduction

In the present chapter, the physics, and the mathematical formulation of the posed problem of VIV in a riser is described. The riser is an elastic body that deforms and oscillates as a response to the excitation produced by the fluid flow. A different flow velocity excites the riser producing both different vibration mode and amplitude. A vibration mode is characterized by its frequency and shape and it is numbered according to the number of half waves in the vibration. The analyzed fluid flow is a constant and uniform speed fluid flow. This type of flow produces larger oscillation amplitudes, Resvanis et al. (2012) and, therefore, a higher deformation, tension, and risk for the riser.

The scope of this thesis is to analyze this phenomenon in a riser of closer characteristics to those of real facilities ones, mainly in two aspects: riser size and flow Reynolds number, as there are already several both experimental and computational studies of risers at much lower Reynolds numbers, as it will be shown in section 2.2.

Higher Reynolds number presents several effects: firstly, when velocity is higher, drag force will be higher too, as drag force varies with the second power of the velocity. As drag force upon the riser increases, also reactions on riser fixing points and tension within the riser will do, as they will balance the drag force resultant on the riser. Secondly, if the riser tension increases the structure frequency spectrum will vary, as the tension component of the structure frequency varies with the squared root power of the tension. Hence, the higher is the tension, the higher is the structure frequency. This effect will be compared between the cases of low and high Reynolds number.

Therefore, riser analysis requires the study of the interaction of the flow with the structure which leads to the need of coupling the physics of the flow, this is, the study of the fluid dynamic behavior, and the physics of the structure, the structural behavior. Studies and engineering projects in each of these physics' fields, the fluid dynamics and the structures or finite element analysis, have been developed already since many years ago, but the two fields coupled is a quite recent development and of great interests as many facilities might show phenomena where these two aspects are linked.

The riser analysis shows also a technical difficulty represented by the need of studying high length to diameter ratio (L/D) risers together with their performance at real installations Reynolds numbers, that is, reaching Reynolds number as high as 10e+6. Currently, there is no scaling theory that could allow analyzing riser in towing tank installations and only exceptionally large facilities have reached a riser length of 38 m and Reynolds number of 126K, riser that has been taken as model for the simulations. Unluckily, the data required to simulate such riser by computational methods are not available and analysis of risers at lower Reynolds numbers have been already carried out, Bourghet et al. (2011, 2013 and 2015), Lothode et al. (2015) and Xiao and Wang (2016).

The code used to carry out the simulations is the ANSYS-multi-Physics. This code allows communicating ANSYS solvers of different physics with transference of different variable fields between them.

For the fluid dynamics phenomenon two different solvers: Fluent and CFX, are available within ANSYS Multiphysics, both are based on a finite volume method (FVM), ANSYS Theory Guide (2016), to discretize the Navier-Stokes or fluid governing equations. Nevertheless, there is an important difference between these two solvers: CFX is a coupled solver meanwhile Fluent is uncoupled or segregated.

Uncoupled solvers like Fluent solve the three momentum equations (velocity) sequentially. Afterwards, using this updated velocity field, they calculate the pressure correction equation for continuity. This is repeated until convergence. This pressure correction is done by using some pressure-velocity coupling scheme, as SIMPLE or SIMPLEC, both available for Fluent.

CFX does not use SIMPLE neither other coupling algorithms as it is a fully coupled solver. Coupled solvers have all three momentum equations and pressure equation in the same matrix, so they are solved together. It does not need pressure-velocity coupling as that is taken care in the matrix solution. What it does require is an interpolation of the pressure from the cell nodes to cell centers to avoid decoupling of adjacent cells. For CFX this is the Rhie-Chow interpolation scheme.

Coupled solvers are more robust, this is, do not require a high-quality mesh in terms of cell skewness and determinant (both indicators of the mesh cells orthogonality, that is, the closeness of cell angles to 90 degrees), but take more time per iteration and use more memory as the matrix is bigger. Nevertheless, coupled solvers usually converge much faster as must converge only the non-linear terms. Segregated solvers need to converge both the non-linear terms and the pressure-velocity coupling.

The higher robustness of CFX and its capability of use larger time-steps, that will be defined by physics requirements and not due to mathematical convergence necessities, have been the reasons to choose it as solver.

2.2. Review of computational modeling of VIV

Several computational research works have been published in the field of VIV. The complexity of such works has increased as knowledge of the phenomenon developed as well as the computational tools capabilities (software) and computer power (hardware) also improved. For these reasons, the VIV computational research has followed a several stages path. This path can be observed in Table 2.1, that shows the first works carried out in VIV analysis.

The first stage focused on 2D simulations and started with the first study of VIV in a cylinder by Peter Justesen in 1991. He analyzed the oscillation of the flow around a fixed and rigid circular cylinder at low Keulegan-Carpenter and Reynolds numbers by using a Finite Element Method (FEM) model, therefore, only the flow field had to be computed. The Keulegan-Carpenter number is a non-dimensional number that describes the relative importance of drag forces over inertial forces in periodic motions as waves. It is defined as the product of the flow velocity amplitude and the oscillation period divided by the characteristic length. He analyzed the vortex shedding structures.

Table 2.1 First computational simulations of VIV in cylinders (Sources: Williamson and Gavardhan, 2004 and thesis author´s own investigation [1]).

Investigators	**Year**	**Medium**	**Re**	**m*ζ**	**A* (peak)**
Finite Element Method (FEM)					
Justesen (1)	1991	2D-code	200	0.00	
Direct Numerical simulation (DNS)					
Blackburn and Karniadakis	1993	2D-code	200	0.012	0.64
Newman and Karniadakis	1996	2D-code	200	0.00	0.65
Shiels, Leonard and Roshko	2001	2D-code	100	0.00	0.59
Fujarra et al.	1998	2D-code	200	0.015	0.61
Guilmineau and Queutey	2000	2D-code	100	0.179	0.54
Blackburn et al.	2001	2D-code	560	0.122	0.47
Evangelinos and Karniadakis	1999	3D-code	1000	0.00	0.47
Turbulence Models (LES and RANS)					
Saltara et al. (LES)	1998	2D-code	1000	0.013	0.67
Guilmineau and Queutey	2002	2D-code	3800	0.013	0.98

This was the VIV analyzing first computational approach. Several works followed it, Table 2.1, with different numerical models. The last work following this 2D and Keulegan-Carperter dependence methodology was that of Zhao et al. (2012). Blackburn and Karniadakis (1993) confirmed such difficulty in simulating the solid movement and oscillation with the software and hardware capabilities of the time and showed the need of using some simplifications: "Rather than arrange a method in which the computational grid deformed to allow cylinder motion, we have used a fixed-configuration grid attached to the cylinder. By applying appropriate boundary conditions and adding a fictitious forcing term to the Navier-Stokes's equations, the flow simulation may be carried out". They analyzed firstly a rigid cylinder forced to oscillate in the crossflow direction at several frequencies and flow of Reynolds number 200 obtaining the drag and lift coefficients as well as the force-oscillation phase angle as function of the oscillating frequency. Later, they released the cylinder allowing it to free oscillate forcing the cylinder natural frequency to match the forced cylinder vortex shedding frequency. They obtained the maximum crossflow amplitudes as function of the mass-damping product.

It was not until 1995, where Henderson and Karniadakis developed a parallel/spectral Fourier method. This tool allowed the simulation of the vibration deformation for first time, but with some important restrictions. These restrictions were the capability of simulating only infinite long cylinders, being this infinite length a method to introduce 3D turbulence but not the 3D cylinder deformation or, when the 3D cylinder deformation was included, this was prescribed by means of a sinusoidal equation that forced the cylinder shape along time.

Using this Direct Numerical Simulation (DNS) tool, NekTar, the first 3D simulations were those of Newman and Karniadakis (1996 and 1997). In the first article they analyzed a "short" cable of L/D= 12.6 and a "long" cable of L/D = 45, both for Reynolds numbers 100, 200 and 300. They paid attention to the cable dynamics as well as the lift forces and the power produced by the lift force. In their second article they returned to Blackburn's riser infinite length by means of an extended 2D case analyzing a case with Reynolds 100 and 200. In their second article they found both a standing wave and a travelling wave response but, in general, the travelling wave is the most common response. A standing wave cable response produces an interwoven pattern of vorticity, while a travelling wave cable response produces oblique vortex shedding. The lift force on the cable and its motion amplitudes are larger for the standing wave response. When the Reynolds number reaches a value of 200, the cable and wake response are no longer periodic, and the maximum amplitude of the cable oscillation is about one-cylinder diameter, in agreement with experimental results.

The aim of all these works were to reproduce the experimental results represented by the Griffin Plot (1980), a plot developed during the ´70s by Skop and Griffin (1973) representing the oscillation amplitude as function of the Scrutton number, or a parameter derived from it, concretely the product of mass and damping $m\zeta$. The Scruton number, Scruton (1965), is:

$$S_c = \frac{2\delta_s m_e}{\rho b_{ref}^2} \tag{2.1}$$

Where:

δ_s is the structural damping expressed by the logarithmic damping decrement.

m_e is the effective mass per unit length.

ρ is the fluid density.

b_{ref} is the characteristic length of the structure (for a riser, its diameter).

This spectral method approximates the solution via global functions, usually Fourier series, and is intensively used for the study of isotropic and homogenous turbulence. It is not attractive for problems characterized by complex geometries. The spectral/hp element method combines the geometric flexibility of classical finite element techniques with the high-order convergence features of spectral method. This technique utilizes a polynomial expansion of high order to approximate the solution on a collection of elements. It can be considered as an extension of the more widespread Finite Element Method, which approximates the solution by linear functions on elements, but using exponential convergence properties. Spectral method uses a series of high-order polynomials on each element. This allows reducing the error (residual) either refining the mesh or increasing the order of the polynomial. The simulations carried out with this method are Direct Numerical Simulations (DNS) as polynomial approach allows resolving all the turbulence scales with no turbulence model. **The main limitation of the DNS approach is the maximum Reynolds number that can simulate, being this value just a bit above 10000.**

Anagnostopoulus (1998) analyzed an elastically supported rigid cylinder with motion restricted to the in-line direction incorporating an oscillating flow stream of constant velocity value to yield a Reynolds number of 200 and varying the oscillating flow period to achieve Keulegan-Carpenter (KC) numbers in the range 2 to 20. They used a Finite Element Method where the variables were the stream function and the vorticity. For each KC number, they analyzed several frequency ratios defining this frequency ratio as the ratio between the stream oscillation frequency and the cylinder natural frequency in air. They obtained the stories of the cylinder response and hydrodynamic forces. Drag and added mass coefficients in the total in-line force were evaluated.

Evangelinos and Karniakakis (1999) did a visual analysis of shedding patterns with the new version of their DNS code NekTar. If in former works, they used a simple string equation to model the motion of the structure, Newman and Karniadakis (1996), or this simple equation with an added term for the beam blending stiffness, Evangelinos and Karniadakis (1997), in this work the NekTar new version allowed to increase the former Reynolds number limitation from 300 to 1000.

Also, in 2001, Shiels, Leonard and Roshko studied an elastically mounted rigid cylinder at Reynolds number 100. They observed the appearance of VIV in a cylinder with zero mass, zero spring and zero damping. They limited the cylinder movement to the crossflow movement. The wake resulted to be a Von Karman vortex street where, at any moment, the transversal ideal added mass force is exactly balance by the vortex force. To do so, they used other computational method, the “High-Resolution Viscous Vortex Method”. This is a mesh-free method for direct numerically solving 2D Navier-Stokes in Lagrange coordinates. It does not implement any turbulence and is free of arbitrary parameters. The main idea of this method is to present vorticity field with discrete regions (domains) which travel with diffusive velocity relative to fluid and conserve their circulation. The fluid is viscous and incompressible with viscosity and density constants. It is also a Direct Numerical Simulation (DNS) method and convenient for deforming boundaries due to the mesh-free characteristic.

In the year 2002 Guilmineau and Queutey developed the first 2D study using a Reynolds Averaged-Navier Stokes (RANS) method.

Dong et al. (2004) developed a DNS simulation for Reynolds number 10K, the highest Reynolds analyzed with a DNS method. Meanwhile, Guilmineau (2004) used a 2D RANS method with Menter´s SST (Shear Stress Transport) turbulence model to analyze a case of a elastically mounted rigid cylinder for Reynolds between 900 and 15K. Their simulations correctly predicted the maximum oscillation amplitudes, but they did not match the upper branch found experimentally.

Yamamoto (2004) and Meneghini et al. (2004), in different works, used a Discrete Vortex Method (DVM), firstly introduced by Saltara et al. (1998). The DVM method is a Lagrangian numerical scheme technique, a potential scheme for simulating two-dimensional, incompressible, and viscous fluid flow. The method employs the stream-based boundary integral method and incorporates the growing core size and core spread method to model the diffusion of vorticity. The riser is discretized in N panels and N discrete vortices, with circulation Γ_i, are created from a certain distance of the body, one for each panel. The vortices are convected and their velocities are assessed through the sum of the free stream velocity and the induced velocities from the other vortices. The induced velocities are calculated through the Biot-Savart law. Forces on the riser are calculated integrating the pressures and viscous stresses. Viscous stresses are evaluated from the velocities in the near-wall region, and the pressure distribution is calculated relating the vorticity flux on the wall to the generation of circulation.

Meneguini´s team (2004) used this technique to analyze the cases of a elastically mounted rigid cylinder, a cantilever flexible cylinder and two risers. The cantilever cylinder was analyzed for Reynolds number ranging from 7K to 2.3e+5 and lengths ranging from 100 to 4600 meter using

128 panels. The first riser was analyzed for uniform flow of Reynolds number 58K to 200K for a 120m riser using 100 panels. The second riser was 1500-meter-long and was discretized with 600 panels. They compare the results with those obtained with the quasi-steady theory, as no experimental results were available. They obtained the drag and lift force coefficients for the elastically mounted cylinder. For the risers they found just the vibration envelopes.

All the former studies were carried out with in-house software. The works developed with a DNS method are those of the M.I.T. group and software *Nektar*, based on the spectral/hp method. The works developed with a DVM quasi-3D method was developed by the University of Sao Paulo, the Brazilian oil company Petrobras research center Centro de Pesquisas Leopoldo Américo Miguez de Melo, known as CENPES and the Brazilian oil company Petrobras itself.

In the early years of 2000, some Reynolds Averaged Navier-Stokes (RANS) methods were also developed in-house, Guilmineau and Queutey (2002) and Placzek et al. (2009).

In 2004 Potanza et al. presented a new simulation approach, based on chimera meshes, a set of two meshes, one associated to the riser and the other to the fluid domain being the first one immersed in the second. Hence, the deformation takes place in the first mesh and is transferred to the second one. In following works during 2005 and 2007 they developed a new method to discretize the Navier-Stokes's equations, the Finite-Analytic Navier Stokes (FANS) approach. The FANS approach estimates a local-analytic solution of governing equation in the form of Fourier series and applies it to each numerical element locally. The system of equation thus formed is used to calculate the flow variables for each nodal value. The continuity equation is solved using a finite volume approach and a hybrid PISO/SIMPLER algorithm is used to update the pressure field. The approach requires also chimera meshes.

In the year 2006 Holmes, Constantinides and Oakley in one work, and Menter (2006) in other work, presented the two first studies with commercial software. Holmes used a coupling FEM+CFD method developed for the firm Altair HyperWorks to analyze a 38-meter length, 0.027meter diameter riser. He covered the Reynolds number range 7K to 50K. Constantinides and Oakley continued this work the same year (2006) and two years later (2008). They analyzed a stationary cylinder, a flat surface riser and a riser with strakes with a mixed turbulence model of RANS near riser surface and LES far from it and with DES model. They clarify that, for a stationary cylinder DES turbulence model is better than the RANS but, for oscillating risers, RANS is better, since vortices are in this case more organized and 2D due to cylinder motion. In the analysis of the flat riser, the oscillation mode results agreed quite well for low Reynolds values but overestimated the mode value for their higher Reynolds numbers. At that moment they did not know whether the overestimation arise from an incorrect treatment of the riser structure model or from the fluid-dynamic model. Menter (2006) used a coupling of FVM (Finite Volume Method) plus CFD developed for ANSYS group.

Pan et al. (2007) analyzed a 2D case using an in-house CFD RANS method with SST k-ω turbulence model for an elastically mounted rigid cylinder with Reynolds number range 2.5K to 13K. They focused on determining vibration peak amplitudes, drag and lift forces coefficients and visualizing the vortex shedding. They also explained the impossibility of finding the vibration upper branch with computational methods and the reason for each approach (DNS, LES and RANS) to be unable to find such branch. They claim on that the upper branch appears randomly in the experiments, which will force to carry out extremely long computations. They also commented that three-dimension turbulence characteristic might play an important role and that 2D simulations will not be correct to capture this phenomenon.

Wanderley et al. (2008) analyzed a 2D case using an in-house CFD slightly compressible RANS method with a k-ε turbulence model for Reynolds number ranging from 2K to 12K. They used the drag coefficient of a fixed cylinder as the way of validation for the numerical method and grid, as the validation for lower Reynolds numbers do not assure the validation for higher ones, the y^+ value will surely change. The present work follows their approach for verification purpose in section 2.4.9. They obtained good accuracy on oscillation amplitudes. They reached cylinder crossflow amplitude 0.94 for upper branch, in agreement with Williamson and Khalak (1999) results.

Plazcek et al. (2009) analyzed a 2D case using a commercial CFD RANS code, the Star-CD from Adapco Group (the third commercial software together with those of Altair and ANSYS) for a

Reynolds number 100. They started analyzing the vortex shedding regime for a fixed cylinder. They continued with a forced oscillating rigid cylinder to end with an elastically mounted rigid cylinder. They analyzed the synchronization phenomenon with the forced oscillation case, following the used experimental methodology. In the elastically mounted rigid cylinder, they analyzed drag and lift force coefficients as well as oscillation amplitudes.

Huang et al. (2009) presented a work with a Finite Analytic Navier Stokes (FANS) method. Huang et al. continued this work in a second and third article (2011a and 2011b) in which he analyzed risers as well as different types of mooring systems: taut legs and catenaries' lines.

Bourghet, R. et al. (2011) presented the first of a series of works about VIV in 3D risers with a DNS method. He continued the VIV analysis with other works in 2012, 2013 and 2015. In these works, they analyzed all the important aspects of VIV in a 3D riser: vibration amplitude, vibration modes, vibration frequencies, drag and lift forces and synchronization phenomenon. The use of the DNS method restricted the Reynolds number to a maximum of 3K and the lack of experimental results were solved analyzing a dimensionless riser.

Zhao et al. (2011) presented a 2D case with RANS methods that he continued (2012). He analyzed the Reynolds values 1.5K and 3.0K. Zhao et al. (2014) presented a 3D case with RANS method.

Sun et al. (2012) presented a work with the potential DVM method. The last one published currently with such methodology.

Lothode et al. (2015) used a RANS method "in-house" developed tool to analyze a 3D riser for a Reynolds value of 4.5K.

Xiao and Wang (2016) presented a 3D riser work with the commercial tool firstly used by Menter (2006) to analyze four cases: two of uniform flow velocity and two of a sheared current and Reynolds number 4K and 8K.

Summarizing, plenty of work has being devoted to VIV but, due to physical and technical limitations, researchers focused until very recently mainly in rigid cylinders. The knowledge about flexible cylinders performance, as it is the case of riser and tension legs, is still limited. The main difference between these two cases (rigid or flexible cylinder) is that the first has a single structural oscillating frequency, meanwhile the last one has a spectrum of frequencies, spectrum that depends on the riser tension. Then, for the first case, the synchronization phenomenon can take place at its frequency, but for the elastic case, synchronization can take place at any frequency of the spectrum. This, besides that, in water and for high Reynolds numbers, tension cannot be easily calculated, makes that synchronization remains unexplained for elastic risers. It is the aim of this work to analyze this tension-frequency-synchronization relationship.

Besides, riser behavior depends on several parameters: length to diameter ratio, material density and Young´s modulus, and flow Reynolds number. Currently, one riser is taken and investigated at several Reynolds number, but prediction of the riser behavior for other parameter change is not possible. It is also the purpose of this work to analyze the effects of the variation of other parameter, out of the Reynolds number, in the riser behavior. More precisely, this parameter will be the Young´s modulus.

2.3. Physics model formulation

The solving of a Fluid-Structure Interaction (FSI) problem requires both the solving of the physics of the flow field in the fluid domain around the riser and the physics of the riser tension and deformation fields.

In the subchapter 2.3.1 the fluid domain governing equations that form the fluid dynamics model are presented. The subchapters 2.3.2, 2.3.3 and 2.3.4 are devoted, respectively, to the treatment of the turbulence phenomenon, the mechanical energy transported by the flow field that will be transferred to the riser, and the energy dissipation that will take place both in the fluid and the riser. Finally, subchapter 2.3.5 shows the solid domain governing equations which form the structure dynamics model.

2.3.1. Fluid governing equations.

The domain to be study in a FSI simulation is a fluid domain plus a solid domain, the riser. For the theoretical formulation the fluid domain, denoted as Φ_f is regarded. Its boundaries are three solid boundaries, one representing the seabed $\partial\Phi_b$, located at the domain bottom, another solid surface $\partial\Phi_s$, representing the platform moored by the riser, located at the domain top, and the third one the riser itself $\partial\Phi_r$, located in the interior of the domain. The fluid domain has also an inlet boundary $\partial\Phi_{in}$, an outlet boundary $\partial\Phi_{out}$ and two free-slip flow boundary conditions, one at each domain side, $\partial\Phi_{fs}$.

The fluid will be defined one-phase, incompressible and Newtonian fluid, representing water. The one-phase and incompressible Navier-Stokes's equations are:

$$div(\boldsymbol{V}) = 0 \tag{2.2}$$

$$\frac{D\boldsymbol{V}}{Dt} = f + \frac{div(\boldsymbol{\sigma})}{\rho} \tag{2.3}$$

Where 2.2 is the continuity equation and 2.3 is a set of three equations, the momentum equations (one in each domain dimension) and:

V is the velocity vector of velocity components (u, v, w), in the directions (x, y, z), respectively.

ρ is the fluid density.

f is the sum of the external forces and:

$\boldsymbol{\sigma}$ is the fluid stress tensor. As the fluid is of Newtonian type, the fluid stress tensor $\boldsymbol{\sigma}$ can be written as:

$$\boldsymbol{\sigma} = -p\boldsymbol{I} + 2\mu\boldsymbol{E} \tag{2.4}$$

Where p is the pressure, $\boldsymbol{I}$ is the 3rd order unity tensor (with value 1 in its diagonal and zero out of it). μ is the dynamic viscosity and $\boldsymbol{E}$ is the strain rate tensor defined as:

$$\boldsymbol{\sigma n} = -p\boldsymbol{n} + \mu(\boldsymbol{n}\times\boldsymbol{\omega}) + 2\mu\nabla\boldsymbol{V}\boldsymbol{n} \tag{2.5}$$

Where $\boldsymbol{\omega}$ is the vorticity, defined as $\boldsymbol{\omega}$ = curl($\boldsymbol{V}$) and the strain rate tensor is decomposed in two tensors, one antisymmetric and one symmetric by just forming the sums or the rests of the components of the tensor symmetric respect its diagonal. A more detailed development has been included in Appendix I.

On $\partial\Phi_r$, Eq. 2.5 becomes:

$$\boldsymbol{\sigma n_r} = -p\,\boldsymbol{n_r} + \mu\,(\boldsymbol{n}_r\times\,\boldsymbol{\omega}) + 2\mu\,\frac{\partial\,\boldsymbol{V}}{\partial\boldsymbol{n}_r} \tag{2.6}$$

Where the first component of the tension is the pressure component and the second and third components are friction stress components.

Hence, equation 2.3 takes finally the form:

$$\frac{\partial\,\bar{u}_i}{\partial t} + \bar{u}_j\frac{\partial\,\bar{u}_j}{\partial x_j} = -\frac{1}{\rho}\frac{\partial\,\bar{p}}{\partial x_i} + \frac{\partial}{\partial x_j}\left[\nu\left(\frac{\partial\,\bar{u}_i}{\partial x_j} + \frac{\partial\,\bar{u}_j}{\partial x_i}\right)\right] - \frac{\partial\tau_{ij}}{\partial x_j} \tag{2.7}$$

Where (x_1, x_2, x_3) = (x, y, z) are the Cartesian coordinates, the overbar denotes that the variable is a filtered variable, u_i is the velocity component in the x_i direction, p is the pressure, t is the time, ρ is the fluid density, ν is the kinematic viscosity of the fluid and τ_{ij} is the sub-grid-scale stress, defined as:

$$\tau_{ij} = \overline{u_i u_j} - \bar{u}_i \bar{u}_j \qquad (2.8)$$

And using the approximation for turbulent flows:

$$-\left(\tau_{ij} - \frac{\delta_{ij}}{3}\tau_{kk}\right) = 2\nu \overline{S}_{ij} \qquad (2.9)$$

Where δ_{ij} is the Kronecker symbol.

The governing equations are discretized using an element-based Finite Volume Method as it will be seen in section 2.4.

2.3.2. Model of turbulence

The simulations are run in a Reynolds range that makes the flow fully turbulent. This situation forces to add a turbulence model to the set of equations that forms the fluid dynamic model.

Among the different turbulence models that have been developed along time, the Shear Stress Transport, SST model of Menter (1994), has been chosen.

The reason to choose this model is that it is a mixed model of the two-equation k-ε and k-ω models. The k-ω model is known to be more accurate near walls meanwhile k-ε obtains better results in the bulk flow region, ANSYS Solver Theory (2016).

This model has been widely tested for VIV cases, where accuracy is required both in the boundary layer to achieve an accurate capture of the forces upon the riser, accuracy that is necessary to subject the riser to the correct force state and, hence, obtain from the structural model the correct deformation, Menter (2006), Lothode (2015). Therefore, the model becomes the k-ω model near the riser walls, eq. 2.10, 2.11 and 2.14, and the k-ε model far from the boundary layer eq. 2.12, 2.13 and 2.14:

$$\frac{\partial(\rho k)}{\partial t}+\frac{\partial(\rho u_i k)}{\partial x_i}=\frac{\partial}{\partial x_i}\left[\left(\mu+\frac{\mu_t}{\sigma_k}\right)\frac{\partial k}{\partial x_j}\right]+P_k-\beta\rho k\omega \tag{2.10}$$

$$\frac{\partial(\rho\omega)}{\partial t}+\frac{\partial(\rho u_i \omega)}{\partial x_i}=\frac{\partial}{\partial x_i}\left[\left(\mu+\frac{\mu_t}{\sigma_k}\right)\frac{\partial \omega}{\partial x_j}\right]+\alpha\frac{\omega}{k}P_k-\beta\rho\omega^2 \tag{2.11}$$

$$\frac{\partial(\rho k)}{\partial t}+\frac{\partial(\rho u_i k)}{\partial x_i}=\frac{\partial}{\partial x_i}\left[\left(\mu+\frac{\mu_t}{\sigma_k}\right)\frac{\partial k}{\partial x_j}\right]+P_k-\rho\varepsilon \tag{2.12}$$

$$\frac{\partial(\rho\varepsilon)}{\partial t}+\frac{\partial(\rho u_i \varepsilon)}{\partial x_i}=\frac{\partial}{\partial x_i}\left[\left(\mu+\frac{\mu_t}{\sigma_k}\right)\frac{\partial \varepsilon}{\partial x_j}\right]+\frac{\varepsilon}{k}(C_{\varepsilon 1}P_k-C_{\varepsilon 2}\rho\varepsilon) \tag{2.13}$$

Where P_k is the turbulence production due to viscous and buoyancy forces:

$$P_k=\mu_t\frac{\partial u_i}{\partial x_i}\left[\frac{\partial u_i}{\partial x_j}+\frac{\partial u_j}{\partial x_i}\right]-\frac{2}{3}\frac{\partial u_i}{\partial x_j}\left(3\mu_t\frac{\partial u_i}{\partial x_i}+\rho k\right)+P_{kb} \tag{2.14}$$

And where $C_{\varepsilon 1}$, $C_{\varepsilon 2}$, σ_k are model constants.

The convenience of also including a model for the local flow transition from laminar to turbulent has been considered. According to the software code handbook, together with Reynolds number range and the fact that riser wall will move making the relative movement between riser and flow to change of direction with riser movement showed that its inclusion was not recommendable.

The k-ω models assume that the turbulence viscosity is linked to the turbulence kinetic energy and turbulent frequency via the relation:

$$\mu_t = \rho \frac{k}{\omega} \tag{2.15}$$

Where μ_t is the turbulent viscosity, ρ is the fluid density, *k* is the turbulent kinetic energy defined as:

$$k = \frac{1}{2} \sum \overline{(u')_i{}^2} \tag{2.16}$$

Where:

$$\overline{(u')_i{}^2} = \frac{1}{T} \int_0^T (u_i(t) - \overline{u_i})^2)dt \tag{2.17}$$

And ω is the energy dissipation per kinetic energy unit, defined as:

$$\omega = \varepsilon / k \tag{2.18}$$

The k-ω based SST model accounts for the transport of the turbulent shear stress and gives highly accurate predictions of the onset and the amount of flow separation under adverse pressure gradients.

2.3.3. Mechanical energy

The power (energy per second) that the fluid flow (fluid mass per second) exerts on the moving body (riser), $P_{fluid/body}$ is obtained by integrating the power of the fluid stress acting on each body surface element:

$$P_{fluid/body} = -\int_{\partial\Phi r} \boldsymbol{\sigma_f}\, \boldsymbol{n}\cdot \boldsymbol{u} dS \qquad (2.19)$$

With $\boldsymbol{n}$ being the unit normal vector pointing outwards the fluid domain and σ_f the fluid stress tensor.

This fluid flow power is converted into an energy variation of the fluid and a body deformation energy that are equal to the net power variation between power entered and exited of the fluid domain P_{ext}. Hence, – $P_{fluid/body}$ = $P_{body/fluid}$ + $P_{body\ deformation}$ = P_{ext}. An equivalent way to define the power using the divergence theorem gives:

$$P_{ext} = \int_{\Phi f} div(\boldsymbol{\sigma_f n}) dV + \int_{\Phi s} \varepsilon^T \sigma_r \ dV_r \qquad (2.20)$$

Where the first integral of eq. 2.20 represents the fluid power and the second integral the riser deformation power and where ε is the riser strain field and σ_r is the riser stress field, T as superscript denotes the need of making the transpose matrix of the strain matrix and V_r denotes the volume of the riser body.

Using the divergence theorem, Eqn. 2.19 becomes:

$$\int_{\Phi f} (div\boldsymbol{\sigma_f}) \cdot \boldsymbol{n} dV = P_{ext} - \int_{\Phi f} \boldsymbol{\sigma_f} : \boldsymbol{E_f} \ dV_f - \int_{\boldsymbol{\Phi r}} \boldsymbol{\varepsilon} : \ \boldsymbol{\sigma_r} \ dV_r \qquad (2.21)$$

Which indicates that the fluid flow power (first integral in equation 2.21) is the power that exits the domain, P_{ext} minus the power dissipated in the fluid flow by viscous dissipation (second integral) minus the power dissipated in the body deformation (third integral).

Using momentum equation, the left side of Eqn. 2.21 can be written as:

$$\int_{\Phi f} (div\boldsymbol{\sigma})\cdot\boldsymbol{n}dV = \int_{\Phi f} \left(\rho\frac{D\boldsymbol{u}}{Dt} - \rho f\right)\cdot\boldsymbol{u}dV \tag{2.22}$$

The conservative body force is due to gravity ***g***, but, as there is no change of riser elevation, the work against or with gravity is null in our case.

Using the transport theorem and the continuity equation it is obtained:

$$\int_{\Phi f} (div\boldsymbol{\sigma})\cdot\boldsymbol{n}dV = \frac{D}{Dt}\int_{\Phi f} \rho\frac{\boldsymbol{u}^2}{2}dV \tag{2.23}$$

It can be defined:

$$\boldsymbol{\varepsilon_K} = \int_{\boldsymbol{\Phi f}} \frac{\boldsymbol{u}^2}{2}\rho dV \tag{2.24}$$

Therefore:

$$\int_{\Phi f} (div\boldsymbol{\sigma})\cdot\boldsymbol{u}dV = \boldsymbol{\varepsilon}_K \tag{2.25}$$

The second term of the equation 2.21 is the derivative of the internal energy and can be expressed for an incompressible fluid as:

$$\int_{\Phi f} \boldsymbol{\sigma}\,\mathbf{E}\,dV = 2\mu\int_{\Phi f} \boldsymbol{E} : \boldsymbol{E}\,dV \tag{2.26}$$

This represents the viscous dissipation term for a Newtonian fluid. It is always negative; hence the dissipative power in the fluid and in the riser can be defined as, respectively:

$$\boldsymbol{\varepsilon_{Df}} = -2\mu \int_{\Phi f} \boldsymbol{E} : \boldsymbol{E}\, dV_f \tag{2.27}$$

$$\boldsymbol{\varepsilon_{Dr}} = \int_{\Phi r} \varepsilon : \sigma_r\, dV_r$$

Hence, Eqn. 2.21 can be written as:

$$P_{ext} - \boldsymbol{\varepsilon_K} = \boldsymbol{\varepsilon_{Df}} + \boldsymbol{\varepsilon_{Dr}} \tag{2.28}$$

Hence, it can be inferred that: the power due to the external forces minus the kinetic energy of the fluid variation is balanced by the power dissipated by the fluid and the work of deforming the riser.

2.3.4. Dissipation

The total energy of a fluid stream is defined, following the classic Bernouilli's equation, as: $\boldsymbol{E} = \rho \boldsymbol{u}^2 + \rho g z + p$, to what viscous term must be added. Then, the mechanical energy balance on the domain $\boldsymbol{\Phi}$ is:

$$\boldsymbol{\varepsilon_M} = \boldsymbol{P}^{\boldsymbol{Kinetic}}_{\frac{\boldsymbol{body}}{\boldsymbol{fluid}}} + \boldsymbol{P}^{\boldsymbol{Pressure}}_{\frac{\boldsymbol{body}}{\boldsymbol{fluid}}} + \boldsymbol{P}^{\boldsymbol{Viscous}}_{\frac{\boldsymbol{body}}{\boldsymbol{fluid}}} - \int_{\Phi f} [\boldsymbol{E}\,\boldsymbol{n} + \mu(\omega \times \boldsymbol{n})]\cdot \boldsymbol{u} dS + \boldsymbol{\varepsilon}_{\omega} + \boldsymbol{\varepsilon}_{FS} \tag{2.29}$$

Where the terms in the equation right-hand side are defined as:

$$P^{Kinetic}_{body/fluid} = -\int_{\Phi_S} \rho \frac{u^2}{2} \boldsymbol{u} \cdot \boldsymbol{n} dS \tag{2.30}$$

$$P^{Pressure}_{body/fluid} = -\int_{\Phi_S} p\, \boldsymbol{u} \cdot \boldsymbol{n} dS \qquad (2.31)$$

$$P^{Viscous}_{body/fluid} = -\mu \int_{\Phi_S} (\boldsymbol{\omega} \times \boldsymbol{n}) \cdot \boldsymbol{u} dS \qquad (2.32)$$

$$\varepsilon_\omega = -\mu \int_{\Phi_S} \omega^2 \, dV \qquad (2.33)$$

$$\varepsilon_{FS} = -2\mu \int_{\Phi_S} (\boldsymbol{\nabla u}\, \boldsymbol{u}) \, dV \qquad (2.34)$$

Where ε_ω is the enstrophy, eq, 2.33, that can be interpreted as another type of potential density; or, more concretely, the quantity directly related to the kinetic energy in the flow model that corresponds to dissipation effects in the fluid bulk.

Regarding the solid surface boundary conditions and assuming horizontal local translation of the riser $V_r(z,t)$ (riser oscillation that depends on time *t*, and riser spanwise location *z*):

$$P^{Pressure}_{body/fluid} = V_r(z,t) \cdot F^{Pressure}_{body/fluid} \qquad (2.35)$$

$$P^{Viscous}_{body/fluid} = V_r(z,t) \cdot F^{Viscous}_{body/fluid} \qquad (2.36)$$

Where:

$$F_{body/fluid} = F^{Pressure}_{body/fluid} + F^{Viscous}_{body/fluid} \qquad (2.37)$$

Usually, the term of Eqn. 2.33, is the largest contribution in dissipative free surface flows, followed by the free-surface integral, Eqn. 2.34. But in the present case the free surface disturbances are not important, due to the free-surface distance to the element, therefore, the free-surface viscous term ε_{FS} is neglected.

Regarding a body oscillating in certain direction with velocity $v_B(t)$, and integrating over an oscillation period, Eqn. 2.29 becomes:

$$\int_t^{t+T} \varepsilon_M \, dt = \int_t^{t+T} v_B(t) \cdot F_{body/fluid} \, dt - \int_t^{t+T} \int_{\delta\Phi} [En + \mu(\omega \times n)] \cdot u dS dt + \int_t^{t+T} \varepsilon_\omega \, dt \quad (2.38)$$

After a whole cycle, the mechanical energy variation is null, as no plastic deformation or hysteresis are regarded, thus, implying that all the external power is dissipated by the fluid. The precedent expression then becomes:

$$\int_t^{t+T} v_B\,(t) \cdot F_{\frac{body}{fluid}} \, dt = \int_t^{t+T} \int_{\delta\Phi} [En + \mu(\omega \times n)] \cdot u dS dt - \int_t^{t+T} \varepsilon_\omega \, dt \quad (2.39)$$

It is convenient to note that if all the boundaries that limit the fluid domain are far enough from the body, the vorticity is diffused inside the domain and the vorticity term flux in RHS of Eqn. 2.39 can be neglected. In addition, and due to the large distance to the free surface, the oscillating riser does not irradiate energy through the generation of gravity waves, the term that goes with *E* can therefore also be neglected. The following expression for the present continuous model, exact under such assumptions, applies:

$$\int_t^{t+T} v_B\,(t) \cdot F_{body/fluid} dt = -\int_t^{t+T} \varepsilon_\omega \, dt \quad (2.40)$$

This equation demonstrates that the power exerted by the body on the fluid can be directly correlated to the net change in the enstrophy per cycle, as defined in eq. 2.33.

2.3.5. Solid governing equations.

When a solid is subjected to an external field of forces (volumetric or superficial) it deforms. Also, with that deformation (or, when made dimensionless with original dimensions, strain), a tension field inside of it appears to counteract the external force field (if tension is divided by the body section area perpendicular to the force, the stress is obtained).

There is a relationship between the stress field σ and the strain field ε. This relationship can be expressed generally as, Oñate (1992):

$$\sigma = D\ \varepsilon \tag{2.41}$$

Or, when the body is loaded from an initial tension-deformation state $(\sigma_o, \varepsilon_o)$:

$$\sigma = D\ (\varepsilon - \varepsilon_o) + \ \sigma_o \tag{2.42}$$

Where D is the stress-strain tensor and its inverse D^{-1} is known as the compliance matrix, which elements are:

$$\varepsilon_i = \left(\frac{1}{E_i}\right)\sigma_i - \left(\frac{\nu_{ji}}{E_j}\right)\sigma_j - \left(\frac{\nu_{ki}}{E_k}\right)\sigma_k \tag{2.43}$$

$$\gamma_{ij} = \frac{\tau_{ij}}{G_{ij}}$$

Where:

ε_i with $i = 1, 2\ 3$ are the body strain rates in the three coordinates directions x, y and z.

σ_i with $i = 1, 2\ 3$ are the body stress rates in the three coordinates directions x, y and z.

E_i is the Young modulus in the i coordinate direction. If the body is made of an isotropic material, that is, with equal properties in all directions, the three Young´s moduli are equal. Young modulus is the proportionality constant between the force applied to the body and its elongation.

ν_{ji} is the Poisson ratio. The Poisson ratio measures the stretching of the body section perpendicular to the applied force as body elongates. Due to mass continuity equation, as the body elongates in one direction, stretches in the perpendicular ones.

γ_{ij} is the shear strain. It is the deformation in the i direction when applying a force in the j face of a body differential element, see figure 2.1.

τ_{ij} is the shear stress. It is the force applied in the i direction and in the j face of a body differential element, see figure 2.1.

G_{ij} is the shear modulus that relates shear strain and shear stress.

As it can observed in figure 2.1, the shear stress is the result of a force applied in the body surface in a direction parallel to that surface meanwhile the named as stress is the result of a force applied in the body surface in a direction perpendicular to that surface.

Hence, strain-stress relationship plays the role of the continuity equation in solid physics model, that is, the conservation of mass, and volume, as solid material has fixed density.

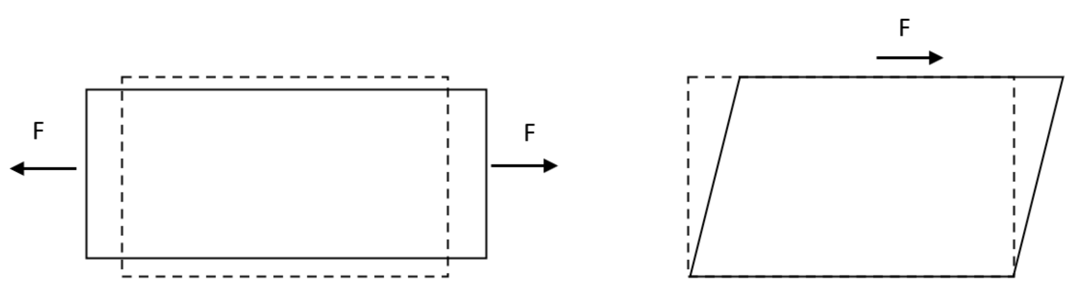

Fig. 2.1. Scheme of stress-strain normal (left) and tangential (right) relationships.

The second equation of the solid physics model is the conservation of energy. In the case of solids this role is played by the principle of the virtual works which equation is, Oñate (1992):

$$\iiint_V \partial \varepsilon^T \, \sigma \, dV = \iiint_V \partial u^T \, b \, dV = \iint_S \partial u^T \, t \, dS + \sum_i \partial a_i^T \, q_i \tag{2.44}$$

Where:

∂u is a virtual displacement vector (δu, δv, δw) in the coordinate's directions x, y and z.

And "following the classic theory of tridimensional elasticity the deformation vector in a point $\partial\varepsilon$ is defined by six components as:

$$(\partial\varepsilon_x, \partial\varepsilon_y, \partial\varepsilon_z, \partial\gamma_{xy}, \partial\gamma_{yz}, \partial\gamma_{xz},) =$$
$$(\partial u/\partial x, \partial v/\partial y, \partial w/\partial z, \partial u/\partial y + \partial v/\partial x, \partial v/\partial z + \partial w/\partial y, \partial u/\partial z + \partial w/\partial x) \tag{2.45}$$

Where ($\partial\varepsilon_x, \partial\varepsilon_y, \partial\varepsilon_z$) are the perpendicular deformations and ($\partial\gamma_{xy}, \partial\gamma_{yz}, \partial\gamma_{xz},$) are the tangential deformations", Oñate (1992).

b are volumetric forces, as mass forces.

t are surface forces, as flow drag force upon riser surface.

q are punctual forces, as reaction on riser clamping ends.

It must be noticed that this formulation is valid for materials in the elastic range, this is, that returns to the initial stress and strain situation when an applied force is no more applied and that do not experience hysteresis effects, that is, progressive deformation due to cyclic loads.

2.4. Simulation procedure

The fluid and solid governing equations presented in the subchapter 2.3 have no exact solution. Hence, to solve them, both fluid and solid physics models, as well as the geometry model where they apply, must be transformed in an algebraic mathematical model, transformation known as physics model discretization. The discretized models are the models solved by computers creating what is commonly known as a computational simulation.

In this subchapter 2.4 the different parts of the methodology used for the development of the simulations, and other required calculations carried out in this work by using the results obtained in the simulations, will be explained.

In the section 2.4.1 is presented the computational tool chosen to develop the numerical simulations. In the section 2.4.2 the discretization of the fluid physics model equations is explained. In the section 2.4.3 the analytical model used to calculate the riser oscillation frequency spectrum is described. This is the analytical model commonly used to predict the riser oscillation frequency spectrum, Bourget et al. (2011a) and Xiao and Wang (2016). This spectrum will be compared with the one resulting from the simulations. In this section it is also commented the existence of a divergence between the two spectra, the analytic and the one obtained from simulations. The explanation and correction of such divergence is a main aim of this work. To do so, drag force must be calculated. The method to calculate this force is explained in the section 2.4.4. In the section 2.4.5 is introduced the parameter that corrects the commented divergence: the flow-induced tension.

In the section 2.4.6 the discretization of the solid physics model equations is explained. Section 2.4.7 introduces the model of riser chosen for developing the simulations as well as its discretization, that is, the application of geometric and mathematical elements commented in the section 2.4.1 to this riser are explained.

Section 2.4.8 explains the post-processing methodology. This is, the treatment of the simulation results: flow velocity fields, riser shape along time and forces upon the riser, to obtain the required data of the variables studied in the VIV field.

Finally, section 2.4.9 shows the verification and validation procedures developed to ensure the simulations are correct and accurate.

2.4.1. Computational tool

The tool utilized to carry out the simulations has been the commercial software package ANSYS-MFX multi-field solver.

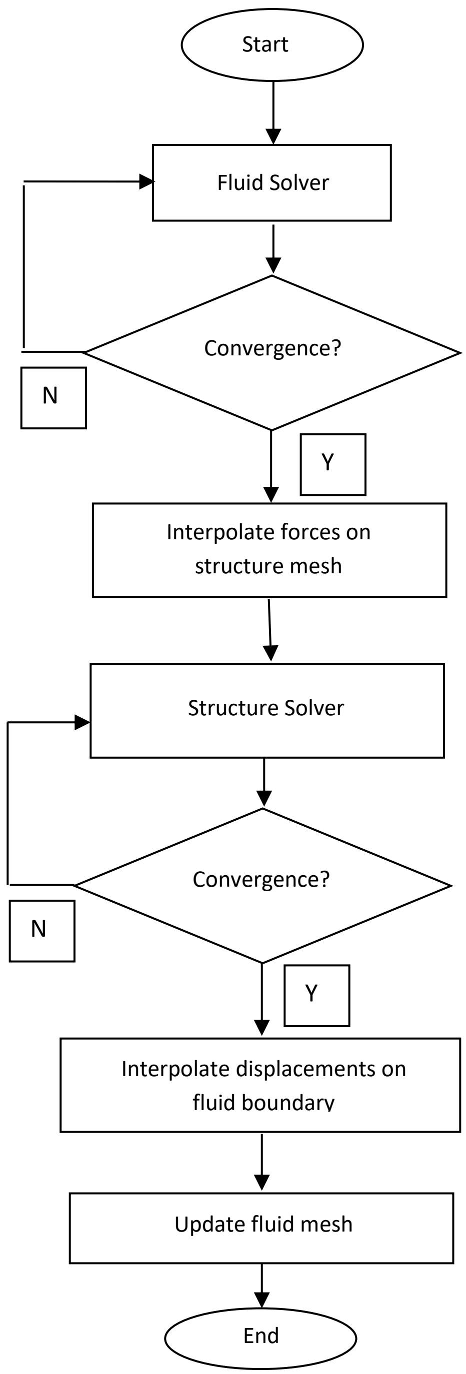

Fig. 2.2 Scheme of the FSI solver structure.

This tool is the result of the integration of the ANSYS fluid-dynamics tools: ANSYS-CFX or ANSYS-Fluent with the ANSYS structure calculation tool, named just ANSYS in its Transient Structural tool. In this work ANSYS-CFX was chosen due to its capabilities that will be explained in next subchapter 2.4.2.

The fluid-structure interaction is done, see figure 2.2, by means of a software tool, launched in the year 2006, that maps the fluid-dynamic pressure field of the riser surface that belongs to the fluid mesh upon the riser surface that belongs to the riser structure body. To do so, riser surface is meshed as an interface, that is, a double surface where one of its side belongs to one domain (the fluid domain) and the other to the second domain (the structural body domain).

The deformation of the structure with a pressure field was available in the ANSYS structural tool already from the '80. Also, the re-meshing of the fluid mesh as one of its surface boundary condition deforms was available in ANSYS-CFX years before.

In the case of this work, the riser is the solid domain. Its lateral surface will receive, see figure 2.2, at the end of the time-step solver iteration, the pressure field calculated in such iteration, which will be mapped onto this riser solid domain surface.

With this pressure field on the riser solid domain wall condition, and the condition of riser fixed at its extremes, the structure solver will find the riser deformation. Each of the flow solver iterations need some loops (set to a maximum of 10 loops per iteration) to end with the fluid domain reaching the temporal solution that complies a whole field of velocity, pressure, turbulence intensity and turbulence dissipation.

Also, the structural solver iterates until reaching a temporal converged solution (set to a maximum of 8 loops per iteration). The riser deformation is incorporated to the riser fluid-solid interface and both fluid and solid meshes are re-meshed with these new boundaries, ending in this way a complete FSI timestep iteration.

2.4.2. Numerical discretization of the fluid model and domain

To obtain a numerical solution of the Navier-Stokes's equations, CFX uses a discretization method which converts the differential equations into algebraic equations: The Finite Volume Method (FVM).

The FVM, as others, such as the finite element and finite difference methods, discretize the problem as follows:

- **Spatial discretization:** Consists of the division of the geometry domain into a set of points where the physics model approximated algebraic equations will be solved.
- **Temporal discretization** (For transient problems) or **Pseudo-temporal discretization** (for stationary problems): Consists of the division of the time domain into a finite number of time intervals, or steps. For transient problems, the simulation mathematical time step Δt corresponds with the physical time step (that one that will take the physical phenomenon to develop in reality). For stationary problems, the time step is a pseudo-time step required to reach a solution as the equation discretization requires iteration.
- **Equation discretization:** Consists of the generation of a system of algebraic equations in terms of discrete quantities defined at specific locations in the domain equivalent to the partial differential equations explained in the section 2.3.1, equations that characterize the problem.

The discretization methods developed in time are many. The ones used in the ANSYS fluid solver, CFX, for solving the fluid governing equations starts by considering the convection-diffusion governing equation of fluid flow which is the equation that must be discretized:

$$\frac{\delta}{\delta t}(\rho\phi) + \frac{\delta}{\delta x_i}(\rho v\phi) - \frac{\delta}{\delta x_i}\left(\Gamma_\phi \frac{\delta\phi}{\delta x_i}\right) = S_\phi \tag{2.46}$$

The equation 2.46 incorporates the processes by which a dependent variable ϕ is transported through the fluid. Hence, it is named a transport equation. The first term in the left-hand side of equation 2.46 is the transient term, the second is the convection term and the third one is the diffusion term. The continuity equation of the Navier-Stokes's equations is obtained by just considering ϕ = 1, with both Γ_ϕ and S_ϕ equal to zero. The momentum equations of the Navier-Stokes's equations are obtained by considering ϕ= *v*, being *v* the velocity and Γ_ϕ the viscosity and S_ϕ the sum of the forces acting on a fluid control volume.

The convection term of equation 2.46 represents the flux of the variable ϕ convected by the flow. The diffusion term represents the random motion of molecules due to the density gradients. The source term describes the production or destruction of ϕ and includes any process that cannot be represented by either the diffusion or the advection terms. Due to the non-linearity of the advection term, as it is a product of dependent variables, the governing equations must be solved by using an iterative method. As CFX is based on finite volume method (FVM), equation 2.46 is integrated over each control volume. The variables are stored at each control volume center.

By integrating equation 2.46 over a control volume and converting the diffusion and advection volume integral over the control volume surface *S* by using the Gauss Divergence theorem, it is obtained:

$$\int_V \frac{\delta}{\delta t}(\rho\phi)dV + \int_S (\rho v\phi)n_i\, dS - \int_S \Gamma_\phi \frac{\delta\phi}{\delta x_i} n_i dS = \int_V S_\phi\, dV \tag{2.47}$$

The above equation contains four terms which need to be discretized, that is, to be put in algebraic form instead of this differential form, from left to right: the transient term, the convection term, the diffusion term, and the source term. The momentum equation also contains a pressure term which does not satisfy a transport equation.

First term: transient scheme.

The first term is the transient term. It is discretized using a First Order Backward differencing scheme, Eq. 2.48a or a Second Order Backward scheme 2.48b:

$$\frac{dy}{dt} \approx \frac{y_i - y_{i-1}}{\Delta t} \quad \text{First order time backward} \qquad (2.48a)$$

$$\frac{dy}{dt} \approx \frac{y_i + 2y_{i-1} - y_{i-2}}{\Delta t^2} \quad \text{Second order time backward} \qquad (2.48b)$$

With the First Order Backward scheme, Eq. 2.48a, to find the variable values at current timestep y_i the former timestep values y_{i-1} are used. For the Second Order Backward Euler scheme, Eq. 2.48b, the two former timestep values y_{i-1} and y_{i-2} are used. The first order backward Euler scheme is more robust while the second order Euler scheme has higher order of accuracy. For the simulations this second order Euler was used.

Second and fourth terms: convection and sources.

The second and fourth terms of equation 2.47 do not present derivatives. They are calculated as the sum of fluxes over the surfaces of the control volume, see fig 2.3. Therefore, these three terms of equation 2.47 yield values of ϕ at the faces of the control volume. However, solution variables are stored at grid nodes (control volumes centers).

Hence, it is necessary to express the face values of ϕ in terms of adjacent nodal values. The method of specifying face values in terms of adjacent nodal values is called an advection scheme. The face value of a variable is calculated at an integration point from the variable value at the upwind node and the variable gradient. There are different advection schemes. The ones used in CFX are:

1. First order Upwind Differencing Scheme: This scheme is obtained by doing the blend factor zero. The blend factor is a weight-factor in the numerical iteration between the downwind and upwind nodes, chosen to balance the numerical method velocity and stability. Hence, when the blend factor is zero the variable value at an integration point is equal to its value at the upwind node meanwhile when blend factor is one the variable value is equal to the downwind node value. This scheme is first-order accurate and introduces discretization error due to numerical diffusion, but it is very robust as it does not result in non-physical values.
2. Numerical Advection Correction Scheme (Specify Blend): This scheme reduces the errors associated with the Upwind Differencing Scheme. In this scheme, the blend factor between 0 and 1 is chosen and the variable gradient is calculated as the weighted average of the adjacent nodal gradients. The first-order accurate scheme is obtained when blend factor is set to zero while second-order accurate scheme is obtained by setting the blend factor to 1. However, setting the blend factor to 1 produces non-physical oscillations in regions of rapid solution variation.
3. High Resolution Scheme: This scheme is intended to satisfy both accuracy and boundedness requirements by computing blend factor locally as to be as close to 1 as possible without resulting in non-physical values, while the variable gradient is set equal to the control volume gradient at the upwind node.

During the solution, correct pressure substituted into the momentum equation is indirectly taken in the continuity equation such that the resulting velocity must satisfy the continuity equation. Therefore, the calculations of pressure and velocity should be coupled. The pressure term is discretized by central differencing, where the pressure difference between the two lateral faces of the node of the control volume is calculated by using alternate nodal pressure values rather than adjacent ones.

This means that the oscillatory pressure field, for example, the pressure at consecutive grid nodes that might follow an alternating sequence, would be treated as a uniform pressure field since alternate grid points have the same value which could result in pressure-velocity decoupling.

However, this problem is overcome by adopting the Rhie Chow algorithm, ANSYS Inc. ANSYS Solver Theory Guide. Chapter 5 (2016).

Third term: diffusion scheme

The third terms represent the transport of the variable ϕ due to its spatial gradient (instead of the temporal variation of the first term). The derivative discretization is like that of the first term but:

- The subindices of the variable do not correspond to successive timesteps but to successive nodes of the special discretization.
- The timestep of the denominator changes for a "space step" corresponding with the characteristic length of the spatial discretization (the length of the element in which calculation domain is divided).

Therefore, the discretization of the different equation 2.47 terms requires the discretization of both time and space domains.

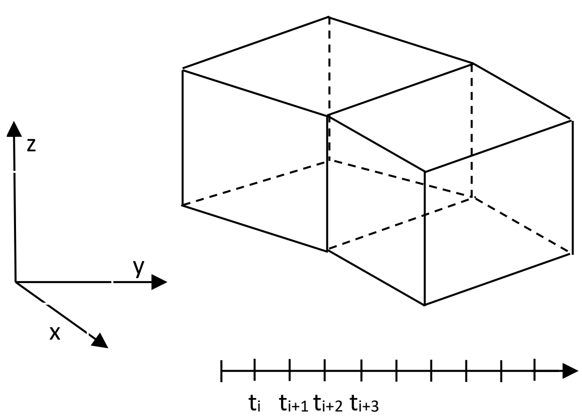

Fig. 2.3 Discretization of the solution domain

The discretization of the solution space domain can be observed in the figure 2.3. A computational mesh is developed, on which the governing equations are subsequently solved. It also determines the position of points in space and time (for transient problems with mesh deformation) where the solution is sought. Discretization of time, if required, is simple: it is broken into a set of time steps Δt that may change during a numerical solution, perhaps depending on some condition calculated during the simulation. The time step length is related with the algebraic equation system convergence by means of the Courant number, defined, for a one-dimensional case, as:

$$C = \frac{u\Delta t}{\Delta x} \leq C_{max}$$

Where:

u is the velocity magnitude (whose dimension is length/time)

Δt is the time step (whose dimension is time)

Δx is the length interval, related with cell characteristic length (whose dimension is length).

The value of C_{max} changes with the method used to solve the discretized equations, especially depending on whether the method is explicit (Fluent) or implicit (CFX). If an explicit (time-marching) solver is used, then typically C_{max} = 1. Implicit (matrix) solvers are usually less sensitive to numerical instability and so larger values of C_{max} may be tolerated.

For a 3D problem the Courant number is generalized to:

$$C = \frac{u\Delta t}{\Delta x} + \frac{v\Delta t}{\Delta x} + \frac{w\Delta t}{\Delta x} \leq C_{max} \tag{2.50}$$

Being (u, v, w) the velocity components in the (x, y, z) directions.

The discretization of space for the Finite Volume Method requires the subdivision of the domain into Control Volumes or Cells, figure 2.4. Cells must not overlap and completely fill the computational domain.

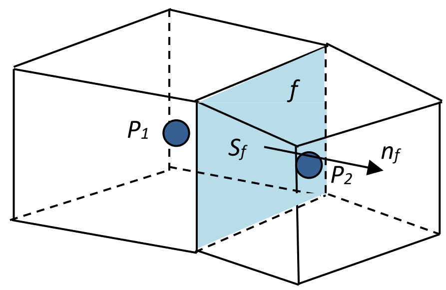

Fig. 2.4 Scheme of the Finite Volume Method

Each cell is surrounded by a set of faces and each face is shared with only one neighbor cell. The face area vector n_f is formed for each face in such a way that it points outwards from the cell and towards the neighbor one, is perpendicular to the face and has the magnitude equal to the area of the face S_f. For the shaded face, the cell and neighbor cell centers are marked with P and N, respectively. For simplicity, all the faces of the control volume will be subtitled as f, which also represents the point in the middle of the face, see figure. 2.4.

Variables and properties values are stored at the cell centroid ***P,*** although they may be stores on faces or vertices.

Different types of cells are available: hexahedra, tetrahedral, prisms or pyramids. Hexahedral cells form structured meshes. There are two definitions of structured mesh: that mesh where the inner nodes have the same number of elements around them or that mesh that follows a given topological pattern that is reproduced in all the directions of the space. These meshes are indicated for problems with a principal direction or having heat transfer.

The problems with mesh deformation, due to the movement of a boundary condition, do not show any improvement to use this type of mesh, as hexahedrons will deform losing their 90 degrees angles between their faces. For example, fluid-dynamic simulations of vortex shedding from rigid fixed bodies are more accurate with structures meshes but if the body is free to move then unstructured meshes are indicated, Oakley et al. (2008). Besides, producing hexahedral meshes is much more time cost, unless the geometry is quite simple. Therefore, tetrahedral meshes are chosen.

An important item of tetrahedral cell meshes is that they cannot capture the boundary layer that develops on surfaces. To capture this boundary layer, the zone upon the wall where this will be formed must be meshed with prisms.

Prisms cells are cells of triangular base and cell top parallel to base. The first prism layer base belongs to the wall surface. This first prism layer, according to the bulk velocity and turbulence model will require to fulfill a requirement to correctly capture the boundary layer and, together with it, the pressure field upon the wall surface. This requirement is named dimensionless wall distance, represented as y^+ and will be a criterion for verification. It is defined as:

$$y^+ = \frac{y u_\tau}{\nu} \qquad (2.51)$$

Where:

u_τ is the so-called friction velocity,

y is the absolute distance from the wall and

ν is the kinematic viscosity.

It can be interpreted as a local Reynolds number or cell Reynolds number.

The friction velocity u_τ can be defined as function of the shear stress and density as:

$$u_\tau = \sqrt{\frac{\tau_w}{\rho}} \qquad (2.52)$$

With:

$$\tau_w = \rho \nu \frac{d|U|}{dy}_{y=0} \quad (2.53)$$

When using a vorticity-based turbulence model, a k -ω model, as the case of the Shear Stress Transport (SST) model, the recommended value of y+ would be ~1. The k -ω modes, also named low-Re models, are the recommended to achieve a good capturing of boundary layer, pressure drop or drag calculations, as it is the case of achieving an accurate pressure field on the riser surface.

2.4.3. Fluid-structure interaction modeling of a riser.

The phenomenon of VIV on risers were studied formerly forcing risers to move following harmonic oscillations as it has been explained in the literature review in section 2.2**.** This was due to both physical and computational limitations. However, riser oscillation is a free oscillation induced by the flow with neither frequency nor amplitude known a priori.

An a priori estimation of the frequency spectra has been developed but still is not accurate. The first proposed model predicted correctly for elements working in a gas fluid, usually air. This formulation is, Weaver et al. (1974):

$$f_{n,t-beam} = \sqrt{f_{n,string}^2 + f_{n,beam}^2} \quad (2.54)$$

Where n = 1, 2, … n is the mode number and:

$$f_{n,string} = \frac{n}{2}\sqrt{\frac{T}{mL^2}} \quad (2.55)$$

And:

$$f_{n,beam} = \frac{n^2 \pi}{2}\sqrt{\frac{EI}{mL^4}} \quad (2.56)$$

These equations fail completely for the case of bodies immersed in liquids. It was not until Khalak and Williamson (1999), who introduced the added mass into the formulation that accuracy for elements vibrating in liquids improved significantly meanwhile Reynolds number remains not high. Such correction is:

$$\sqrt{\frac{m}{m+\frac{\pi}{4}C_m}} \tag{2.57}$$

That multiplies the equation of the frequency range$f_{n,t-beam}$, Eqn. 2.54, and where the added mass coefficient C_m was taken as the potential flow solution value of 1.

With this correction, the frequency estimation is correct at low Reynolds numbers but diverges from experimental results when the Reynolds number increases, Chaplin et al. (2005). It is a purpose of the present thesis to introduce a new factor, the flow induced tension, to correct this divergence.

This factor is defined as follows: the riser does not vibrate from its position and shape at rest (with no flow acting upon it) but, after a transient period of riser deformation and oscillation. The oscillations produced by vortex shedding vibrations, VIV, take place on a fixed deformation cylinder. This deformation is the response of the cylinder to flow drag force. This body deformation field has associated a body tension field, Gere and Timoshenko (1998). **It is this tensioned cylinder the body that will vibrate due to the vortex shedding.** The vortex shedding frequency will be that given by the Strouhal number, and the structure natural oscillation frequency will be that of the tensioned cylinder. Hence, synchronization will occur when vortex shedding frequency locks to the natural frequency of the tensioned riser, not of the riser at rest.

To calculate the flow induced tension we should start taking a body immersed in a flow. This body will experience a force, named drag force of value:

$$F_D = 0.5\, \rho\, C_D\, S\, V^2 \tag{2.58}$$

Where:

F_D is the drag force,

ρ is the fluid density,

C_D is the drag force coefficient,

S is the body surface facing the flow and

V is the flow velocity.

The drag force coefficient C_D is a constant value for rigid bodies, but not for elastic bodies that deform. The drag force coefficient value for oscillating risers is larger than that of a fixed cylinder and varies with the Reynolds number, Bourghet et al. (2011), Resvanis et al. (2012), Lothode et al. (2016).

Hence, the drag coefficient must be calculated.

2.4.4. Drag force coefficient calculation

As the vibration mode and oscillation amplitude of a riser changes with the Reynolds number, the velocity that faces each spanwise point (the sum of the flow velocity and the local and instantaneous relative velocity of that point) varies with time, so does the force and the drag coefficient. Hence:

$$\partial F_z(t) = 0.5\,\rho\,C_{D,Z}(t)\,D\,V_{flow,z}(t)^2 \tag{2.59}$$

Therefore, to calculate the riser coefficient drag force for a given Reynolds number the force at each spanwise section *z* and time *t* is obtained from the corresponding FSI simulation. Then, the time-averaged local drag force is obtained integrating the local force along an oscillating period, thus:

$$\partial F_z = \int_t^{t+T} \partial F_z\,(t)dt \tag{2.60}$$

As in a period *T*, at any spanwise point, the riser movement, velocity, and acceleration make a whole cycle, for the case of the velocity:

$$\overline{V_z} = \frac{1}{T}\int_t^{t+T} V\,(t)dt = \frac{1}{T}\left(\int_t^{t+T} V_{flow}\,(t)dt + \int_t^{t+T} V_{riser}\,(t)dt\right) = V_{flow} \qquad (2.61)$$

What indicates that, for any spanwise point, the velocity taken to define the drag force coefficient remains being the flow velocity as in the case of fixed rigid body.

Then, calculating the force with Eqn. 2.60, and operating in the way of obtaining the force coefficient by length unit:

$$C_{D,Z} = \frac{\partial F_z}{0.5\,\rho\,D\,V_{flow,z}(t)^2} \qquad (2.62)$$

Following this methodology, it will be found from simulations the drag coefficient distribution along the riser length. This distribution allows analyzing the correspondence between riser average deformation and the force that produces such deformation.

Once obtained the drag coefficient distribution on the riser, the riser drag coefficient is calculated by integrating along the riser length:

$$C_D = \frac{1}{L}\int_0^L C_{D,Z}\,(z)dz \qquad (2.63)$$

It is worth to say that, in the same way that Khalak and Williamson (1999) proposed a value for the added mass coefficient of 1, result of the potential analysis of the body immersed in a fluid, that is not exact, as added mass coefficient depends on both flow velocity and oscillation frequency and amplitude, the constant value for drag force coefficient is not exact either. But, as an average value the added mass coefficient of 1 has shown as valid and allowed a significant improvement on frequency range estimation, Govardhan and Khalak (2006). **The same**

philosophy is proposed to be used for the flow induced tension where, according to the results that will be shown in chapter 5, an average value for the drag coefficient can be taken.

With this drag coefficient value the tension produced by the flow on the riser will be calculated as follows.

2.4.5. Flow induced tension calculation

The average riser deformation produced by the drag force is sometimes represented as a simulation or experimental test result, Bourghet et al. (2011), Lothode et al. (2015), in form of a figure showing the riser average deformed shape, but is not analyzed, see figure 2.5 for a typical riser deformation curve. The present work considers that this curve should be analyzed as provides the data to define a new term that the author considers the main source of discrepancy between frequency numerical estimation and frequency tests results when Reynolds number increases.

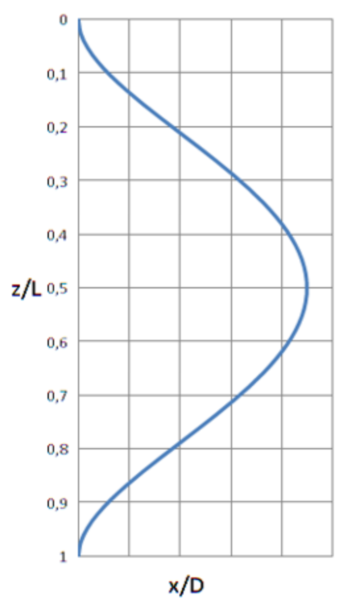

Fig. 2.5 Typical dimensionless riser in-line average deformation curve.

The riser deformation supposes a local bending of each riser section *z* respects to one infinitesimally proximate section *z+dz,* that is, a curvature and, regarding that the riser two extremes are fixed and that all intermediate section separates from their straight position, an elongation. Whether the average curvature or the elongation produces a higher tension state, that is, whether the flexion stress or the tensile stress is more significant, is the aim of the next brief analysis.

Table 2.2 shows L/D data and maximum deviation results, that is, the maximum deviation of their curve analogue to that shown in figure 2.5 of Bourghet et al. (2011) and Lothode et al. (2016) works. The values obtained from the simulations carried out for this thesis have been already included, it can be observed that the maximum deviation from the initial straight position is always small in comparison to riser length. In fact, this parameter is smaller as more rigid is the riser.

Table 2.2 Maximum deviation of the riser slope slide curve as function of Reynolds number. In the third column is shown made dimensionless with the riser diameter and in the fourth column by the riser length.

Reynolds n.	**L/D**	**X_{max}/D**	**X_{max}/L**	**Source**
1100	200	12.00	6,00e-2	Bourghet et al.
4500	468	1.15	2.46e-3	Lothode et al.
42000	475	0.10	2.11e-4	Present work
84000	475	0.15	3.16e-4	Present work
126000	475	0.17	3.58e-4	Present work

As real risers, to keep platform at their positions, are to be very rigid, the dimensionless deviation is to be extremely small. Thus, riser remains “almost” straight. Hence, regarding the tension as a tensile tension is an acceptable assumption.

Hence, tension will be calculated with the equation of the tensile stress:

$$\varepsilon = \frac{\Delta L}{L} = \frac{\sigma}{E} \tag{2.64}$$

Where σ = *T/A*, being *T* the riser tension to be obtained and *A* the riser section area. *L* is the riser length, ΔL is the riser elongation and *E* is the riser material Young´s modulus.

Later, to obtain the flow induced tension, known the geometrical characteristics of the riser: length *L* and section area *A,* and the material property Young modulus *E,* it is only required to calculate the riser elongation ΔL from the riser deformed curve. Hence, two methods are proposed to calculate such elongation:

- To measure the elongation in the FSI simulation results.
- To calculate with structure calculus of a both ends clamped/connected by ball joints beam with constant force distribution or lineal force distribution. The constant force ***F*** distributions correspond to uniform flows and the linear force distributions correspond to shear flows as, for a riser section at spanwise position *z,* the drag force produced by the flow at such section is calculated with equation 2.60. ***The aim of this method is to have a pre-design procedure that, without carrying out simulations, could give an approximate value of the VIV frequency spectrum.***

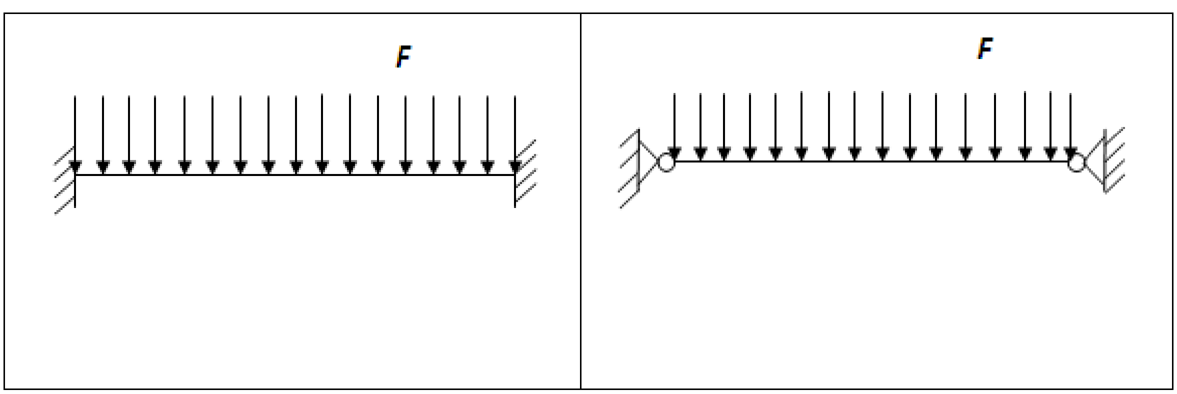

Fig. 2.6 Scheme of the riser force distribution when drag force is produced by a uniform velocity distribution.

The shape of the slide-slope curve for the beam supported on its two extremes, figure 2.6 right, is given by the equation 2.65, Gere and Timoshenko (1998). An equivalent equation can be found for the case of the beam with clamped ends, figure 2.6 left, where, for a riser, the need of using one or the other depends on the type of riser anchoring to sea bottom and to the platform.

If the anchor might rotate around its anchoring point:

$$x(z) = -\frac{Fz}{24EI}(z^3 - 2Lz^2 + L^3) \tag{2.65}$$

Where *F* is the force per unit length produced by the drag force. The first and second derivatives of this equation will be needed as it will be seen next. The first derivative is:

$$x'(z) = -\frac{F}{24EI}(4z^3 - 6Lz^2 + L^3) \tag{2.66}$$

And the second derivative is:

$$x''(z) = -\frac{F}{2EI}(z^2 - Lx) \tag{2.67}$$

The first derivative is used in the following way: the length of the deformed riser can be found as the length integral of any curve, which is given by the equation:

$$L_{deform} = \int_0^L \sqrt{1 + [x'(z)]^2}\, dz \tag{2.68}$$

Regarding that the elongation *ΔL* to be entered in the equation 2.64 is:

$$\Delta L = L_{deform} - L \tag{2.69}$$

The tensile tension is found.

It was considered the incorporation of the stress due to flexion, which is given by, Gere and Timoshenko, (1988):

$$\sigma_i = E\,\varepsilon_i \tag{2.70}$$

Where *i* is the coordinate *x* for the in-line direction and the coordinate *y* for the crossflow direction and where:

$$\varepsilon_x = -\frac{D}{2}\left(\frac{x''(z)}{1 + x'(z)^2}\right) \tag{2.71}$$

Where *D* is the riser diameter.

But the flexion stress does not produce a net stress on the body sections but a compression tension in a part of the riser section and a tensile tension in the rest of the section, these zones are separated by what it is known as the neutral axis.

Hence, flexion does not produce a net elongation and, therefore, neither a net tension, but local tension of different sign (tensile or compression). These tensions, as varying with time with riser oscillation, may cause a fatigue problem on the structure but, being of sum zero, will not produce a net tension neither a change in structure frequency range.

2.4.6. Numerical discretization of the solid modeling equations

The structural model is the usual of a transient analysis of a solid piece. This mathematical model consists of the use of block type elements. The numerical model is that of an iterative process where for each time step is solved the element stiffness matrix with the boundary condition of fixed ends and pressure field upon its lateral surface. The pressure field is calculated in the fluid-dynamic part of the FSI model. The solution for a certain time step is used as an initial estimator for the next one.

According to Huang et al. (2011a) and Jhingran et al. (2008), the equation of a riser can be taken as that of a tensioned beam, whose flow direction, IL, and lateral motion, CF, are described, respectively, as:

$$\frac{\partial^2}{\partial z^2}\left[EI\frac{\partial^2 x}{\partial z^2}\right]-\frac{\partial}{\partial z}\left[T\frac{\partial x}{\partial z}\right]+(m(z)+m_a(z))\frac{\partial^2 x}{\partial t^2}+c\frac{\partial x}{\partial t}=F_x \qquad (2.72a)$$

$$\frac{\partial^2}{\partial z^2}\left[EI\frac{\partial^2 y}{\partial z^2}\right]-\frac{\partial}{\partial z}\left[T\frac{\partial y}{\partial z}\right]+(m(z)+m_a(z))\frac{\partial^2 y}{\partial t^2}+c\frac{\partial y}{\partial t}=F_y \qquad (2.72b)$$

Where *EI* is named structural flexibility, being *E* the Young's modulus and *I* the riser section moment of inertia, the same one for IL and CF motions as riser section is a circle, *T* is the riser tension, *m* is the mass per length unit, m_a the added mass per length unit, also the same for IL and CF motions for the same reason that in the case of the inertia moment, *c* is the structural damping, *z* is the non-deformed riser axial direction, *x* denotes the flow in-line, IL, direction, *y* the cross-flow, CF, direction. F_x are the hydrodynamic forces in the IL direction, which is formed by both the flow drag force plus the periodic vortex shedding force IL component, and F_y is the hydrodynamic forces in the CF direction, which is the periodic vortex shedding force CF component.

But, coming back to the equations 2.80a and b, a finite element method must be used to discretize these equations obtaining the governing equation set in a form like follows:

$$[M]\{\ddot{x}\}+[C]\{\dot{x}\}+[K]\{x\}=\{F\} \qquad (2.73)$$

Where $\{x\}$ is the distance that the riser nodes move in the three space dimensions $\{x, y, z\}$, $\{\dot{x}\}$ is the velocity vector and $\{\ddot{x}\}$ the nodal acceleration vector of the riser mesh nodes. [M], [C] and [K] are the mass, damping and stiffness matrices, respectively. $\{F\}$ is the hydrodynamic force vector. The governing equation is solved using the Hilber-Hughes-Taylor (HHT) method.

The ANSYS Transient Structural Analysis solver solves the general form of equation 2.73 in the following way, ANSYS Solver Theory Guide. Chapter 5 (2016). As the external force *F* is a time-depending force, it uses a direct integration method (an implicit integration method) to calculate the dynamic response. The implicit integration method works fine with structures excepting in the case of high-speed impact simulations, that require extremely small timestep unless using an explicit integration method.

Regarding that the movement of the riser elements in the domain corresponds with riser model nodes displacements, let´s change the physical vector of movements, x in eq. 2.73 for the mathematical vector of node displacement D, hence:

$$M\{\ddot{D}\} + C\{\dot{D}\} + K\{D\} = \{F\} \tag{2.74}$$

Now, considering a typical time step at t_n. Let D_n, $\dot{D}_n$ and $\ddot{D}_n$ the displacement, velocity, and acceleration at t_n, and D_{n+1}, $\dot{D}_{n+1}$ and $\ddot{D}_{n+1}$ be those at t_{n+1}. Also, let $\Delta t = t_{n+1} - t_n$. Assuming that the acceleration is linear over the time step (i.e., $\ddddot{D}_n = D_n^{4\cdot} = etc = 0$), then, by Taylor series expansions at t_n:

$$\dot{D}_{n+1} = \dot{D}_n + \Delta t\ddot{D}_n + \frac{\Delta t^2}{2}\dddot{D}_n \tag{2.75}$$

$$D_{n+1} = D_n + \Delta t\dot{D}_n + \frac{\Delta t^2}{2}\ddot{D}_n + \frac{\Delta t^3}{6}\dddot{D}_n$$

The quantity $\dddot{D}_n$ can be approximated by:

$$\dddot{D}_n = \frac{\ddot{D}_{n+1} - \ddot{D}_n}{\Delta t} \tag{2.76}$$

Substitution of equation 2.76 into equations 2.75 yields:

$$\dot{D}_{n+1} = \dot{D}_n + \frac{\Delta t}{2}\left(\ddot{D}_{n+1} - \ddot{D}_n\right) \tag{2.77}$$

$$D_{n+1} = D_n + \Delta t\dot{D}_n + \Delta t^2\left(\frac{1}{6}\ddot{D}_{n+1} + \frac{1}{3}\ddot{D}_n\right)$$

Equations 2.77 can be regarded as a special case of Newmark methods, ANSYS Solver Theory Guide. Chapter 5 (2016):

$$\dot{D}_{n+1} = D_n + \Delta t\left[\gamma\ddot{D}_{n+1} + (1-\gamma)\ddot{D}_n\right] \tag{2.78}$$

$$D_{n+1} = D_n + \Delta t\dot{D}_n + \frac{1}{2}\Delta t^2\left[2\beta\ddot{D}_{n+1} + (1-2\beta)\ddot{D}_n\right]$$

When γ=1/2 and β= 1/6, equations 2.78 become equations 2.77.

Equations 2.78 are used in transient structural analysis systems. The parameters γ and β are chosen to control characteristics of the algorithm such as accuracy, numerical stability, etc. It is called an implicit method because the calculation of $\dot{D}_{n+1}$ and D_{n+1} requires knowledge of $\ddot{D}_{n+1}$, that is, the response of the current time step depends on not only the historical information but also the current information. Iterations are needed to solve equations 2.78.

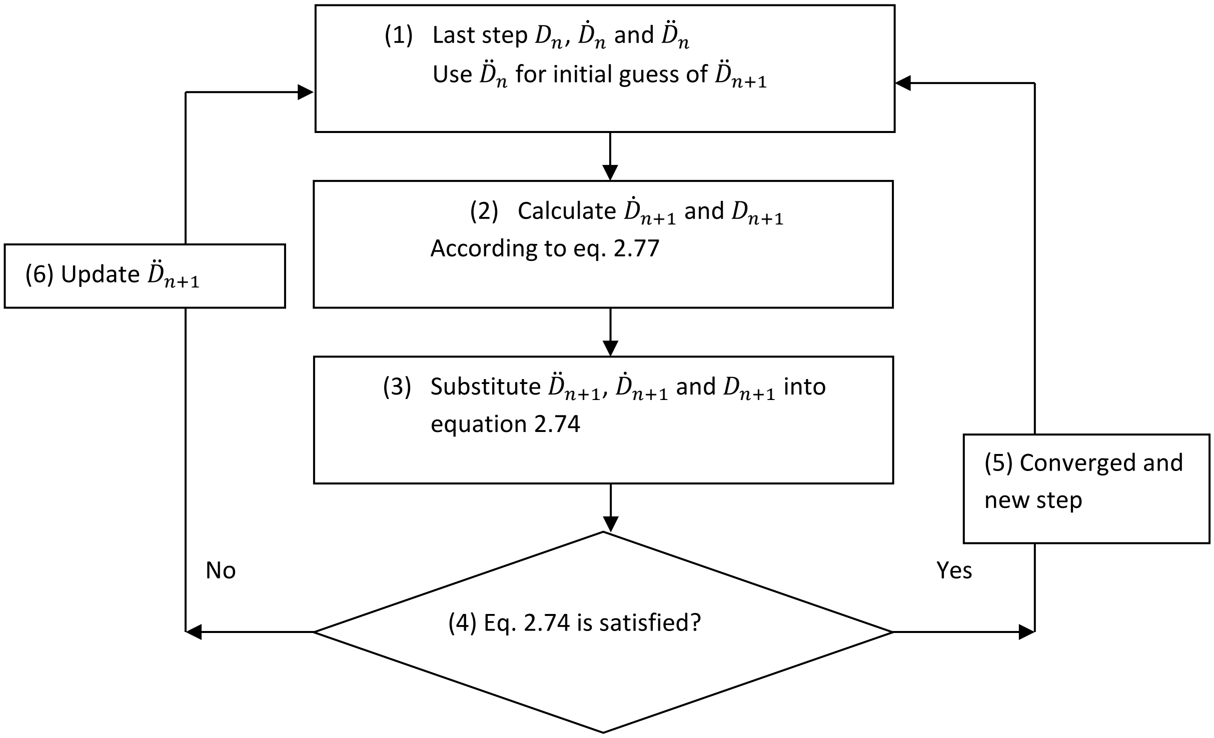

Fig. 2.7. Flowchart of the transient structural analysis.

Calculation of the response at time t_{n+1} is depicted in the chart of figure 2.7. In the beginning (1) the displacement D_n, velocity $\dot{D}_n$ and acceleration $\ddot{D}_n$ of the last step are already known (For n=0, it is assumed $\ddot{D}_0 = 0$). Since $\ddot{D}_{n+1}$ is needed in equations 2.77, $\ddot{D}_n$ is used as an initial guess of $\ddot{D}_{n+1}$. Knowing D_n, $\dot{D}_n$ and $\ddot{D}_{n+1}$, the quantities $\dot{D}_{n+1}$ and D_{n+1} can be calculated according to 2.77 (2). The next step (3) is to substitute $\ddot{D}_{n+1}$, $\dot{D}_{n+1}$ and D_{n+1} into equation 2.74. If the equation 2.74 is satisfied, then the calculation of the response at time t_{n+1} is complete (5). Otherwise, $\ddot{D}_{n+1}$ is updated and another iteration is initiated (6). Update of $\ddot{D}_{n+1}$ (6) is like the Newton-Raphson method described next.

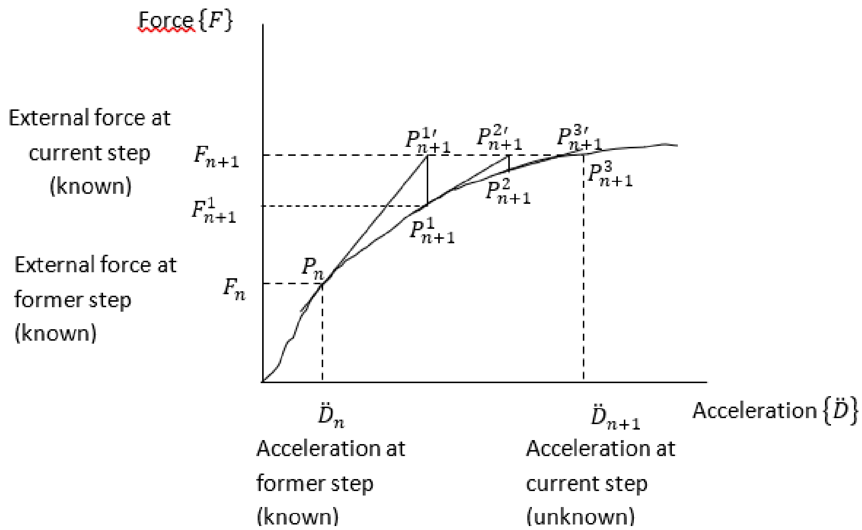

Fig. 2.8. Scheme of the Newton-Raphson method for transient structural analysis convergence.

The Newton-Raphson method, see figure 2.8, is used in the following case: supposing that the simulation has converged at the iteration of time step *n* and proceeds to the new current time step *n+1* at which the displacement is D_{n+1}, the velocity $\dot{D}_{n+1}$, the acceleration $\ddot{D}_{n+1}$ with the external force F_{n+1}. The point P_{n+1} represents the point at the response curve described by equation 2.74, but being this equation not satisfied with the value of the acceleration $\ddot{D}_{n+1}$, the point obtained is actually P_{n+1}^1.

To find the correct value of $\ddot{D}_{n+1}$, ANSYS calculates a “tangent mass”$[M]$, the linearized mass, and solves the following equation:

$$[M]\{\Delta\ddot{D}_{n+1}\} + C\{\dot{D}_{n+1}\} + K\{D_{n+1}\} = \{F_{n+1}\} \qquad (2.79)$$

The acceleration $\ddot{D}_{n+1}$ is increased by $\Delta\ddot{D}_{n+1}$ to became $\ddot{D}_{n+1}^1$. Now, in the $\ddot{D} - F$, the new point is $P_{n+1}^{1\prime}$ defined by the coordinates ($\ddot{D}_{n+1}^1$, F_{n+1}), but it is far from the goal P_{n+1} located in the actual response curve.

Substituting the acceleration $\ddot{D}'_{n+1}$ into the governing equation 2.74 it can be calculated the internal force F^1_{n+1}. Now, the point P^1_{n+1} ($\ddot{D}^1_{n+1}$, F^1_{n+1}) can be located and it is in the actual response curve. The difference between the external force F_{n+1} and the internal force F^1_{n+1} is called the residual force of that equilibrium iteration:

$$F^R = F_{n+1} - F^1_{n+1} \tag{2.80}$$

If the residual force is smaller than the convergence criterion, then the sub-step is said to be converge, otherwise iteration is required.

2.4.7. Riser geometry domain model

In the image on the right side of Fig. 2.9 can be observed the riser in its initial situation, straight, without the deformation that it will experience as it will deflect towards the current downstream after the flow field develops the pressure field and corresponding drag force upon its surface.

The riser is fixed in its two extremes to the domain bottom and top, which regard seabed and platform bottom, respectively.

The domain two lateral walls are far enough to the riser wall as to have no influence in the riser behavior by avoiding the appearance of a blocking effect. This distance is regarded to be 10 diameters. Besides, these surfaces are defined as free-slip boundary condition, so no boundary layer will grow upon them.

The domain front face is defined with an inlet condition, located 10 diameters before the riser. Thus, perpendicular to it, inwards to the domain a velocity field is defined of the velocity value regarded in each case. In the present work the velocity field is constant as it is already known that constant velocity cases produce larger riser deformations, Resvanis et al. (2012).

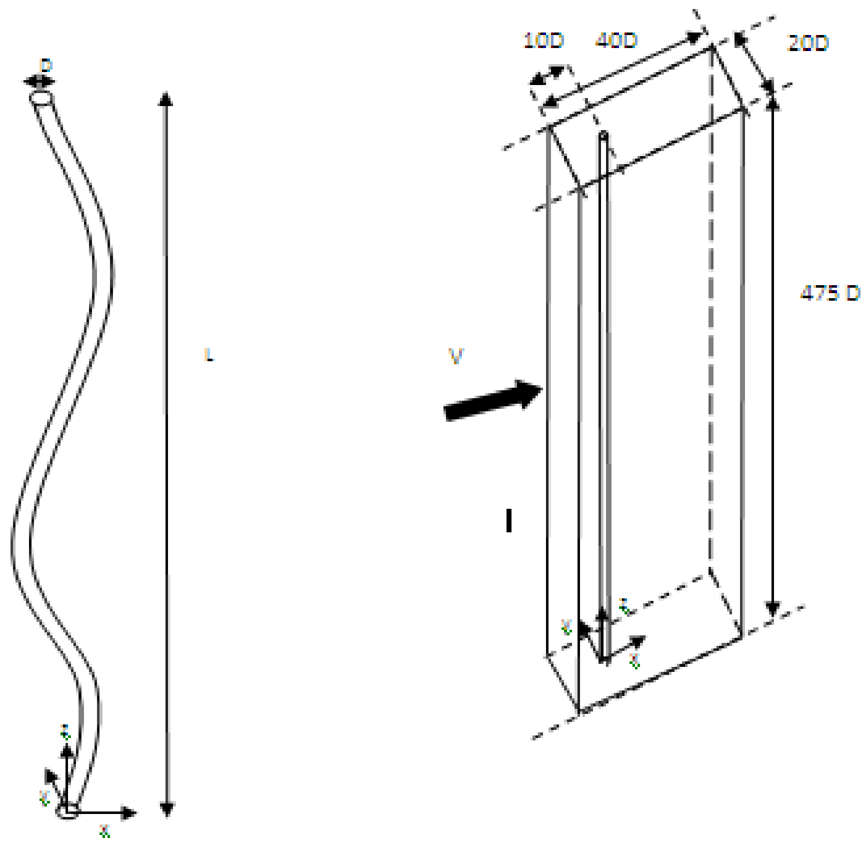

Fig. 2.9. Image of the riser with deformation (left) and the riser within the fluid domain at initial instant (right).

The domain back face is defined with an outlet condition. This condition must allow the flow outgoing with the local and temporal velocity, pressure and vorticity variations produced by the effect of the riser oscillation. To do so, 30 diameters downstream the riser are considered.

The riser surface is defined as an interface. This condition consists of two coincident conditions, one belonging to one of the domains (the fluid domain) and the other belonging to the other domain (the riser solid domain). The fluid domain side is defined as a no-slip wall boundary, allowing in this way to develop the flow boundary layer and the corresponding pressure field upon it.

2.4.8. Post-processing methodology

Numerical tests developed for this work must be post-processed to obtain the results shown in chapters 3 to 7. The post-process was carried out by using two different tools: the ANSYS-CFX tool and the Fast Fourier Transform (FFT). The ANSYS-CFX tool was used to extract coordinates, velocities and forces at different spanwise sections of the risers.

Having the riser, a diameter, the *x* and *y* positions of each *z* spanwise position have been represented by the section center calculated as the area average of the *x* and *y* coordinates of the section, thus:

$$\bar{x}_i = \iint_{A_j} x dA = areaAve(x_i)@section\_j \qquad (2.81)$$

Where the integral expression represents the physical variable, and the right-side expression represents the post-processing tool expression. In the same way can be obtained the velocity vector components for the same riser sections:

$$\bar{V}_{x_i} = \iint_{A_j} V_i dA = areaAve(u_i)@section\_j \qquad (2.82)$$

For the case of the force upon a riser section, the total force, the section normal force (due to the pressure field) or the tangential pressure (due to shear) can be obtained.

So, for the case of the total pressure and shear force:

$$F_{X_i} = \iint_{A_j} \left(P + \mu \frac{\delta u}{\delta \boldsymbol{n}_i}\right) dA \boldsymbol{n}_{A_i} = force_{x_i}@section\ j \qquad (2.83)$$

As frequency domain analysis has been carried out to determine the riser oscillating frequency values, a Fast Fourier Transform (FFT) tool has been used. The advanced options of the Excel data sheet include this tool. The FFT is an algorithm that takes data of a signal in the domain of time and converts it to the frequency domain.

2.4.9. Verification and validation of the numerical procedure.

Before running the simulations aim of the research work some other simulations to verify and validate the methodology must be carried out. Verification and validation are not synonymous but different things, in this way:

- Verification is done to a software code, to check that is robust and its results can be repeated (robustness and repeatability).
- Validation is done to any work results (numerical or experimental) by comparing them with other results taken as valid ones.

A correct validation for the case of simulations is to simulate a similar case and obtaining close results, hence, the results can be taken as validated. That was the way taken by Xiao and Wang (2016), who, for simulating a riser in the Reynolds number range of 4K to 8K previously check the methodology by simulating Huang et al. (2011a) riser, a riser of similar characteristics and in a remarkably close Reynolds number range. Nevertheless, being its work interesting, she did not find any "new knowledge" out of what Huang found. Among the four cases simulated by Xiao and Wang (2016), the closest one to the cases analyzed in this work was taken for validation purposes. This case is the one with uniform flow pattern and highest Reynolds number (about 8K).

But, as the case taken for validation purpose and cases for the work were quite far in several of its parameters, it was considered to develop firstly a verification procedure, following the theory of numerical flow simulation to check the different parameters involved in the simulations.

Hence, verification has been carried out at different stages. First, it was verified the mesh characteristics: first prism layer thickness to obtain a correct y^+, and number of prism layers and tetrahedral cell size to correctly capture the riser motion. Later, the value of the required time-step for the simulations was analyzed.

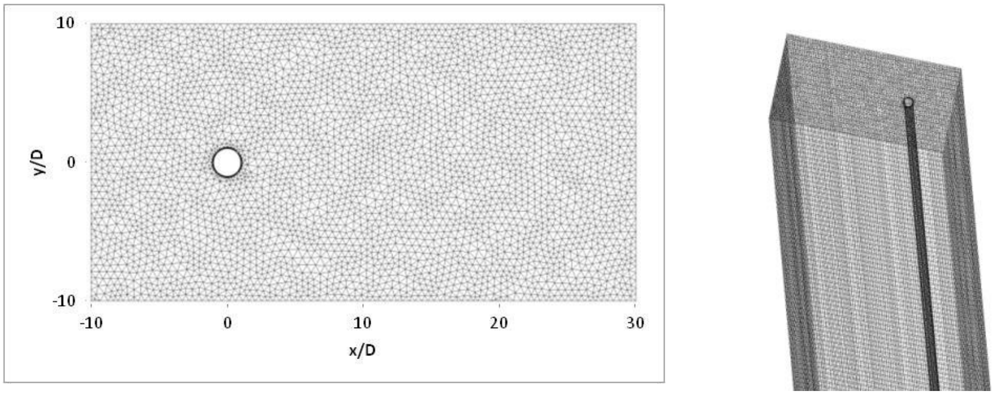

Fig. 2.10: Fluid mesh viewed from top (left) and the upper part of the 3D mesh (right), showing element length in the z-direction.

In figure 2.10 is shown the chosen mesh of the several meshes of the fluid domain developed and tested both with the riser as a stationary cylinder, thus, without the deformation tool activated, and as a vibrating riser. The purpose of the stationary cylinder riser simulations was to find the correct cylinder wall boundary layer in what respects to capture this boundary layer and the pressure field produced by the flow with enough accuracy. The accuracy criteria were both the value of *y+* and the value of the drag coefficient C_D.

The first prism layer thickness was reduced progressively until achieving a simulation with the required value of $y^+ < 1$ for the maximum simulated velocity, 1.8 m/s upon riser surface, a riser drag coefficient value near that of a L/D = 1 cylinder, C_D = 0.64, Blevins (1984) and also a good vortex shedding pattern. The final y^+ was lower than 1 and the C_D value obtained was 0.67 (in good accuracy with the 0.64 value of Blevins (1984)) when the boundary layer was defined with the following parameters: 10 layers of prisms with an exponential growth of 1.35 and a first layer thickness of 2e-5 m.

Once obtained the boundary layer requirements and, following the recommendations of Holmes et al. (2006), the size of the bulk mesh elements was that required to obtain about 2.5K nodes on planes Z = 0 and Z = 475, so simulation accuracy is good, and the computation requirements do not grow excessively. The final value was 2553 elements by plane, see figure 2.10, left.

Finally, the number of elements on the mesh z-direction had to be obtained, see figure 2.10 right. Following the procedure of Xiao et al. (2016) the z-length is divided into 200, 175 and 150 elements of equal length, to produce meshes 1, 2 and 3, respectively. With this number of elements vibration modes from 1st to 10th order should be accurately captured.

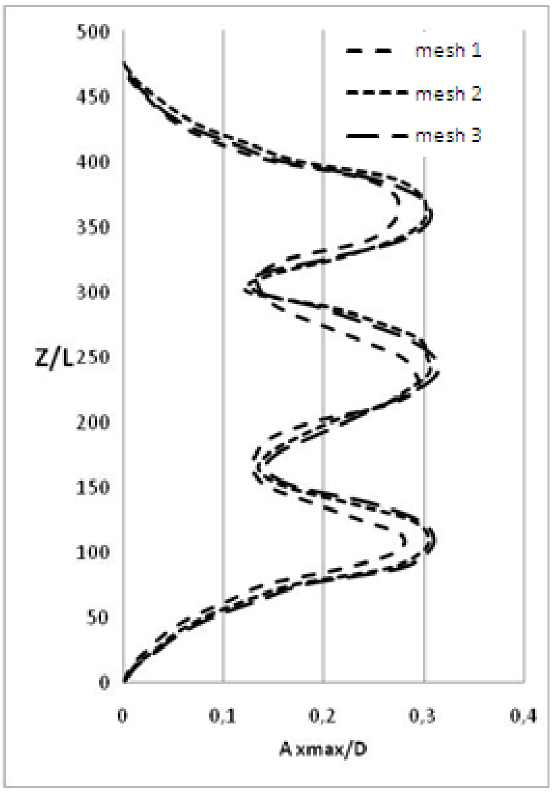

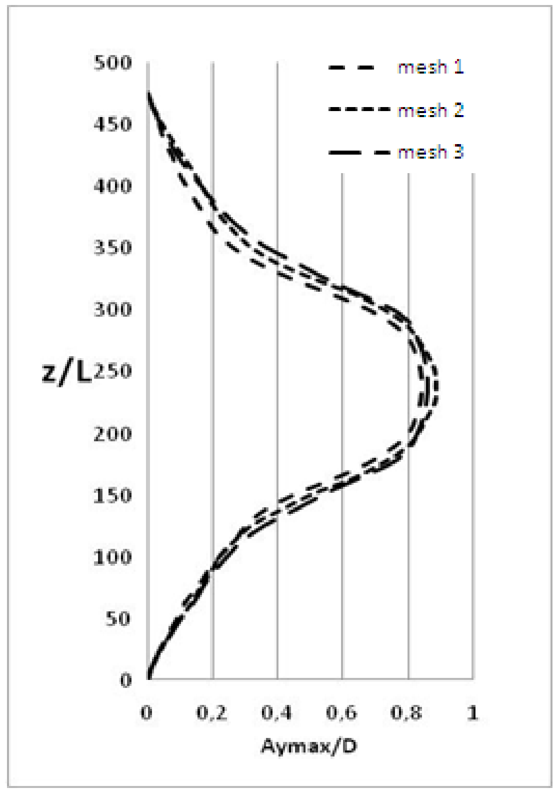

Fig. 2.11: Maximum riser oscillation in the IL (left) and CF (right) directions for the three analyzed meshes.

Hence, these three meshes were used for the final sensitiveness analysis. With this analysis was checked other possible sources of error, such as numerical diffusion or flow pressure mapping accuracy on the riser surface. The results can be observed in figure 2.11, where the oscillation in both the IL and CF directions were recorded over time until maximum amplitude was reached. Mesh 2 was chosen for the simulations as the increase of mesh nodes from mesh 2 to mesh 3 does not vary the results.

Time step analysis was carried out in the following way: knowing the anticipated frequency values, an initial estimation of the time step required to capture a wavelength with enough points was made. The first chosen time-step was 0.02 seconds, but simulations showed the need to reduce it. Values of 0.015 s and 0.0125 s were analyzed. The value of 0.015 seconds resulted acceptable for Reynolds 42K and 84K, and 0.0125 s was found to be acceptable for Reynolds 126K.

The simulations run with a high-resolution advection scheme, a second order backward Euler for the transient scheme, a high resolution for the turbulence mathematical model, and a convergence criterion of 1e-4.

Once the verification is done the validation was carried out. The geometry of the Xiao and Wang (2016) riser was taken and meshed following the values obtained in the verification process. The three timestep values were checked.

The Xiao and Wang (2016) riser was 9.63 m long and has a diameter of 20 mm. Its Young modulus is 1.025 e+11 N/m2. It is pre-tensioned with a force of 817 N and has a mass ratio of 2.23. These figures can be observed in Table 2.3.

Table 2.3. Data of the Xiao and Wang (2016) riser, taken for validation.

Properties	Values	SI units
Length	9.63	m
Diameter	20	mm
Young modulus	1.025×10^{11}	N/m^2
Tension	817	N
Mass ratio	2.23	--

This riser was simulated, in the Xiao and Wang (2016) article, at two velocities: 0.2 m/s and 0.42 m/s. For the validation, the higher was chosen.

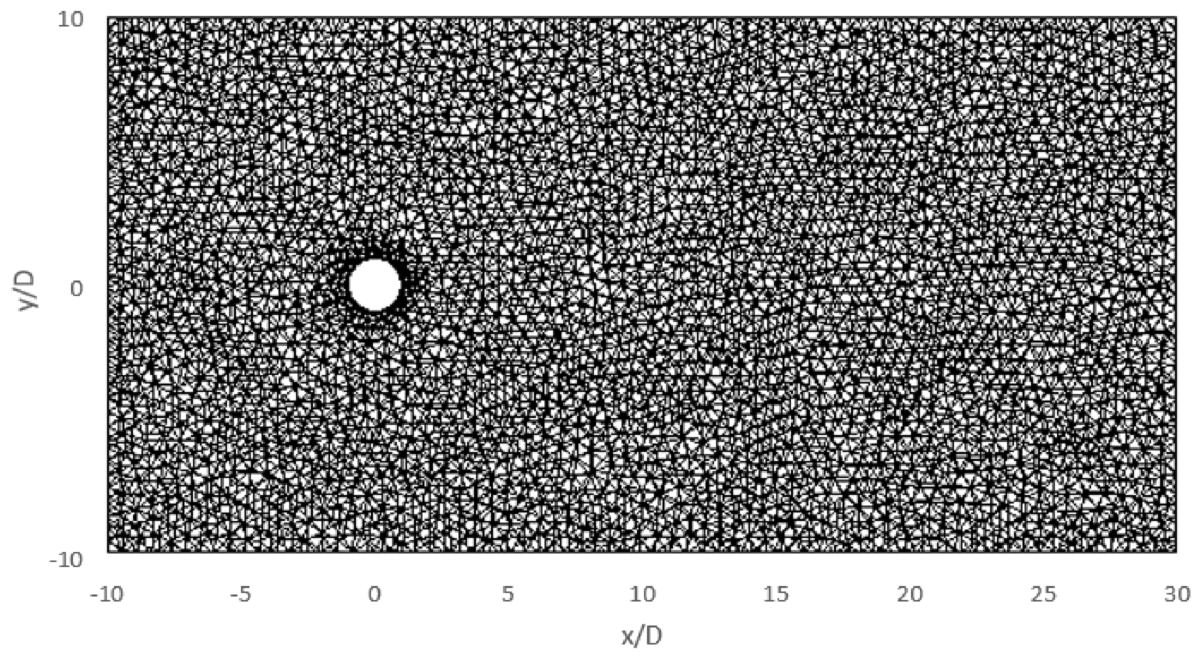

Figure 2.12. Mesh for validation purposes (top view).

Once the mesh was obtained, the case of velocity 0.42 m/s was simulated with the three timesteps used also for this work cases. These are: 0.0125 s, 0.015 s and 0.02 s.

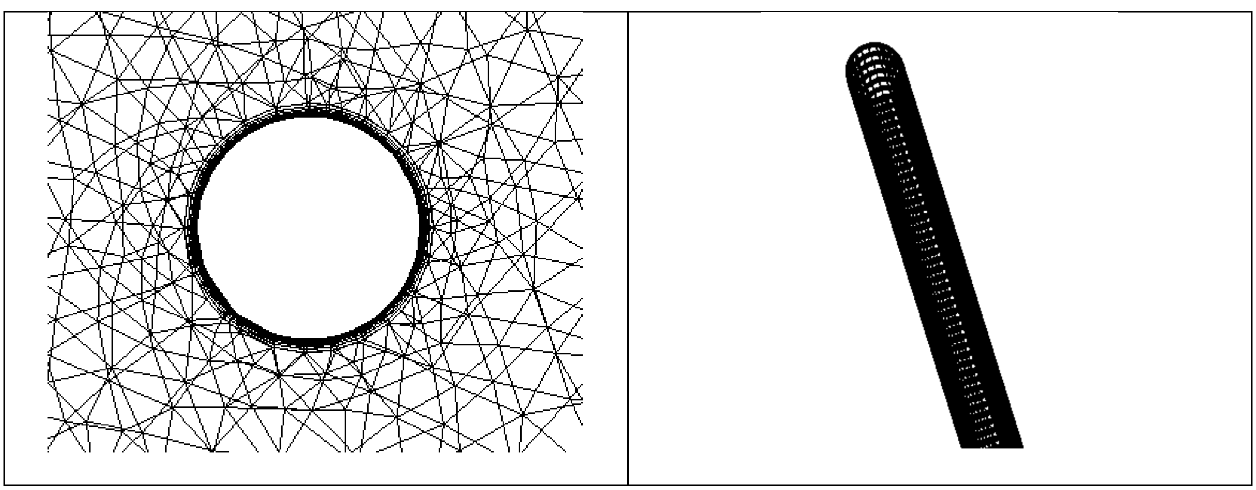

Figure 2.13. Mesh for validation purposes: boundary layer (left) and riser (right).

Once the case was chosen, the meshing process was done according to the parameters obtained in the verification process. These parameters are:

- A boundary layer composed of 10 layers of prisms with an exponential growth of 1.35 and the first layer thickness of 2e-5 m.
- An average of about 2.5K nodes at every vertical plane. This is, if the mesh is cut at any height value, the number of nodes in that planes is about 2.5K.
- The mesh vertical height, which is the same that the riser length was divided into 175 as expected oscillation modes were similar, from first to third in Xiao and Wang (2016) and from first to fifth in this work.

An image of the validation mesh can be observed in figures 2.12 and 2.13.

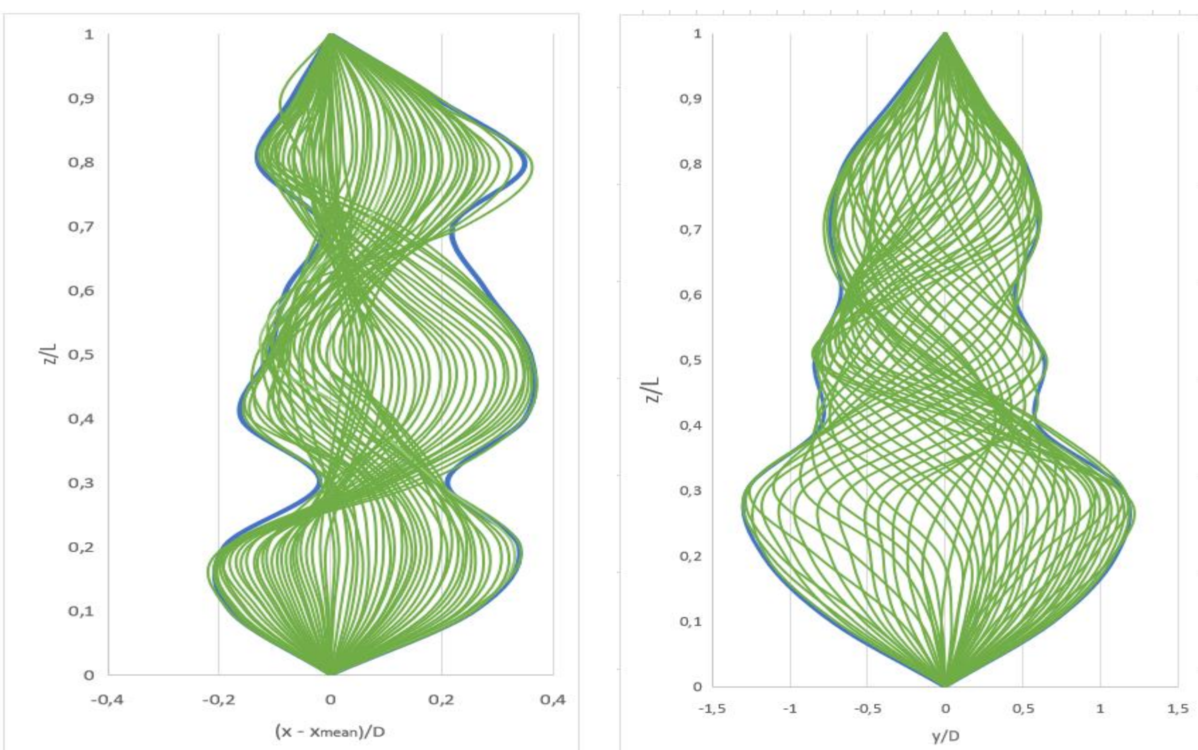

Figure 2.14. IL (left) and CF (right) envelopes from Xiao and Wang (2016) and in present work.

In figure 2.14 the IL and CF envelopes for the 0.015 s case (the finally chosen one) are observed. The blue line represents the Xiao and Wang (2016) results envelope meanwhile green lines are the oscillations for each timestep of the validation simulation.

It can be observed how the accuracy is good showing simulations and results taken for validation the same general shape with few smaller differences at some spanwise points.

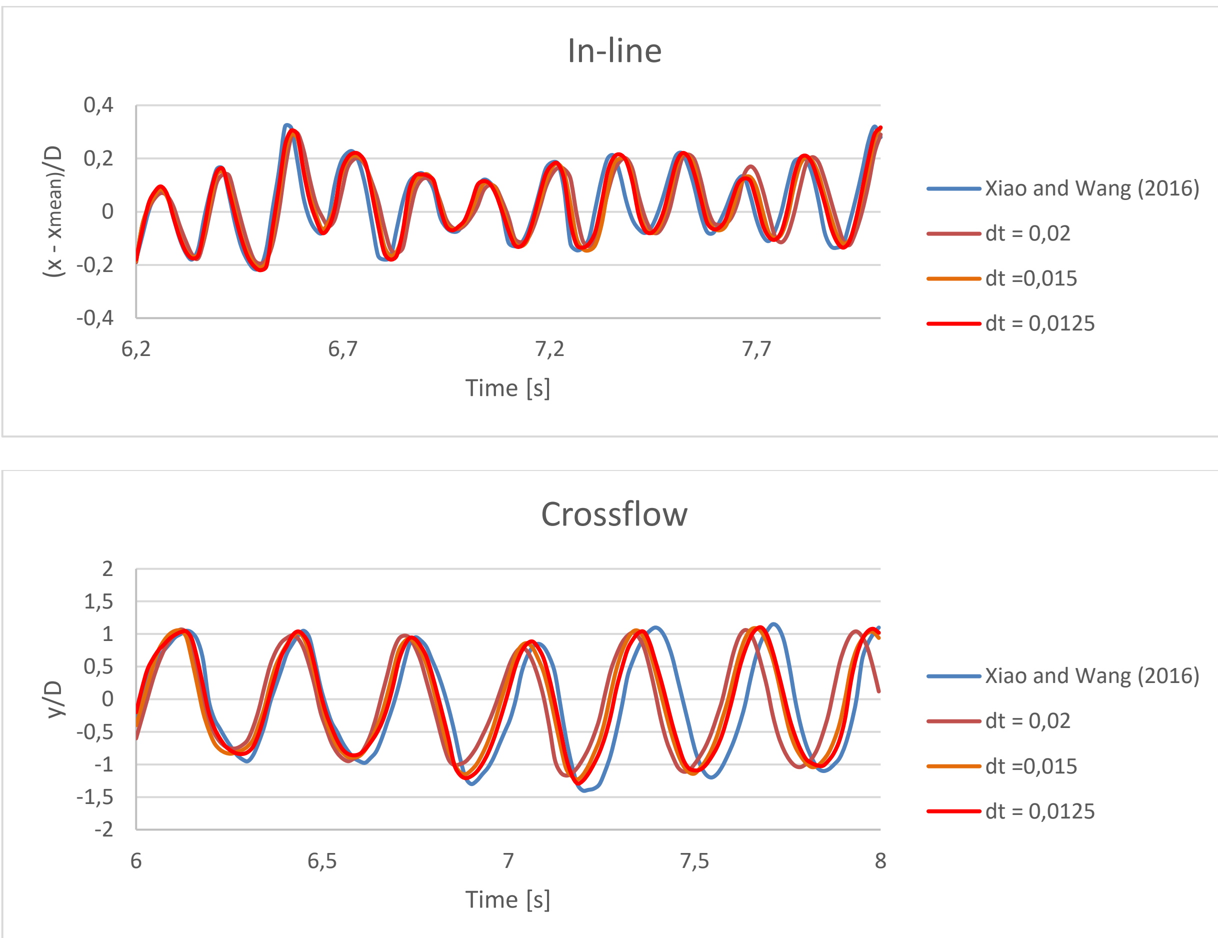

Figure 2.15. IL (above) and CF (below) time histories from Xiao and Wang (2016) and present work for the three different timesteps.

Figure 2.15 shows the time histories for the mesh but three different timesteps and z/L= 0.22 which is the spanwise point published by Xiao and Wang (2016), being no significative differences among the two smaller timesteps for both the IL and CF oscillations.

As conclusion, it can be said that the results of the simulations carried out following the theory recommendations for mesh development (to satisfy *y+* requirements and oscillation mode order) as well as timestep need (related to expected oscillation frequency estimation) achieve an accuracy enough to validate the simulation procedure.

Chapter 3

3. Reynolds number dependence.

3.1. Introduction

In this chapter the VIV phenomenon dependence of the Reynolds number is analyzed. To carry out this study, a range of Reynolds number 42K to 126K has been chosen. The aim is to find the vibration mode variation and the average and maximum oscillation amplitude variation with the Reynolds number.

3.2. Analysis data and variables

The analysis is carried out for three different velocity values: 0.6, 1.2 and 1.8 m/s (corresponding to Reynolds numbers 42K, 84K and 126K, respectively), and compared to published towing tank tests results of the riser of most similar characteristics found in the bibliography. These characteristics are equal geometry: length and diameter, but of different material as the towing tank riser complied an outer layer of a material of unknown Young's modulus value to make the riser known as Pipe 2, of 27 mm diameter to reach a diameter of 80 mm and, in this way, with the same towing tank velocity limit, obtain the indicated Reynolds numbers. They named this 80 mm riser as Pipe 3, Resvanis et al. (2012).

Besides, this size of riser (38 m) in this range of Reynolds number, with Reynolds number referred to riser diameter D, has not been studied by computational methods. Computational methods have no body size limitation as occurs with towing tanks when no scaling theory for that type of body is developed, what makes remarkably interesting to develop riser computational analysis.

Their towing tank results indicate vibration mode range 2 – 7 increasing in the same Reynolds number range. Beside the vibration mode number, the CF average and maximum amplitudes and the IL average amplitudes are analyzed variables. For these variables there are towing tank results for the whole Reynolds number range and for both the smooth and the rough towing tank same geometry risers.

The expressions of the dimensionless average and maximum amplitudes for IL movement, where transformation to dimensionless form is done with riser diameter are, respectively, Resvanis et al. (2012):

$$\overline{\sigma}_{A/D} = \frac{1}{N}\sum_{i=1}^{N}\sqrt{\sigma_{A/D}} = \frac{1}{N}\sum_{i=1}^{N}\sqrt{\frac{1}{M}\sum_{j=1}^{M}\left(x_j - \bar{x}_j\right)_i^2} \tag{3.1}$$

And:

$$\sigma_{A/D}^{max} = max_i(max_j(\sqrt{\left(x_j - \bar{x}_j\right)_i^2} \tag{3.2}$$

Where:

$\overline{\sigma}_{A/D}$ is the dimensionless averaged vibration amplitude along riser length and time.

x_j is the dimensionless oscillation amplitude of the point number *j* of the *M* points of equal distance among them at which the riser length is divided.

$\bar{x}_j$ is the dimensionless time-averaged vibration displacement of the riser at its point *j.*

N is the number of timesteps of equal time length of the FSI simulations.

Equal expressions, changing the x-coordinate for the y-coordinate, are used for the crossflow movement, CF.

The M number is 175, number of cells of the mesh in z-direction.

The N number is the number of time-steps that result of simulating 15 seconds of riser vibration at a time-step value of 0.015 s for the cases of the Reynolds number 42K and 84K and 0.0125 s for the case of the Reynolds number 126K. The simulation time length of 15 seconds was checked to be enough to obtain several stabilized oscillations after the transient initial riser oscillation.

3.3. Results of the Reynolds number dependence.

The results of this chapter will be divided into two sections: “Oscillation envelopes and vibration amplitude” which will be focused on analyzing the riser oscillation modes and amplitudes, comparing them with the available data of the tests carried out by Resvanis (2012) for the most similar riser found, and the “Oscillation time histories and vibration frequency” section, focused on riser oscillation frequency analysis, including the effects of the two components involved in the vibration frequency: the beam-frequency component and the string-frequency component.

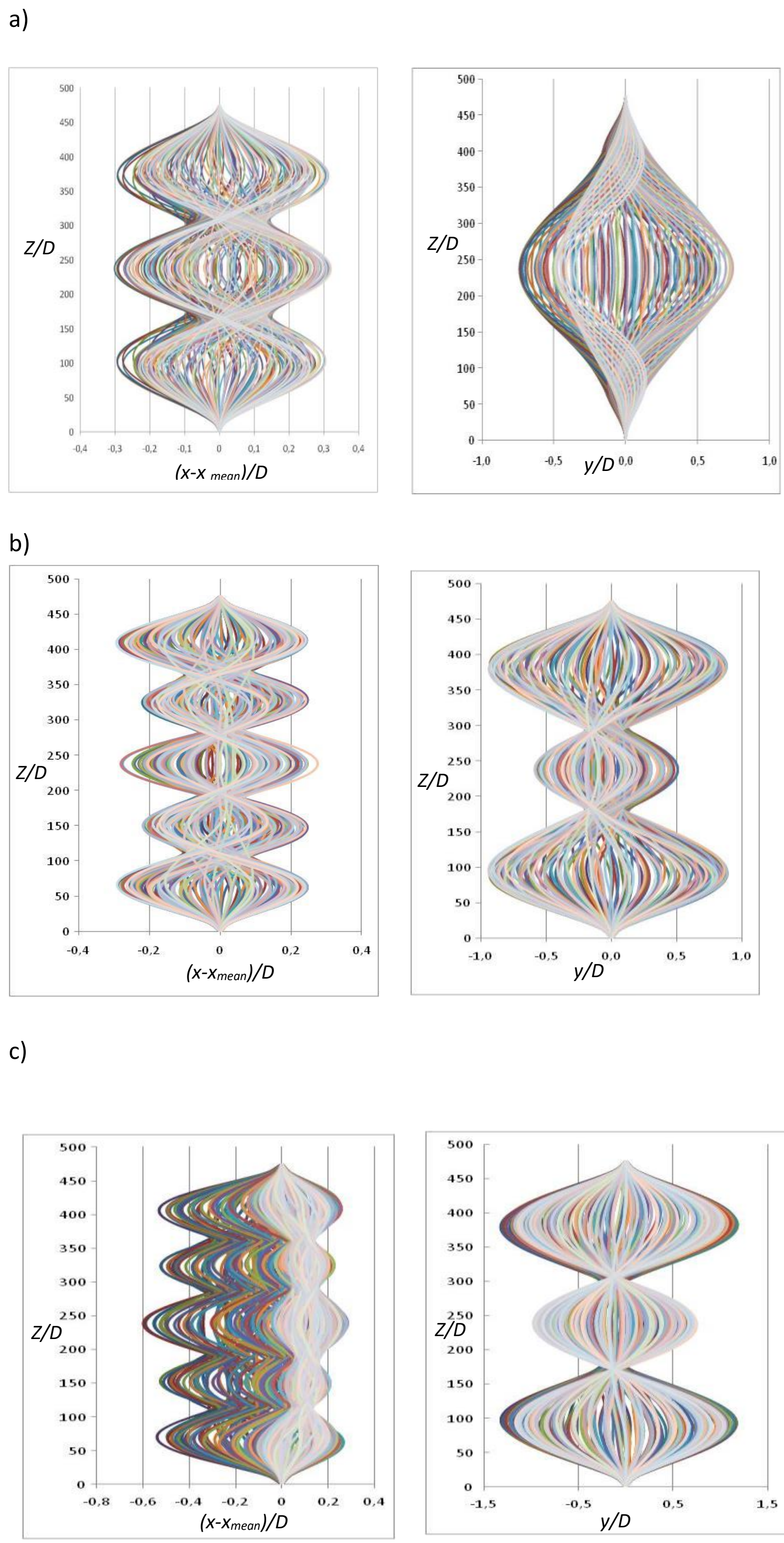

Fig. 3.1: Riser response IL envelope (left) and CF envelope (right) for the three Reynolds numbers: a) Re = 42K, b) Re = 84K and c) Re = 126K.

3.3.1. Oscillation envelopes and vibration amplitude.

In figure 3.1 the IL oscillation (left) and CF lateral oscillation (right) for the three analyzed cases are shown. Vibration mode might increase with Reynolds number, as occurs when the Reynolds number changes from 42K to 84K, or it might remain the same, as occurs when the Reynolds number changes from 84K to 126 K. In the first case the oscillation mode changes from a 3rd mode to a 5th mode for the IL oscillation, and from a 1st mode to a 3rd mode for the CF oscillation.

CF maximum amplitude increases with Reynolds number, being ~0.7D for Re = 42K, ~0.9D for Re = 84K and ~1.3D for Re = 126K. This behavior agrees with observations made by Bourghet et al. (2011a), Resvanis et al. (2012), Xiao and Wang (2016) and others. The CF maximum amplitude is about three times the IL maximum amplitude, in agreement with results reported by Bearman (2011).

IL maximum amplitudes do not increase evenly. In fact, from Re = 42K to Re = 84K they decrease slightly. This might be the result from the increase in riser tension level that would make a greater vortex shedding force component in the flow direction necessary to produce the same oscillation.

The values of the IL oscillation amplitude at the envelope nodes are different from zero. The envelope nodes are the envelope span points with narrow amplitudes. This emphasizes the modulation of the standing wave pattern, which would have node widths of zero, by superimposing traveling wave components.

All the CF and IL responses are quite symmetric, but the IL oscillation for Re = 126K shows clear non-symmetric behavior. This has been observed also by Xiao and Wang (2016) and seems to be the oscillation instability before change to a higher oscillation mode for Reynolds numbers immediately higher.

Calculating the IL and CF mean and maximum amplitudes $\overline{\sigma}_{A/D}$ and $\sigma_{A/D}^{max}$, (eq. 3.1 and 3.2) the obtained values are shown in table 3. 1.

Table 3-1 Numerical results of average and maximum IL and CF dimensionless oscillation amplitudes.

Reynolds n.	42K	84K	126K
$\sigma_{A/D}^{max}$ (CF)	0.712	0.939	1.322
$\overline{\sigma}_{A/D}$ (CF)	0.318	0.392	0.442
$\overline{\sigma}_{A/D}$ (IL)	0.122	0.089	0.107

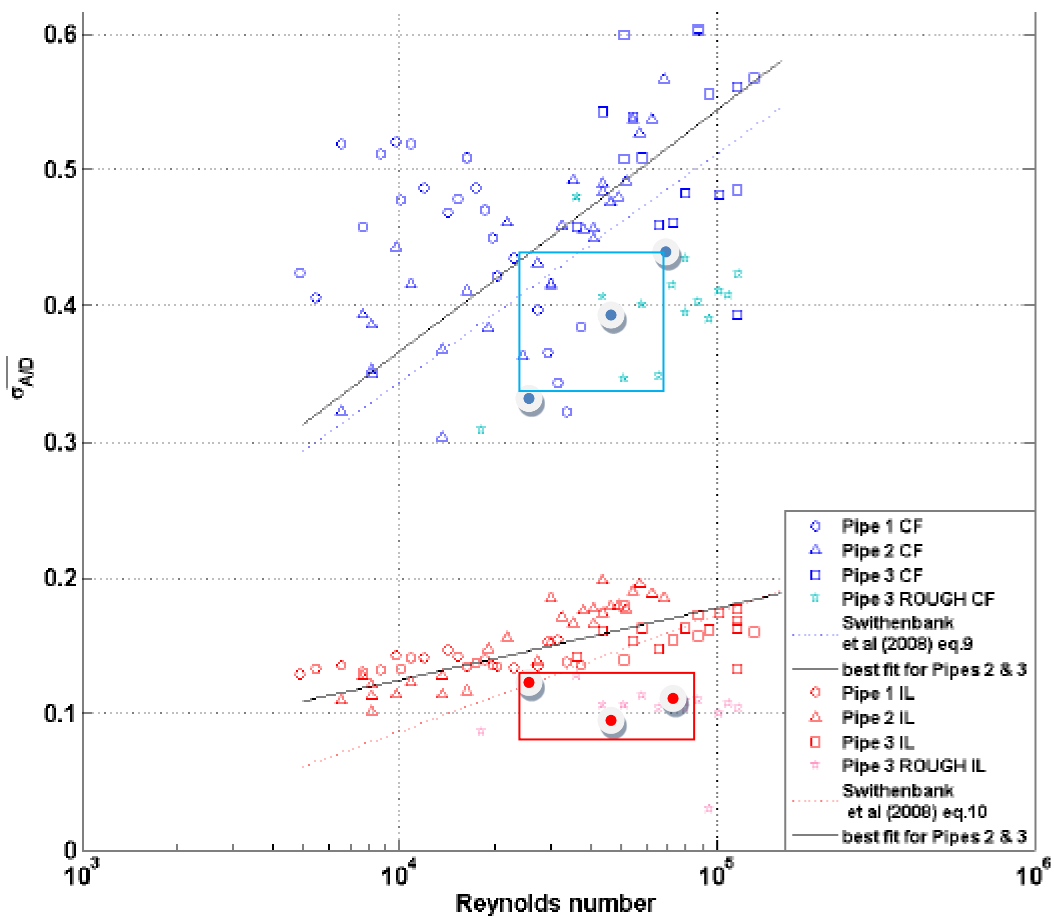

Figure 3.1 $\overline{\sigma}_{A/D}$ as function of Reynolds number for IL and CF oscillation.

In fig. 3.2, the results are compared to those of Resvanis et al. (2012), **indicated by clear blue stars for the CF average amplitude and red stars for the IL average one in figure 3.2**. They show good accuracy. It can be observed that experimental tests had some scattering and computational results fall within these scattering ranges.

The spatial mean amplitude $\overline{\sigma_{A/D}}$ for CF oscillation obtained in the simulations varies from 0.318 to 0.442 with increasing velocity from 0.6 m/s to 1.8 m/s meanwhile in the SHELL tests varied for the most similar riser, named Pipe 3 Rough, see Fig. 3.2, from 0.34 to 0.44.

The spatial maximum dimensionless amplitude $\sigma_{A/D}^{MAX}$ for CF oscillation increases from 0.712 to 1.322. Not values for rough Pipe 3 were indicated by Resvanis (2012).

The spatial mean dimensionless amplitude $\overline{\sigma_{A/D}}$ for IL oscillation varied from 0.122 to 0.107, also with increasing velocity meanwhile in SHELL tests varied from 0.09 to 0.12 for the rough Pipe 3. Both test results and simulation results show a slight scatter around an almost constant value of 0.11.

The simulations results show quite generally how the CF oscillation amplitudes are approximately three times the IL oscillation amplitudes, Bearman (2011).

Now, after observing a good accuracy between simulation results and those of Resvanis et al. (2012) tests, let´s follow their procedure to obtain an analytical correlation for those results. As above analyzed, the results show an almost constant amplitude for high Reynolds numbers in the IL vibration and a logarithmic dependence of the Reynolds number for the CF vibration. More precisely, the correlations given by Resvanis et al. (2012) are:

$$\text{CF direction:} \qquad \overline{\sigma_{A/D}} = 0.077\ln(Re) - 0.343$$

$$\text{IL direction:} \qquad \overline{\sigma_{A/D}} = 0.023\ln(Re) - 0.087 \tag{3.3}$$

These correlations have also the advantage of given amplitude larger than zero from already Reynolds a bit under 100 but the disadvantages of showing large results scatter and, precisely for the riser that covers the highest Reynolds number range (over 100K), named as Pipe 3 Rough, the uncertainty is the highest.

Obtaining a similar correlation to that of Resvanis et al (2012) but from the results of the computational simulations the resulting correlations are:

CF direction: $$\overline{\sigma_{A/D}} = 0.112\ln(Re) - 0.877 \tag{3.4}$$

While for the IL direction shows a practically constant value of 0.11, as occurs also in Resvanis et al. (2012). This might indicate that, in the IL direction there is an amplitude growth as Reynolds number increases but until some limit Reynolds number value where a maximum oscillation amplitude is reached. This maximum seems to be produced by the impossibility of further elongate the riser when it is very much tensioned, as will be observed more clearly in the orbital trajectories that will be analyzed in chapter 6. The non-appearance of this effect on the CF oscillation, where the riser is free to vibrate without supposing an increase in the tension seems to corroborate this explanation.

It must be noticed that Resvanis correlations are for the three risers together. Hence, there is a large scatter for some results, mainly for the Pipe 3 ones. The correlations developed from this thesis simulations correlate better the Pipe 3 results as they are developed for a riser much like that one. Therefore, to develop a correlation for different risers show a large uncertainty, each riser has his own correlation. To achieve a correlation common for several risers must need to change the correlation coefficients for functions of the riser characteristics.

Finally, after having analyzed the amplitude oscillation from both simulations and tests results, let´s investigate whether it can be obtained some evidence that might allow the prediction of the amplitudes without the need of tests or simulations.

The envelope amplitude is the riser deformation due to riser oscillation in both IL and CF directions, with these oscillations taking place from a constant IL deformed riser. This IL constant deformation is the deformation produced by the constant IL force, the drag force. So, as vibrations are Vortices-Induced Vibrations, the energy to produce the riser oscillation deformation must be related with the vortex energy and this one must be function of the flow turbulent energy and turbulence/vorticity generation produced by the riser.

Hence, to estimate the oscillation amplitude for a given oscillation frequency with equations, what corresponds is to make an energy balance. No work has been found aiming this task, out of that of Garrido, C. A. (2015), devoted to rigid non-deforming anti-heave plates and not to risers. The following calculus follows the equations 2.19 to 2.45 of chapter 2.

The energy balance can be formulated as that the energy of the fluid flow upstream, defined with eq. 2.28, is the same of the energy at the domain outlet plus the work done in its path. The external power, P_{ext} is the energy of the flow upstream the riser, and it is the sum of kinetic and turbulent kinetic energy at the domain inlet. No thermal energy appears being the phenomenon isothermal. Also, no potential energy appears due to not free surface effects existence. Furthermore, there is no net change in flow height.

The riser and fluid energy dissipations, ε_{Dr} and ε_{Df}, respectively, are the energy dissipated in moving and deforming a mass, the riser mass with added mass, along the average oscillation amplitude (as energy equals force multiplied by displacement) and the energy transferred in that process from flow kinetic energy to a higher level of turbulence.

The power values are obtained with such energy values divided by the oscillation time. The oscillation time are obtained from the oscillation frequency values, which gives the energy required per unit of time.

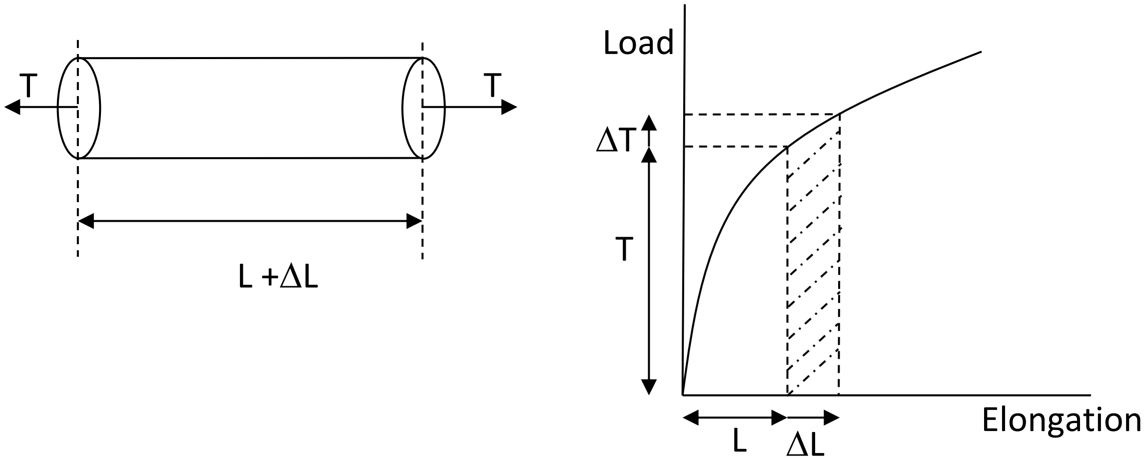

Figure 3.3 Elongation energy scheme.

Firstly, as vibrations take place form an averaged deformed riser, let´s see the energy required to achieve the riser averaged deformation. As it was commented in chapter 2, this deformation will suppose an increase of riser length produced by an axial load resulting from the riser axial component of the global drag force.

Hence, see figure 3.3, having a prismatic bar as the riser subjected to a load *T*, *T* moves through a distance ΔL and hence does work, Gere and Timoshenko (1988):

$$W = \Delta T \; \Delta L \qquad (3.5)$$

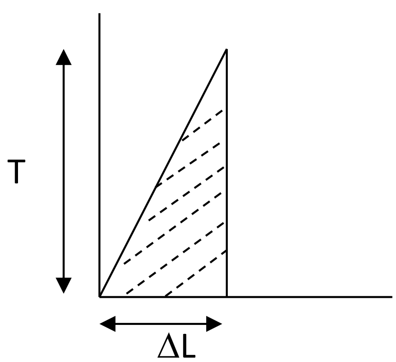

$$W = \frac{1}{2} \, T \, \Delta L \qquad (3.6)$$

$$\frac{\Delta L}{L} = \frac{T}{EA} \qquad (3.7)$$

$$U = W = \frac{T^2 L}{2EA} = \frac{EA \Delta L^2}{L} \qquad (3.8)$$

Figure 3.4 Elongation energy calculations.

This work W produces strain, which increases the internal energy U of the bar, see figure 3.4, when it has been regarded that that the change of elongation with tension is linear meanwhile elongations remain small. This internal energy or strain energy is defined as the energy absorbed by the bar during the loading process.

And the power transferred to the riser by the flow will be this internal energy divided by the time required to reach the averaged deformation, as it is observed in the Table 3.2.

The need of energy to elongate the riser grows with the squared power of the strain eq. 3.8, but the elongations do not grow linearly with the Reynolds number. In fact, doubling the Reynolds number from 42K to 84K produce an increase of a 52% of elongation, Table 3.2, and, when the Reynolds number is multiplied by three, from 42K to 126K, the elongation is only multiplied by two. As being the strains small, order minus five, they remain in the linear material behavior range, thus, the elongation is proportional to tension. Hence, the only possible cause of this smaller increment as Reynolds number grows is the decrease of the percentage of energy transferred from the flow to the riser as Reynolds grows.

The reduction of the percentage of flow energy transferred to the riser vibration as Reynolds number increases seems to be related to the decrease of the drag force coefficient and the small change of the lift force coefficient, as well as the oscillation amplitudes that grow logarithmically on all occasions but the IL amplitude for the Pipe 3, as it was already observed in Fig. 3.2.

Table 3.2: Power to obtain riser average in-line deformation.

Reynolds number	Tension	$\Delta L/L$	U	t	P
[-]	[N]	[-]	[J]	[s]	[W]
42K	5078	2.92e-5	2.82	2.4	1.17
84K	7722	4.44e-5	6.51	1.7	3.83
126K	10209	5.87e-5	11.39	1.2	9.49

Where the procedure to calculate the value of the tension of the second column of table 3.2 will be explained in chapter 4.

This power is consumed initially, until averaged deformation is reached. Then, oscillation takes places from this averaged deformation, consuming the following powers: power of the flow that faces the riser, table 3.3; power consumed in the IL oscillation, table 3.4; power consumed in the CF oscillation, table 3.5 and final power balance, table 3.6.

To be regarded that the averaged deformation time has been taken from simulations, but no other author has published.

Table 3.3: Power of the flow that faces the riser.

Reynolds number	Velocity	Mass flow	Power
[-]	[m/s]	[kg/s]	[W]
42K	0.6	1824.0	328.3
84K	1.2	3648.0	2626.6
126K	1.8	5472.0	8864.6

And:

Table 3.4: Power consumed by the riser in its IL oscillation.

Re n.	F_D	x/D	x	E	T	v	P
[-]	[N]	[-]	[m]	[J]	[s]	[m/s]	[W]
42K	820.8	0.122	0.0098	8.0	0.374	0.026	21.4
84K	3282.2	0.089	0.0071	23.4	0.171	0.042	136.8
126K	7387.2	0.107	0.0086	62.2	0.146	0.059	432.5

And:

Table 3.5: Power consumed by the riser in its CF oscillation.

Re n.	F_L	y/D	y	E	T	v	P
[-]	[N]	[-]	[m]	[J]	[s]	[m/s]	[W]
42K	755.1	0.318	0.0254	19.2	0.775	0.033	24.8
84K	3020.5	0.392	0.0314	94.7	0.347	0.090	272.8
126K	6796.2	0.442	0.0354	240.3	0.292	0.121	824.3

So, finally the energy balance is:

Table 3.6 Power balance: Percentage of flow power consumed in riser oscillation (last column).

Re n.	P fluid	P IL oscil.	P CF oscil.	P total cons.	% Power
[-]	[W]	[W]	[W]	[W]	[-]
42K	328.3	21.4	24.8	46.2	14.1
84K	2626.6	136.8	272.8	419.6	15.6
126K	8864.6	432.5	824.3	1256.8	14.2

To be noticed that, in all cases, the power consumed by the riser in the oscillation is about 15% of the power of the flow that the riser faces. Finally, future work might continue taking this value of power percentage as a data for other risers and use it to calculate riser oscillation average amplitude in an easy and cost saving way.

So now, having this value and the equation of the harmonic oscillation energy:

$$E_k = (0.15) * {}^{1}\!/_{2}\ m_w V_f^2 = {}^{1}\!/_{2}\,(m_r + m_{add}) A^2 \omega^2 \tag{3.9}$$

Where E_K is the kinetic energy of the flow facing the riser, m_w is the fluid mass facing the riser, V_f is the flow velocity upwind the riser, m_r and m_{add} are the riser mass and added mass (calculated with Khalak and Williamson coefficient), A is the oscillation amplitude and ω the oscillation angular velocity.

3.3.2. Oscillation time histories and vibration frequency.

The table 3.7 shows the structural frequency spectrum of the present work riser. The table shows, for the different oscillation mode number 1, 2, 3, etc., (shown at the first column) the frequency component taking the riser as a beam (second column) that is obtained from the equation 2.56 and the following three columns include the frequency component taking the riser as a string, obtaining the results with equation 2.55. It is in this last frequency component where the effect of the flow-induced tension appears.

When this tension is calculated and incorporated to the equation 2.55, calculated oscillation frequencies are much closer to those obtained in simulations. The procedure to obtain the riser tension for each Reynolds number will be explained in the next chapter.

As observed in table 3.7, the frequency of the riser as a beam $f_{n,beam}$ is about one order of magnitude lower than that of the riser as a tensioned string, $f_{n,string}$, having a negligible effect on the total frequency, as observed also by Xiao and Wang (2016).

Table 3.7: Structural frequency spectrum of the present work riser.

Riser vibration frequency spectrum							
n	f_{beam}	f_{string} (Re = 42K)	f_{string} (Re = 84K)	f_{string} (Re = 126K)	f_{total} (Re = 42K)	f_{total} (Re = 84K)	f_{total} (Re = 126K)
1	0.02	0.97	1.19	1.37	0.97	1.19	1.37
2	0.08	1.94	2.39	2.75	1.94	2.39	2.75
3	0.17	2.91	3.58	4.12	**2.91**	3.59	4.12
4	0.30	3.88	4.78	5.49	3.89	4.79	5.50
5	0.47	4.84	5.97	6.87	4.87	**5.99**	**6.88**
6	0.68	5.81	7.17	8.24	5.85	7.20	8.27
7	0.92	6.78	8.36	9.62	6.84	8.41	9.66

a)

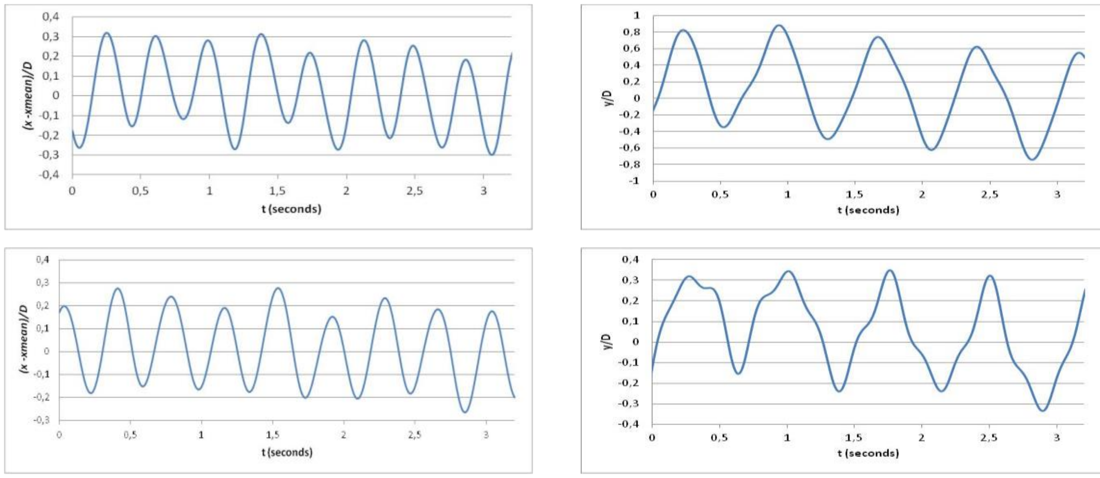

b)

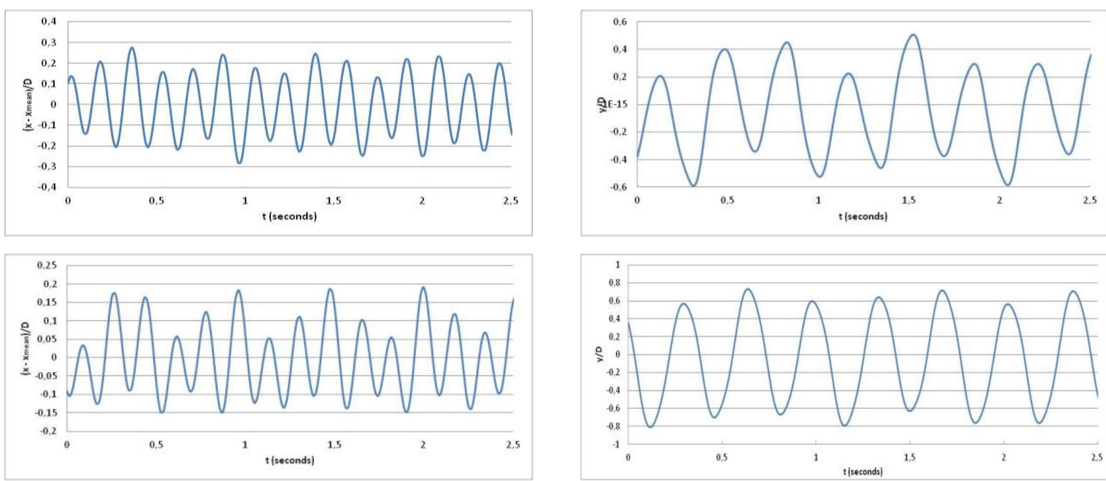

c)

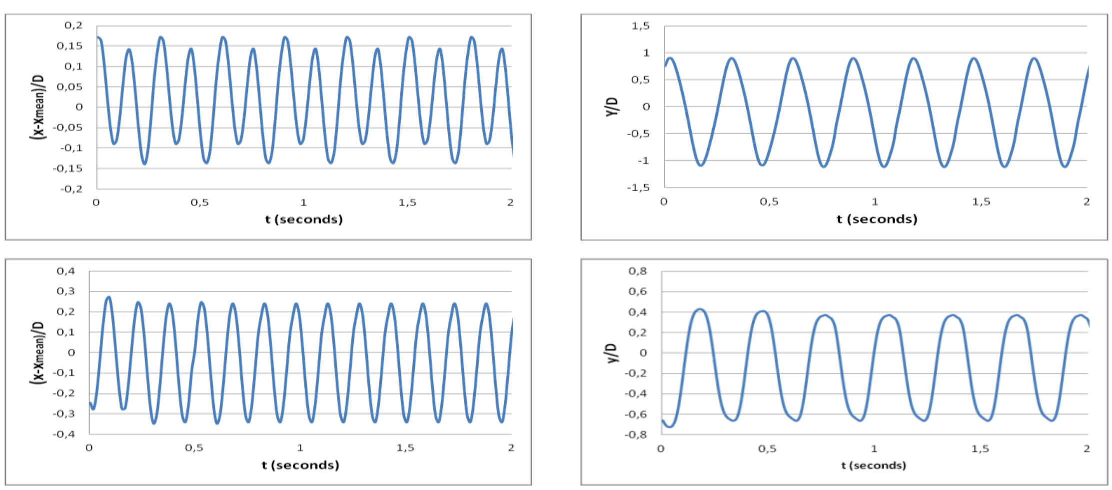

Fig. 3.5: Oscillation time histories at Z/D = 237.5 (upper) and Z/D = 125 (lower) showing IL oscillation (left) and CF oscillation (right) for the three Reynolds numbers: a) Re = 42K, b) Re = 84K and c) Re = 126K.

In figure 3.5 the oscillation time histories for both IL (left) and CF movements (right) are shown for two different riser spanwise points Z/D = 125 and Z/D =237.5 (riser middle length point). In all cases the time required by the riser to get loaded from the flow stream and reach its average deformation has been subtracted. It can be observed how, for all three cases, the IL response frequency is nearly twice that of the CF response frequency as table 3.8 shows. It can be also observed that the procedure accuracy is good, being the frequency value difference between the riser structural frequency spectrum**,** table 3.7 and results, table 3.8, small. The difference must be an effect of water damping, as it was also observed by Huang et al. (2011b). Also, just as observed by authors such as Resvanis et al. (2012) and Xiao and Wang (2016), the IL and CF oscillation frequencies increase with the Reynolds number.

The procedure supposes an improvement as, for example, a 3rd mode for Reynolds number 42K is 2.91 Hz in calculations meanwhile it is in the range 2.67 to 2.78 Hz in the simulations, a 5 – 9 % uncertainty. Xiao and Wang (2016) lowest uncertainty were of 50%, 3.12 Hz from their simulations and 4.73 Hz from tests.

In figure 3.5 it can also be observed that both IL and CF oscillations do not always show themselves as being formed by perfectly shaped sinusoidal shapes. This non-sinusoidal shape is more intense in the Z/D = 125 riser span than in the Z/D=237.5 one. The explanation of this effect, also observed in some oscillation time histories by Xiao and Wang (2016), is the presence of harmonics of slightly different frequencies and smaller amplitudes. Thus, the oscillation frequency value is really an oscillation narrow frequency range. Oscillation along time in different but near frequencies will produce such separation from perfectly shaped sinusoidal shapes. Also, sometimes, time stores show higher peaks after one or two lower ones, indicating those peaks the appearance of second or third harmonics with a non-neglectable energy associated to such harmonic frequency.

In the table 3.8 can be also observed how the IL frequency is nearly twice the CF frequency, this implies again that the riser behaves as a tensioned string, Lie and Kaasen (2006): for a non-tensioned beam, the IL/CF frequency ratio is lower than 2, due to the quadratic relationship between mode and frequency, equations 2.55 and 2.56, Weaver et al. (1974).

Table 3.8: Oscillation periods and frequency values for IL and CF oscillation as functions of Reynolds numbers.

Reynolds number	IL		CF	
	Z/D = 125	Z/D = 237.5	Z/D = 125	Z/D = 237.5
42K	0.360 s (2.78 Hz)	0.375 s (2.67 Hz)	0.735 s (1.36 Hz)	0.776 s (1.29 Hz)
84K	0.173 s (5.78 Hz)	0.171 s (5.85 Hz)	0.341 s (2.93 Hz)	0.348 s (2.88 Hz)
126K	0.146 s (6.84 Hz)	0.146 s (6.84 Hz)	0.292 s (3.42 Hz)	0.292 s (3.43 Hz)

When comparing tables 3.7 and 3.8 it can be observed how, in this last one, IL frequency of every case is about double than CF frequency and corresponds well with all the three IL frequency values for the three regarded Reynolds numbers and the respective oscillation order. But none of the CF frequency values fit. This is due to, as frequency values are linear with oscillation order, as equation 2.55 shows, and tension component of frequency is the main one, frequency of the riser as a string, as it is observed in table 3.7, to capture both frequencies, IL and CF, being one about double than the other, so modes should also be in the ratio 1:2. But IL and CF oscillation modes can appear in a ratio 1:3, as in the case of Reynolds number 42K, or 3:5, as in the other two cases. The explanation to this divergence seems to be that one of the oscillation orders is not an “exact” order. For example, the CF oscillation for the case of Reynolds number 42K is an “1.5” order, this is, the oscillation mode is shifting from a first order to a second one. This can be observed in the curves of some instant times in the CF oscillation, figure 3.1, where two nodes in the positive side of the graph appear.

Besides, the good accuracy of frequency values when taking the tension, with the flow induced effect included, demonstrates that the riser is a tensioned riser even if it is not pre-tensioned. And, as the riser is no pre-tensioned, the tension can be generated only as an effect of the fluid flow.

According to Lehn (2003) the natural frequency of the riser is dominated by tension if the relationship $T \geq 4\pi^2 n^2 EI/L^2$ is fulfilled, being *T* the tension, *n* the oscillation mode, *EI* the flexural rigidity (product of the material Young´s modulus and riser section inertia moment) and *L* the riser length. Notice that the values in this case cannot be used in their dimensionless form.

Doing the calculation of such expression for the Reynolds number 42K case, and consecutive vibration modes the results are:

$$T_{11} = 5080 \ \geq 4\pi^2 1^2 (3.46e^{+10}\ 2.01e^{-6})/38^2 \geq 1901.9 \tag{3.9}$$

$$T_{12} = 5080 \ \leq \ 4\pi^2 2^2 (3.46e^{+10}\ 2.01e^{-6})/38^2 \leq \ 7607.8$$

$$T_{13} = 5080 \ \leq \ 4\pi^2 3^2 (3.46e^{+10}\ 2.01e^{-6})/38^2 \leq 17117.5$$

Where the two *T* sub-indexes are the simulation case, related to the current velocity, and the oscillation mode, respectively. That is, T_{12} is the value of the riser dominated by tension criteria for current velocity 0.6 m/s or Reynolds number 42K (case 1) and 2nd vibration mode, and where tension values were obtained following the procedure that will be explained in chapter 4.

The tension *T* values, obtained from the riser elongation, eq. 2.64, are much larger than those usual values set as pre-tension in most of the investigated bibliography, which range is 100 to 1000 N, see table 3.9.

Table 3.9: Riser dimensionless elongation and tension as functions of Reynolds numbers.

Reynolds number	$\Delta L/L$	T[N]
42K	2.92e-5	5080
84K	4.44e-5	7722
126K	5.87e-5	10211

This will produce an important change in the riser oscillating frequency values, as can be checked by directly changing the tension value in equation 2.55. Also, it will produce a change in the vibration mode order for similar Reynolds number flows. This can be observed by comparing the oscillation mode orders obtained by Xiao and Wang (2016) who found a 2nd order oscillation for a Reynolds number of ~8K meanwhile Resvanis et al. (2012), also observed a 2nd order oscillation only when Reynolds number reached 42K and, as shown above, for the present work riser at the same Reynolds number 42K the oscillation number is a 1st order. As table 3.7 shows**,** it is the tension component the one that leads, in the same way than for other authors, Xiao and Wang (2016). Hence, the only explanation for this divergence is the not consideration of all the tension, as not considering the fluid-induced tension, in the frequency calculus. But, to do so, there should be a way to estimate this flow-induced tension. A way will be proposed in next chapter 4: The flow-induced tension.

3.4. Conclusions

The analyses of the simulated cases show the following conclusions:

- Oscillation order increases with Reynolds number. This increase is not continuous. There are Reynolds number ranges where the oscillation mode remains and, for some Reynolds number value, the oscillation becomes unstable as shifting to the next oscillation mode (case of CF oscillation for Reynolds 42K). The oscillation mode change takes place as, for different instants, the oscillation mode is the current one and for other instants is started to be observed the next oscillation mode.

- IL oscillation order is between 2 and 3 times the CF oscillation order.

- The length averaged oscillation amplitude grows with the Reynolds number for the CF movement and remains almost constant for the IL oscillation. The simulations achieve to predict, numerically, the oscillations amplitudes for the analyzed riser with good accuracy.

- The oscillation amplitudes as function of Reynolds number were represented by an analytical correlation, following the procedure carried out by Resvanis et al. (2012). Comparing both correlations can be observed that:

    - The form of the correlation is common for all the risers: a logarithmical curve.

  - Each riser has its own correlation. Using a common correlation´s coefficients for different risers produces large uncertainty.

- Currently there is no analytical method to estimate the oscillation amplitude without carrying out experiments or simulations. In the present work one method has been proposed. Starting with an energy balance is checked that the percentage of flow stream energy transferred to riser oscillation is about 15%, divided into a 5% for the IL oscillation and a 10% for the CF one, for the three different Reynolds numbers. With this value, the riser oscillation amplitude can be estimated.

- There is an influence of the flow velocity in the riser vibration frequency spectrum. To the already known pre-tension to which some risers are subjected, a flow-induced tension must be added. The development of this tension is the following one: the fluid flow produces a drag force upon the riser. The total riser length drag force is balanced at riser clamped ends with reaction forces. This force field creates a tension field within the riser body. For high enough Reynolds number values this tension is of larger value than the usual estimated pre-tension values.

- The riser is a tension-dominated riser as fulfills the equation of the tension-dominated riser: the IL oscillation frequency is about double of the CF oscillation frequency, Lehn (2003). This occurs although it is not subjected to a pre-tension. This effect asserts the former idea that flow induced a tension in the riser that must be regarded in the calculations.

- The inclusion of this tension in the analytical frequency calculation allows increasing frequency calculation accuracy. In the present case a 5 – 10% uncertainty has been achieved, when other works achieve a 50%, Xiao and Wang (2106).

- A explanation of how two common observations about VIV which seem cannot take place at the same time can, in fact, occur for the same case. These observations are:

  - IL oscillation frequency is about twice the CF oscillation frequency.

- Oscillation frequency is linear with oscillation mode, equation 2.63.

This would lead to IL oscillation order doubles CF oscillation order, but it has been observed in this work as in others that oscillation orders can be out of the relation 1:2. The explanations seems to be, in some cases, as the cases of Reynolds number 42K and 126K, that IL oscillations are starting to shift to the next oscillation mode.

Chapter 4

4. The flow-induced tension.

4.1. Introduction

In chapter two a new variable, the flow-induced tension, was introduced and the way in which appears was explained. In former chapter three this variable was used, and it was observed that its inclusion allowed obtaining a higher accuracy in oscillation frequency prediction when Reynolds number is high. In the present chapter it is shown how this variable is obtained.

A similar situation occurred years ago. Riser amplitude was predicted by means of a graphic: The Griffin plot. The Griffin plot was developed in the 70's and published in 1980, Griffin (1980). This plot represents the peak oscillation amplitude as a function of a parameter, the Skop-Griffin parameter, which is a combination of the riser mass and damping. It showed to have a nice accuracy for VIV results in air but huge scatter when dealing with cases in water. It took many years until Khalak and Williamson (1999) reduced that scatter by changing the riser mass by the riser total mass, being this last one the result of the riser mass itself plus the riser added mass and regarding this value as the potential result of the riser displacement in water.

A similar situation arises with riser oscillation frequency when Reynolds number exceeds the usual studied range 0 -10K, the predicted oscillation frequencies are far from the observed ones. But, as observed in chapter three, introducing the flow-induced tension, this difference can be severely reduced.

Then, to introduce this variable in the frequency calculation, it must be explained the way to obtain it. Two possibilities arise: calculation with simulations and analytical calculation. In section 4.3, these two possibilities, with different attempts for the analytical calculation, are explained.

The aim of the analytical calculation must also be explained. The idea is to **propose a simple method to estimate this flow-induced tension and riser natural vibration frequency spectrum without the need of carrying out FSI-simulations, which have a high cost in terms of time, focused on a pre-design step. The FSI-simulations are regarded, due to its time and cost requirements, for a detailed-engineering project.**

The feasibility of such model arises from the idea that risers and tension-legs are just a type of beam or string, subjected to a distributed force, in the same way that beam analysis, as a part of structure calculus, studies. The difference arises from the fact that the distributed force has a fluid dynamic origin. Several models have been analyzed to estimate a second relationship between the flow-induced tension and a riser deformation parameter (elongation, curvature, angle at its ends, etcetera), to achieve a determined system with two variables: tension or force, and deformed riser curve shape, and two equations. The analyzed ones are:

a) The equation of the beam with a constant load along its length.

b) The equation of the catenaries' (changing the constant weight per unit length for constant drag force per unit length in case of constant velocity flow).

c) The Jhingran simplification of the riser differential equation, Jhingran et al. (2008), Resvanis et al. (2012)

d) A model regarding a relationship between tension and riser angle at its extremes.

4.2. Theory Review

The tension field within a riser arises from the force effect produced by the flow upon the riser surface: drag and vortex shedding forces and varies with flow velocity. Tension is the response of the riser material to the state of forces at which these flow forces make it subjected. When a fixed body is under a field of forces, the body produces forces in its fixing points that balance the forces of such field. The effect of the acting and reacting forces within the body is to create a state of stress (per body area unit) and tension (per body section). Hence, as the external force field becomes stronger, i.e., the drag force produced by a flow stream when the stream velocity increases, the reacting forces grow to balance this higher drag force and the stresses within the body grow in the same way. Therefore, this tension induced by the flow stream is what has been named in this work as flow-induced tension.

The formulation for this flow-induced tension proposed in this work is the following one:

The force upon a riser section due to the fluid flow is:

$$dF = \frac{1}{2} C_{Dz} \rho \, dS \, V^2 \tag{4.1}$$

Where:

$$dS = D \, dL \tag{4.2}$$

dF is the force per riser unit length, in [N/m].

C_{Dz} is the drag coefficient in the cylinder sector at height z, dimensionless.

ρ is the fluid density, in [kg/m^3],

dS is the surface facing per riser unit length, in [m^2],

D is the riser diameter, in [m],

dL is the riser differential of length, in [m] and

V is the flow velocity, in [m/s]

Being the total drag force the integral of eq. 4.1 to the riser whole length, hence:

$$F_D = \int_0^L dF\ dL \tag{4.3}$$

Applying Newton's 3rd law, that asserts that: "**for every action, there is an equal and opposite reaction"** to the riser in the flow direction (x–direction) and in the axial direction (z-direction) of the riser before it deforms, it will be obtained the equations of static equilibrium:

$$F_{Dx} + R_{1x} + R_{2x} = 0$$
$$F_{Dz} + R_{1z} + R_{2z} = 0 \tag{4.4}$$

Where F_{Dx} and F_{DZ} are the components of the total drag force in "x" and "z" directions and R_1 and R_2 are the reactions in the two riser fixed extremes.

Upon the riser and supposing a uniform flow, regarding weight as neglectable, as risers are built to be almost neutral in buoyancy, this is, weight and displacement being similar, then, due to vertical symmetry the action of the flow drag force produces the equal and opposite reactions on riser extremes, hence R_1 and R_2 are equal but of different sign in the z-direction.

These forces and reactions are transmitted to every riser section, so the section will be in static balance, this is, the sum of the forces applying to the section equals zero, as there is no more section movement (a non-zero resultant force will produce, upon the section mass, an acceleration, Newton´s second law).

Once the riser has been deformed, and regarding the average deformation, that is, without considering the oscillations, both the forces and reactions of equation 4.4 can be now decomposed, for each riser axial section, in a tension in the perpendicular direction of the section and a section parallel to the section. The perpendicular component will produce an tensile stress and the parallel component a shear stress (section displacement respect to adjacent section) and a flexion (section rotation respect to adjacent section).

The only stress that supposes a net stress increase is the tensile stress that produce a riser elongation. This can be clearly observed as deformed riser is longer than the straight non-deformed riser.

As there is a known relationship between elongation and tension, equation 2.64, calculating the riser elongation allows obtaining the riser tension.

4.3. Flow-induced tension estimation models.

In this section both the procedures to estimate the flow-induced tension from simulations and from analytical models are developed. Firstly, the method with available simulations is analyzed.

Having developed the riser simulations, the first step to obtain the flow-induced tension is to calculate, from the average riser deformation, the riser elongation and obtaining the tension average value from equation 2.64.

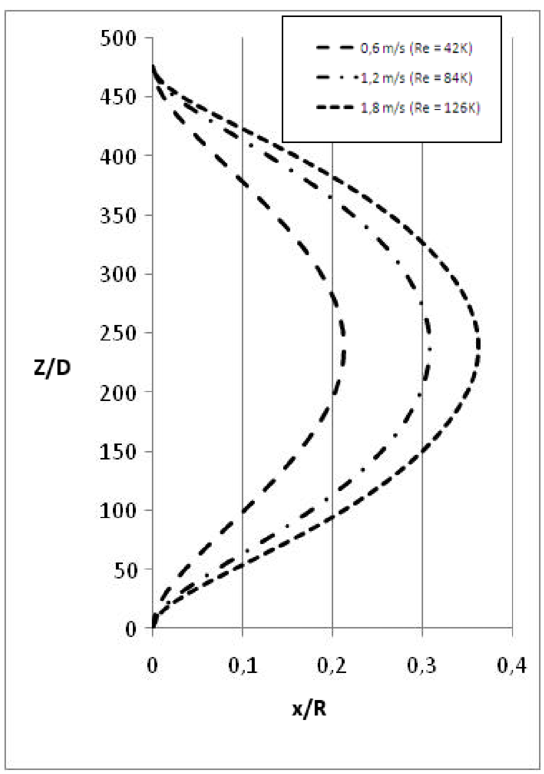

Fig. 4.1: Time-averaged dimensionless IL displacement for the three Reynolds numbers.

The riser average deformation is obtained by post-processing the simulation results, this is, obtaining for each time step the IL riser shape and calculate, for each riser spanwise section, the average of all the timesteps deformation. The difference between the riser oscillation and this rises average deformation is the vibration in the IL direction. The riser average deformation, for the riser analyzed in the present work and for the three Reynolds number considered, is represented in figure 4.1 which shows the IL radius-dimensionless average displacement from the original straight riser as function of the riser diameter-dimensionless length coordinate Z/D for the three regarded Reynolds numbers.

By applying equation 4.5, or its discrete version 4.6, on the IL average displacement curves of figure 4.1 the riser length elongations ΔL are obtained. Entering these elongations and riser characteristics into equation 2.64 the riser tensions are obtained. Both elongations and tensions were shown in Table 3.9, and with those tensions, the riser frequency spectrum were calculated with a higher accuracy than without considering this parameter as it was observed in former chapter 3.

$$L' = L + \Delta L = \int_0^L \sqrt{1 + y'^2}\, dx \tag{4.5}$$

As the direct integration of the eq. 4.5 integral is not possible for an unknown deviation curve, the following numerical discretization can be used:

$$L' = L + \Delta L = \sum_{i=1}^{n} \sqrt{{\Delta x_i}^2 + {\Delta y_i}^2} \tag{4.6}$$

Now, let´s survey the four analytical proposed methods:

- **MODEL OF RELATIONSHIP BETWEEN DRAG FORCE, FLOW INDUCED TENSION AND RISER ANGLE AT ITS EXTREMES.**

As net drag force value is F_D, that is, the drag force resultant in the whole riser length, a tension field within the riser will appear. This tension field will expand through the whole riser until its ends, clamped to seabed and windmill platform. At each of these two points a reaction force will appear, as net force must be zero for the riser remain at its place (principle of statics, part of mechanics that study bodies in mechanical equilibrium). These are equal among them (due to symmetry and uniform flow), each of them will be of value $F_D/2$, see fig. 4.2:

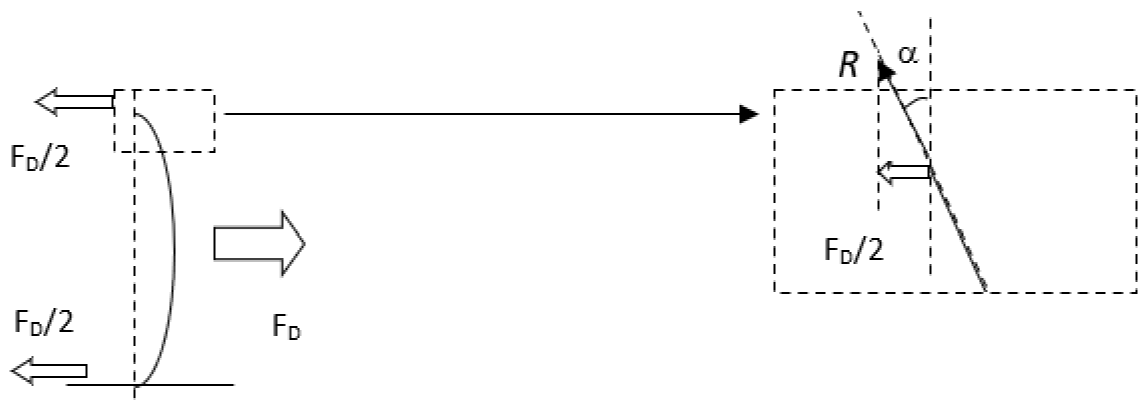

Fig. 4.2 Riser in-line average force equilibrium neglecting vibration (left) and force scheme at riser end (right).

In Fig. 4.2 right side can be observed the relationship between the reaction R, at riser extremes and total drag force F_D, resulting in:

$$R = \frac{F_D/2}{\sin \alpha} \tag{4.7}$$

Hence, a relationship between R and α is obtained. A second relationship between riser angle at the ends and tension or deformation is required.

This second relationship will be surveyed later, on this subsection.

Now, the resulting angles knowing force and tension from simulations are calculated and checked whether they are reasonable values:

- Using eq. with C_D = 1.5, U = 0.6 m/s, D = 0.08 m and ρ = 1000 kg/m^3 is obtained a drag force per length unit of: 21.6 N/m.
- For 38 m, this supposes: F_D =21.6 x 38 = 820.8 N.
- The tension will be, for an uniform flow: R =F/2/sin (α) = 820.8/2/ sin (α) = 410.4/ sin (α) = 5080.
- Hence, sin (α) = 0,0808, α = 4.63 deg (reasonable value).

This calculus results can be better observed in the Table 4.1:

Table 4.1 Riser angle at its ends. Estimation as function of flow velocity.

Velocity	F_D/L	F_D	T	α
[m/s]	[N/m]	[N]	[N]	[deg]
0.6	21.6	820.8	5080	4.63
1.2	86.4	3283.2	7722	12.27
1.8	194.4	7387.2	10211	21.21

With this approach, an estimation of riser tension from the riser angle at riser extremes could be estimated what, in principle, could be an easy way to determine it in experimental cases and in the upper rise extreme of real installations. Therefore, it could become a possible method to control tension experienced by real risers.

As a method proposed for first time, evidently, requires further investigation.

- **MODEL OF BEAM DEFORMATION WITH UNIFORM FLOW CONSTANT DRAG FORCE AS LOAD.**

For this model, the assumption of the riser as a beam briefly presented in chapter 2, figure 2.6, is retaken. The equation of the deformed beam with ball joints at its ends was given by equation 2.65 being its first and second derivatives obtained in equations 2.66 and 2.67, respectively. The equation 2.68 yields the deformed beam final length.

In this case it is analyzed the riser with clamped extremes, hence:

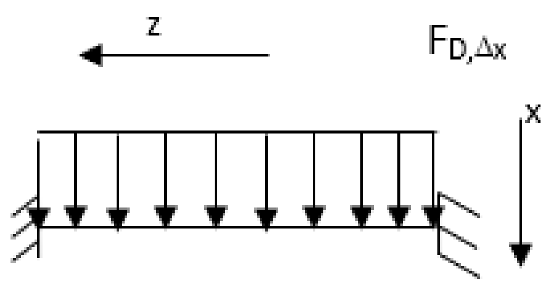

Fig. 4.3 Scheme of the riser as a beam with both ends fixed and subjected to an even drag force distribution.

When in every riser section a drag force $F_{D,\Delta x}$, following the equations 4.1, and taking in that equation a value for the drag coefficient C_D of 1.5, value found by several research groups and confirmed in the present work, as it will be shown in next chapter 5, is applied. The equation of the beam deformation, that is, the equation of the beam shape as subjected to an even force distribution is, Gere and Timoshenko (1988):

$$y = \frac{qL^2x^2}{24EI}\left(1 - \frac{x}{L}\right)^2 \qquad (4.8)$$

Where q, load per unit length, has been used instead of $F_{D,\Delta x}$ for the sake of equation clarity.

The maximum deviation appears entering $x = L/2$ in equation 4.8. For the first of the three cases, the one for Reynolds number 42K and being the flow velocity 0.6 m/s, q= 21.6 N/m, EI = 2.60e+7 Nm^2, the mass per meter length 0.937 kg/m, for $x = L/2$ = 19 m, it can be observed that the maximum deformation value will be 0.0045 m, when the value in the figure 4.1 is 0.21R, being R = 0.04 m, which yields a value of 0.0084 m. Calculating the total length with equation 4.6 yields an elongation $\Delta L/L$ of 0.75e-5 (in comparison to the simulation 2.92e-5). As, for a given value of the Young modulus E, tension is proportional to $\Delta L/L$, the calculated tension with this method results in: 1297 N (in comparison to the 5080 N of the simulation results).

The maximum deviation, elongation, and tension values for the three velocity cases are shown in table 4.2:

Table 4.2: Riser dimensionless maximum deviation, elongation, and tension as functions of flow velocity.

Velocity	Maximum deviation from model	Maximum deviation from simulation	Elongation from model	Elongation from simulation	Tension from model	Tension from simulation
[m/s]	[x/R]	[x/R]	[-]	[-]	[N]	[N]
0.6	0.11	0.21	0.74e-5	2.92e-5	1297	5080
1.2	0.45	0.305	2.28e-5	4.44e-5	3965	7722
1.8	1.01	0.36	1.15e-4	5.87e-5	20074	10211

It can be observed that, according to this model, deviation grows linearly with drag force q, equation 4.8, and this one grows with the squared power of the velocity, equation 4.3. But the maximum riser deviation, at riser length $L/2$, grows less than linearly, table 4.2, 3rd column and Figure 4.1, being the increment of riser maximum deviation lower as Reynolds increases. This deviation must be since risers do not behave as beams but as tensioned strings, as they did not either in the case of frequency analysis carried out in chapter 3.

This was also observed by Bourghet (2011a), but no explanation was given. The explanation is that, due to the riser deformed curve shape, an increase of elongation does not correspond with a linear increase of the riser maximum deviation. Hence, risers do not behave as beams, as they do not either in the case of frequency analysis, as was observed in former chapter 3.

- **MODEL OF UNIFORM DRAG FORCE ALONG RISER LENGTH AND THE CATENARY.**

Let´s consider the curve of a catenaries. ***The catenaries are the curves formed when, being a cable fixed at its two extremes, this is subjected only to its own weight, which is constant and uniform along its length. In this section it is regarded that, being the drag force per unit of riser length also constant and uniform along riser length, and being the relative weight of the riser neglectable, as it is immersed in water with riser relative density to water close to 1 (as it can be observed in the average deformation curves for uniform flows which are symmetric in vertical direction), the catenaries' weight can be changed by the riser drag force. Thus, the riser (a mooring system) is regarded as a catenaries' (another type of mooring system).***

The catenaries' equation is:

$$y = \frac{T_0}{\rho g}\left[cosh\left(\frac{\rho g}{2T_0}(2x - L)\right) - cosh\left(\frac{\rho g L}{2T_0}\right)\right] \qquad (4.9)$$

Where:

T_0 is the catenaries tension at catenaries mid-length, point of maximum deviation and slope zero.

L is the distance between the two fixed catenary endpoints.

In the present case the curve of the riser as a catenary will be:

(4.10)

$$y = \frac{T_0}{F_{Dx}}\left[cosh\left(\frac{F_{Dx}}{2T_0}(2x - L)\right) - cosh\left(\frac{F_{Dx}L}{2T_0}\right)\right]$$

Being F_{Dx} the drag force per unit of riser length, equation 4.1.

In the case of the catenaries model occurs as in the former models, there are two unknown variables, in this case the catenaries deviation "*y*" and the tension "T_0", and only one equation, the equation 4.10, but regarding the catenaries´ length, which equation is:

$$L' = \frac{2T_0}{F_{Dx}} senh\left(\frac{F_{Dx}L}{2T_0}\right) \qquad (4.11)$$

And knowing that in the usual catenaries´ case this length *L´* is known, as it is the length of the cable, and the length *L* is the distance between the points where the cable is installed, therefore also known, with the equation 4.11 the tension T_0 can be obtained and then with equation 4.10 the catenaries´ shape.

This is not the case of the riser, where only one length is known, the initial riser length before fluid-induced tension elongates it.

Consequently, the catenaries model for the riser must be calculated in other way. The proposed way is to define the catenaries elongation in the similar manner of that of a cylinder subjected to tensile stress, that is:

$$\varepsilon_c = \frac{\Delta L}{L} = \frac{L' - L}{L} \qquad (4.12)$$

Now, having the catenaries elongated length *L´* as function of tension T_0, equation 4.11 and the regarding elongation with equation 4.12 and, on the other hand, a tensile elongation, equation 2.64, the equation system is closed fixing the criterion that the elongations calculated by the two methods must be equal, thus $\varepsilon_T = \varepsilon_c$. Hence, the following predictive-corrective scheme is proposed:

a) An estimative value of T_0 is chosen,

b) Entering T_0 in equation (catenary length) it is found ΔL_c and ε_c

c) Entering T_0 in equation (tensile strength) it is found ΔL_T and ε_T

d) Entering ΔL_c in the equation of (tensile strength) it is found T_1

e) When $|T_i - T_{i-1}| < error$, with $error$ the required accuracy, the solution has been found. To be noticed that this enough small error in tension corresponds with an enough small error in elongation ΔL and strain ε.

The results for the chosen riser are shown in the table 4.3:

Table 4.3: Riser dimensionless strain, elongation, and tension as functions of flow velocity.

Velocity	Strain, ε	Elongation, ΔL	Tension, T
[m/s]	[-]	[-]	[N]
0.6	9.72e-5	3.69e-3	16997
1.2	2,45e-4	9.30e-3	42830
1.8	4.20e-4	1.60e-2	73545

It can be observed how the catenaries model overestimates the tension for all the velocity cases. The equation of the catenaries show that the catenaries have smaller curvature radius as its coefficient T_0/F_D is larger. So, for an almost straight catenaries as it is the case of the riser, the tension T_0 will tend to infinite. Hence, catenaries model is not a valid model as riser is not installed in the way that catenaries are.

- **MODEL OF RELATIONSHIP BETWEEN DRAG FORCE AND RISER CURVATURE.**

The last regarded formulation is that proposed by Jhingran et al. (2008) and kept by Resvanis et al. (2012) to be used from towing tank experimental results, although without published results. In this formulation, starting from the equation 2.72a in the IL direction and taking the temporal mean, ($\overline{\quad}^{t}$) to make all zero-mean terms to vanish and regarding a tension dominated riser, so EI is neglected, simplified such equation to:

$$-T(z)\overline{\frac{\partial^2 y^t}{\partial x^2}} = \overline{F(z)^t} \tag{4.13}$$

The term $\overline{\frac{\partial^2 y^t}{\partial x^2}}$ is the riser curvature and the term $\overline{F(z)^t}$ is the drag force per unit length, that is:

$$F(z) = \frac{1}{2}C_D(z)\rho D U(z)^2 \tag{4.14}$$

Then, as Jhingran investigation in towing tank has fixed elements to measure the tension by means of strain gauges measuring pipe curvature, so having riser tension and curvature measured the local drag coefficient as:

$$C_D(z) = \frac{2T(z)\overline{\frac{\partial^2 y^t}{\partial x^2}}}{\rho D U(z)^2} \tag{4.15}$$

To be noticed that this equation already implies a connection between flow force, represented by the drag coefficient and flow velocity *U(z)* and the riser tension *T(z)*.

Hence, former Jhingran and Resvanis equation can be presented as:

$$T(z) = \frac{\rho D U^2(z) C_D(z)}{2\overline{\frac{\delta^2 y}{\delta x^2}}} = \frac{F_D}{2curvature} \tag{4.16}$$

According to this equation, riser tension will be a function of drag force and riser curvature, both being directly calculated from the simulations or from towing tank tests.

Again, for a predictive model, there is the need of obtaining a riser deformed curve to extract from it the curvature (the second derivative of the riser deformed curve).

The possibility for this work is to analyze the model with the results of the simulations, figure 4.1.

Doing so, and integrating the curvature for the whole riser length, it is obtained:

Table 4.4: Riser curvature, drag force and tension as functions of flow velocity.

Velocity	Curvature	Drag force	Tension
[m/s]	[1/m]	[N/m]	[N]
0.6	0.00032	21.6	33 750
1.2	0.00065	86.4	66 460
1.8	0.00076	194.4	127 890

One interesting consideration is that, if for the riser curvature is taken that constant value of an arc of circumference, see fig.4.4, where this arc is the deformed riser and the secant line that limits such arc is the riser at rest, and for the angle between the arc and the line, this is, the angle of the deformed riser at its extremes, are taken the values of the first model, the model of the angles and riser ends, the curvature obtained is such that introducing it in the present model the obtained tension is the correct one.

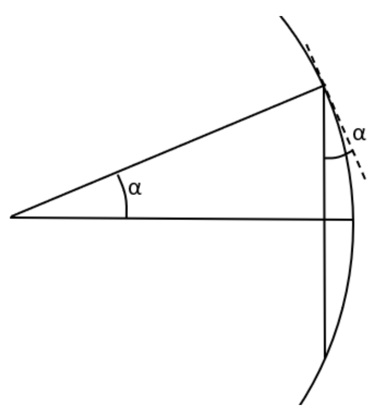

Fig. 4.4 Scheme of the riser as an arc of circumference.

Hence, the following relationship is fulfilled:

$$curvature\ \ T = R\sin{(\alpha)} \tag{4.17}$$

And regarding equation 4.7, the Jhingran model is also satisfied. Hence, the discrepancy between the tensions calculated with this method, Table 4.4, and the obtained with the tensile stress method used in this work, eq. 2.64 might arise from the way of obtaining the curvature from the strain gauges used in Jinghan towing tank tests. Work in towing tank would be required to clarify it.

So, with results of the first model and the geometric relationship of figure 4.4 a prediction-correction model can be proposed. This model is:

- Supposing and angle α at risers ends.
- With this angle, both initial riser length *L*, and elongated riser length *L´* can be calculated, where initial length is the length of the secant line in figure 4.4 and elongated length is the length of the arc of circumference in that figure.
- With equation 4.17 the average tension *T* of the riser can be calculated.
- This tension is compared to that given by equation 2.64.
- The initial regarded angle is changed until tension obtained with both euations 2.64 and 4.17 differ less than the required uncertainty.

4.4. Conclusions

The conclusions of this chapter are:

- The nature of the flow-induced tension variable and its influence on riser behavior, parameter that allows to obtain more accurate results, has been reviewed.

- The procedure to obtain the flow-induced tension from the simulation results has been explained. The procedure assumes that riser tension is like that produced by a pure tensile stress.

  This assumption corresponds well with the less than linear increase of riser average deformation as Reynolds number increases. This increase was formerly observed but not explained.

- Some analytical methods to predict the flow-induced tension without carrying out simulations, focused on a pre-design step, have been proposed and analyzed. The models are:

  a) a model based on riser angle at its extremes,

  b) the beam under a constant load distribution (as like a constant drag force produced by a uniform velocity),

  c) that of the equation of the catenaries' and

  d) the tension linked to the curvature (proposed by Jhingran et al. (2008) in a theoretical way).

- The model based on the riser angles at its fixed ends has an equation that related total drag force with angles at riser ends and two unknown variables: the angles, and the riser tension. Hence, a second relationship is required to make the system defined. A proposal is developed from the curvature model. This proposal is also regarded as a possible method to check tension in real facilities as angle on riser top fixed end might be an easy variable to measure.

- The model of the riser as a beam under a constant load distribution, where this constant load is the constant drag force that results of a uniform velocity flow. The model shows a quadratic riser maximum deviation. This quadratic behavior is a result of the quadratic growth of the drag force when velocity grows linearly and not correspond with the observed simulation results, which grow with a less than linear increment of deviation where velocity increases.

  It is a closed model as the only required variable is the force per unit length and that can be obtained from the drag force equation.

  This is the only closed model (same number the equations and unknown variables), but this characteristic is due to that the required relation is the riser flexural rigidity, that is data knowing riser material and section. But flexural rigidity implies riser behaving as a beam and the large uncertainty of this model asserts that the riser behaves like a tensioned string and not like a beam.

- The model of the riser or tension leg (a mooring system) as an extremely straight catenaries (also a mooring system and susceptible of experience VIV) clearly overestimates the tension. The catenaries model is a one equation model with two unknown variables: catenaries tension and deformation. In usual catenaries a second equation is obtained by calculating the catenaries length. This length is data in the catenaries case as these are installed with its extremes fixed in two points which distance is significantly shorter that the catenaries length. If these lengths are similar the catenaries equation yields extremely large tension values. For the riser case the two lengths are those of the riser at rest and the riser after the deformation produced by the flow. As these lengths are extremely similar the catenaries model overestimates the tension.

- The model based on riser curvature and proposed by Jingham, Resvanis et al. (2012) has been analyzed for the results of the simulations. The model is also undefined as consists of one equation with two unknowns: riser tension and curvature.

The analysis shows that, being the riser deviation small, also the curvature is so. Hence, large uncertainty appears in the curvature calculation which tends to be underestimated and, consequently, the tension is overestimated.

A relationship has been found that related this model with the first one. This relationship asserts that, taking the average curvature as that obtained with three points, the riser two extremes and the riser middle point, for what only maximum deviation in this last point is required, the model correctly captures the tension. Hence only the maximum deviation is required. This deviation can be derived from the first model. A predictor-corrector model is proposed and proved accurate for the present riser.

Hence, summarizing, the main conclusions of this chapter results are that:

- Currently, simulations or towing tank tests remain necessary to analyze riser behavior.
- Assumption of riser deformed mostly with a tensile stress corresponds well with the rate of increase of the riser deformation as Reynolds number increases.
- Unknown variables are more than available equations (excepting in the beam model).
- A first version of the predictor-corrector model is proposed.

Chapter 5

5. Drag and lift forces.

5.1. Introduction

In former chapter 4 it has been regarded that the drag force distribution is constant along the riser length for uniform flows, result of the drag force definition, eq. 2.58, this is, if the flow is uniform, all the variables that define drag force are equal for any riser spanwise point, hence, drag force distribution is also uniform. Nevertheless, it has widely observed, Bourghet et al. (2011a), Resvanis et al. (2012) that the riser drag coefficient is not constant with riser longitudinal position and, also, that it is higher than in the case of stationary cylinders.

It is the purpose of this chapter to report the results obtained in the simulations for this aspect.

5.2. Procedure

The riser was divided into one thousand sections of 1.5 inches (38 mm) so covering the whole riser length and force was measured upon the sections that contain the span values: 0 m, 1 m, 2 m, … 38 m.

With the ANSYS CFX post-processing tool, the IL and CF direction forces were measured along the simulation time, equations 2.81 to 2.83 and, later, in Excel data sheets, averaged in time and length.

5.3. Results

In this section the results for the riser drag and lift force length-averaged coefficients, C_D and C_L will be shown for shown for the three analyzed cases.

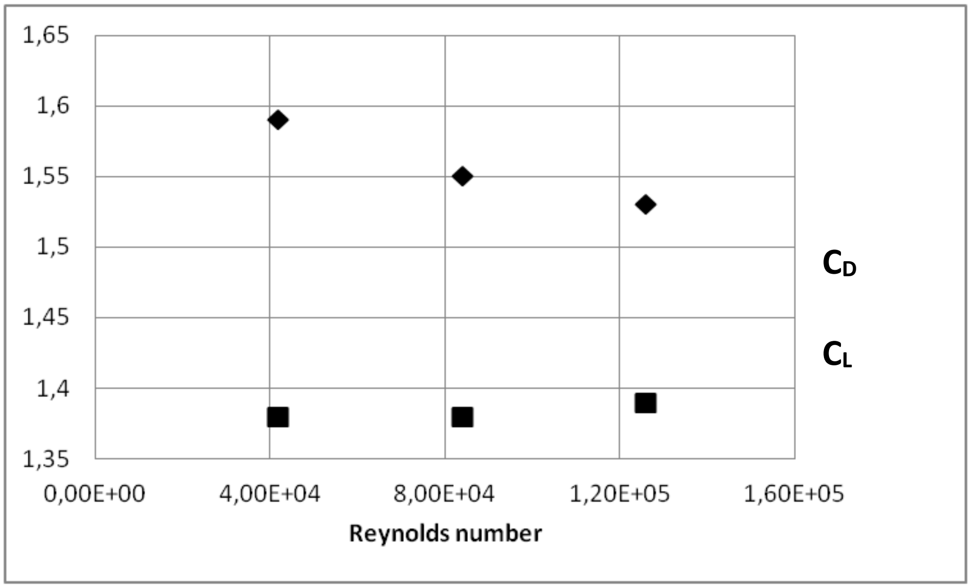

Fig. 5.1 Drag and lift force riser length-averaged coefficients as functions of Reynolds numbers.

Figure 5.1 shows how the drag force coefficient C_D shows a decreasing behavior when the Reynolds number increases, but in all cases is much larger than that of a fixed cylinder that is 0.64 for a finite length cylinder and 1.0 for an infinite long cylinder, Blevins (1984). This difference was also observed by Resvanis et al. (2012). On the other hand, the lift force coefficient C_L remains quite stable when the Reynolds number increases, as it is slightly higher for the higher Reynolds number, Re = 126K. This behavior corresponds well with the observations of Bourghet et al. (2011a).

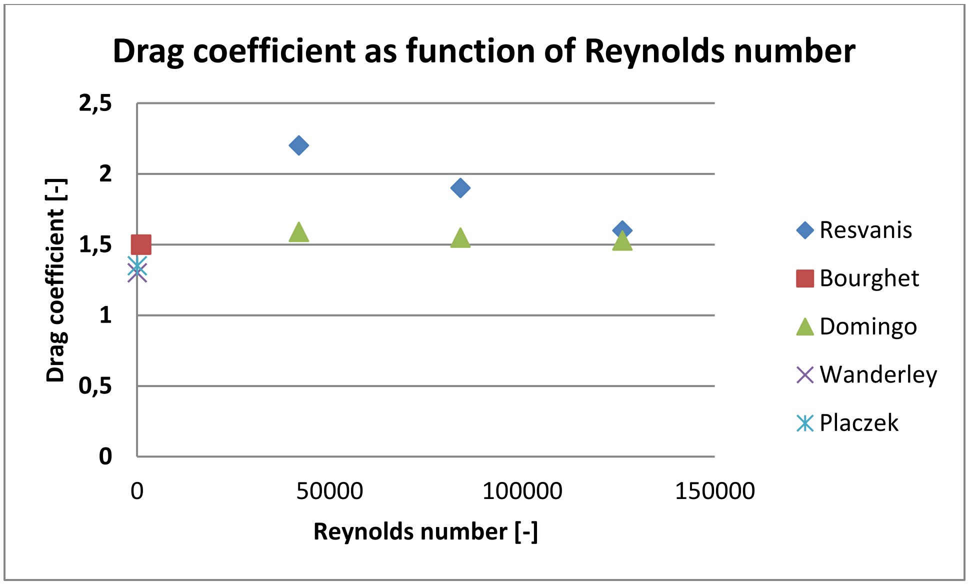

Fig. 5.2 Drag coefficient as function of Reynolds number (risers: Resvanis et al. (2011a) and Bourghet et al. (2012); Elastically mounted rigid cylinder: Wanderley et al. (2008), Placzek et al. (2009).

In figure 5.2 the results for the drag coefficient obtained by other researchers are shown. It must be observed that, excepting Resvanis et al. (2012), all other works were carried out for lower Reynolds numbers, <10K.

Both Resvanis and present work show a drag force coefficient value decreasing with Reynolds number although more evident in Resvanis results, from a value of 2.2 for Reynolds number 42K to a value of 1.6 for Reynolds number 126K. The difference must arise from the characteristics of the materials of both risers as riser geometry characteristics and flow parameters were the same. Less rigid riser, built with a material of lower Young´s modulus *E*, must allow larger elongation and contraction, according to oscillation phase, and higher relative velocity between riser and flow.

Because, as commented before, some research works have found that drag coefficient for oscillating risers is larger than that of rigid cylinder and, observing the equation of the drag force, 2.66, the only reason for this increase, being water density and riser diameter constant, is the increase of the velocity or, to be more accurate, the increase of the relative velocity between the riser and flow, being this relative velocity the result of the vectorial sum of flow velocity and riser oscillation velocity. It is this relative velocity the velocity that produces the drag force.

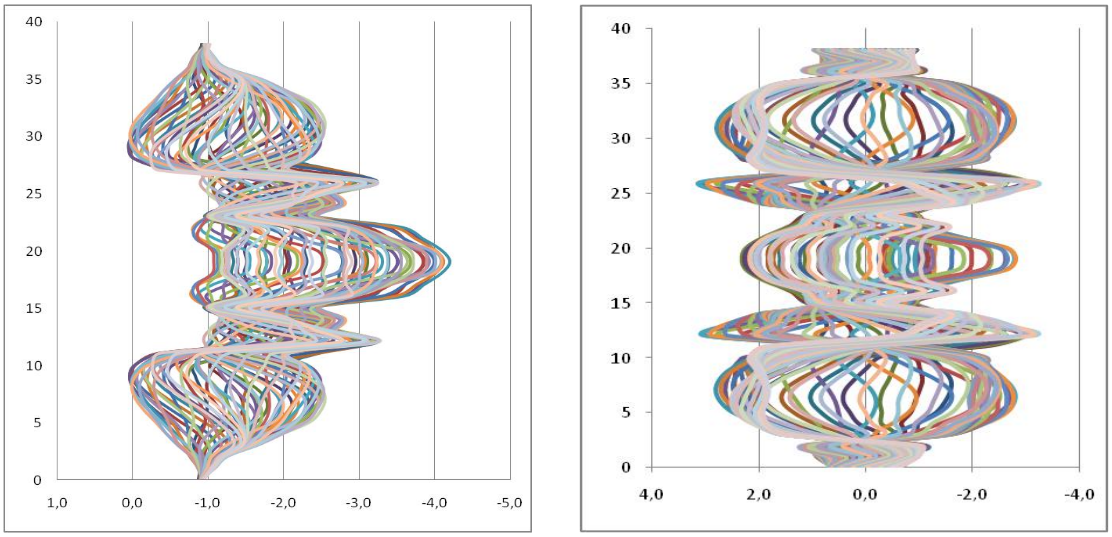

C_D C_L

Fig. 5.3 Drag coefficient C_D (left) and Lift coefficient C_L (right) along time.

Figure 5.3 (left) shows the IL force, or drag force and the CF force, or lift force (right), distributions along riser length and time (one curve for each time step) for the case of Reynolds 42K. The drag force envelope (left) has a flow-wise bending component, in spite that the flow velocity is constant, what indicates that riser average deviation and vibration has a feedback effect on the drag force. Meanwhile, the lift force envelope, as it was to be expected, is symmetric. The drag force curve maximum is located at riser middle length which corresponds with the position of maximum CF oscillation amplitude, see fig. 3.1. The maxima for the lift force curve take place at several riser lengths with slight differences among them despite the first order oscillation that show the CF oscillation envelope. The relationship between oscillation envelope shapes and force envelope shapes is not clear. Only Bourghet et al. (2011a) show both being also different but not finding the possible reason. It might be related to the IL oscillation mode, a 3rd mode, and its influence in flow-to-rise relative velocity.

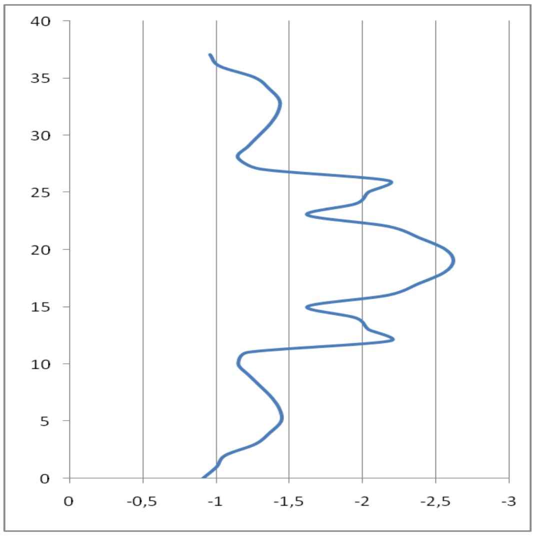

$\bar{C}_D$

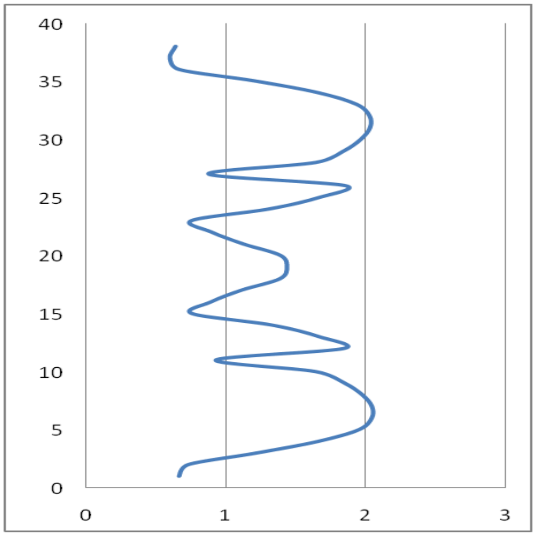

$\bar{C}_L$

Fig. 5.4 Time average drag coefficient (left) and time average lift coefficient (right).

Fig. 5.4 shows the time average curves of the drag and lift forces coefficients of former figure 5.3. As referred by Sarpkaya (2004), since the experiments of Humphries and Walker (1987), until those of Resvanis et al. (2012) in the SHELL experiments, the reported drag coefficient for risers in uniform flow is much larger than in the case of a fixed non-vibrating long cylinder, which value is regarded to be 1.0, Blevins (1984). In fact, Humphries and Walker (1987) reported riser length-averaged drag coefficient values of 1.5 and Resvanis et al. (2012), values from 1.5 to over 2. As observed in figure 5.4 left, the value of the $\overline{C_D}$ at the riser fixed extremes is near 1, as that of the stationary cylinder, as riser in its extremes is stationary. Out of the extreme zones, where the riser oscillates, the value increases with the oscillation amplitude to values of drag coefficient near 2 and even 2.5. Also, Bourghet et al. (2013) reported values in this range.

. .

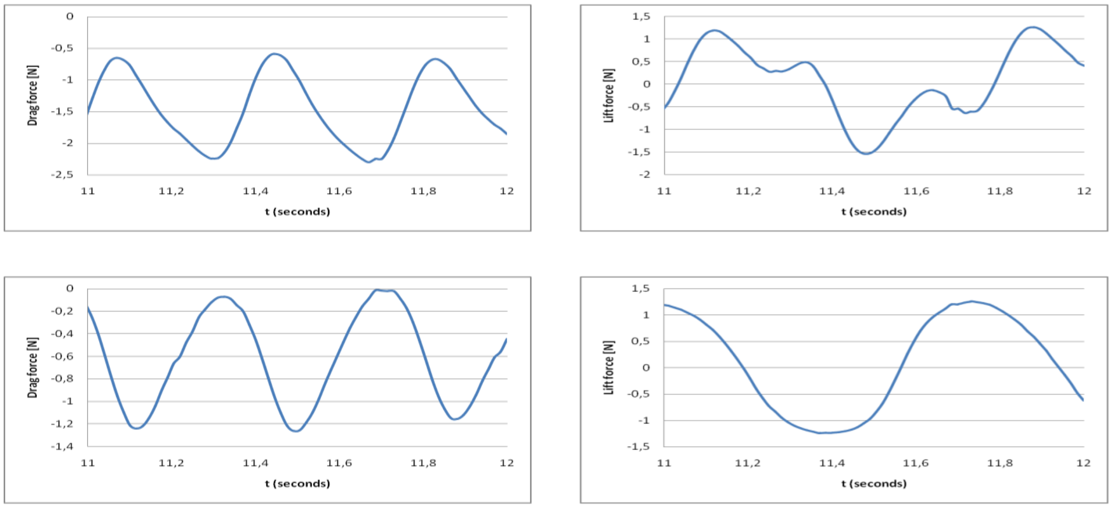

Fig. 5.5 Drag force (left) and lift force (right) at sections 19 meter (up) and 10 meters (down).

In figure 5.5 can be observed the results for the drag and lift forces along time for sections at riser middle length (19 m) up, and at 10 m length, each section consisting of the riser 38.1 mm (1.5 “) spanwise strip containing the regarded spanwise values.

It can be observed the general sinusoidal behavior in all figures excepting the case of the lift force at the central section (top right figure) that shows a smaller peak between the maxima and the minima. This might correspond with the change of oscillation mode as was observed in figure 3.1 top right, the oscillation mode was shifting from a 1st order to a 2nd one, appearing already for some oscillation curves of some instants, a shape with several waves, indicating this change of oscillation mode.

5.4. Conclusions

The main conclusions are:

- Drag coefficient decreases while Reynolds number increases. It varies from 1.5 to 1.6. An average value of 1.5 for the sake of analytic calculations is a good assumption. These values are like those presented by other authors for lower Reynolds number ranges.
- CF coefficient at riser extremes is 1.0, the value for a fixed cylinder, what results logical as these sections do not move.
- Lift coefficient varies little with Reynolds number in a value slightly lower than 1.4.
- Although considering an even value of drag and lift coefficients for analytical purposes, drag and lift force distributions along riser length are not even but present oscillations.
- Both IL and CF force distributions are symmetric in z-axis, what is logical for an uniform flow distribution.
- IL force distribution is not symmetric in its direction (x-direction) but is bent in the upstream direction. This means that force is related with riser relative velocity to the bulk flow. When riser moves downstream in its IL oscillation, the riser and flow relative velocity is lower than where riser moves upstream.
- CF force distribution is symmetric in its direction (y-direction). This corresponds well with the symmetric CF oscillation and the fact that this oscillation is always perpendicular to the bulk flow.
- IL force distribution has a third order pattern shape, as the IL oscillation mode, with the central wave being less “harmonic” than the lateral ones.
- CF force distribution has also a third order pattern shape.
- For both IL and CF force distributions, two sharp force oscillations appear at 1/3 and 2/3 of riser length. They seem related to points were riser vibration changes of direction, moving in one direction the riser length above these zones and in the other direction the riser length below these zones.
- Time histories of drag force appear to be more “harmonic” than lift force histories that may, in some cases, appear to be more “chaotic”.

Chapter 6

6. Synchronization analysis.

6.1. Introduction

Synchronization or lock-in are the names given to the phenomenon when vortices spreading frequency equals the riser transversal oscillation frequency, hence, appearing an equal frequency in the fluid-dynamic transient behavior (vortices) and in the structural transient behavior (riser oscillation). Synchronization has been related and proved to be connected to the largest rigid body oscillation and highest probability of failure and damage. In fact, it was this phenomenon which triggered the study of VIV as responsible of tall chimney falling back in the XIX century, Strouhal (1878).

For rigid cylinders, of a given mass and with fixing systems of a given stiffness and damping, the synchronization frequency results in a single value and the synchronization behavior appears as a narrow flow velocity range where oscillation amplitude suddenly increases as it was explained in chapter 1, fig 1.16.

But for elastic risers the natural frequency values are several, forming a spectrum, being possible the synchronization at several different flow velocity values and oscillation amplitudes, which are not necessary to be maxima. Furthermore, it is regarded that, for uniform flows, the lock-in takes place in the whole riser length meanwhile for linearly sheared flows takes place only in a certain riser length. Also, for uniform flows oscillation amplitudes and, hence, tension level and failure probability are higher than in the sheared flow cases, Resvanis et al. (2012).

6.2. Procedure

The synchronization is, hence, analyzed by means of checking the riser transversal oscillation frequency and the vortex shedding frequency, method proposed by Bourghet (2011a), and observing when these two values are equal, therefore, they are synchronized. Using the ANSYS CFX post processing tool, the riser transversal oscillation is obtained by extracting the oscillation time histories at different riser span points from the transversal oscillation response envelopes, as it was done in chapter 3, fig. 3.5. The vortex shedding frequency is obtained by measuring the transversal component of the flow velocity at a point located several diameters, more precisely 15 riser diameters, behind the riser and at the same riser span points. To do so, virtual points are located at the simulation domain at such locations. At those points the flow velocity components are measured at every timestep, obtaining the curves of flow velocity along time at those points. The distance of 15 diameters between riser location and flow velocity measurement is taken as a mean to avoid capturing the flow velocity produced by the riser oscillation instead of the one produced by the vortex shedding itself, Bourghet (2013).

The frequency values are obtained by measuring the time between oscillation peaks or nodes, time that represents the wave period and its inverse is the frequency value.

Other method to check the frequencies is to carry out a Fast Fourier Transform (FFT) to these oscillation and velocity signals. The FFT transforms those signals from their time-domain to a frequency-domain. Hence, observing the main frequencies is direct in the resulting curves.

A third and last method is to obtain the orbital trajectories. These trajectories are the real oscillations for a certain riser spanwise point. This is, the combined IL and CF oscillations as they really take place. It is known, Dahl et al. (2008), Xiao and Wang (2016) that most of these trajectories form a lemniscates shape, indicating the observed IL and CF vibration ratio of 2, when these shapes are formed counterclockwise when seeing from the top, it indicates synchronization, Bourghet et al. (2011b). This trajectory condition will be taken as the criterion of synchronization appearance.

a)

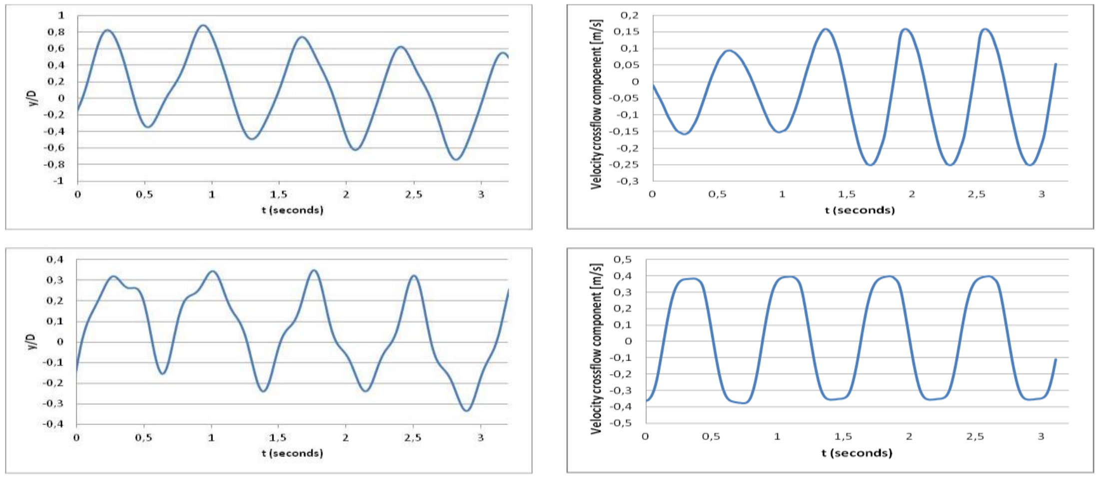

b)

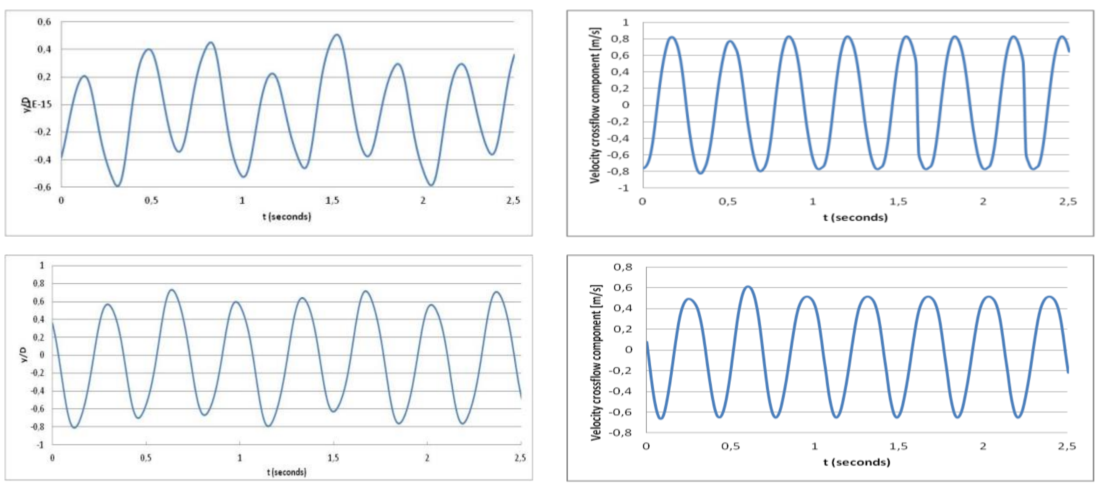

c)

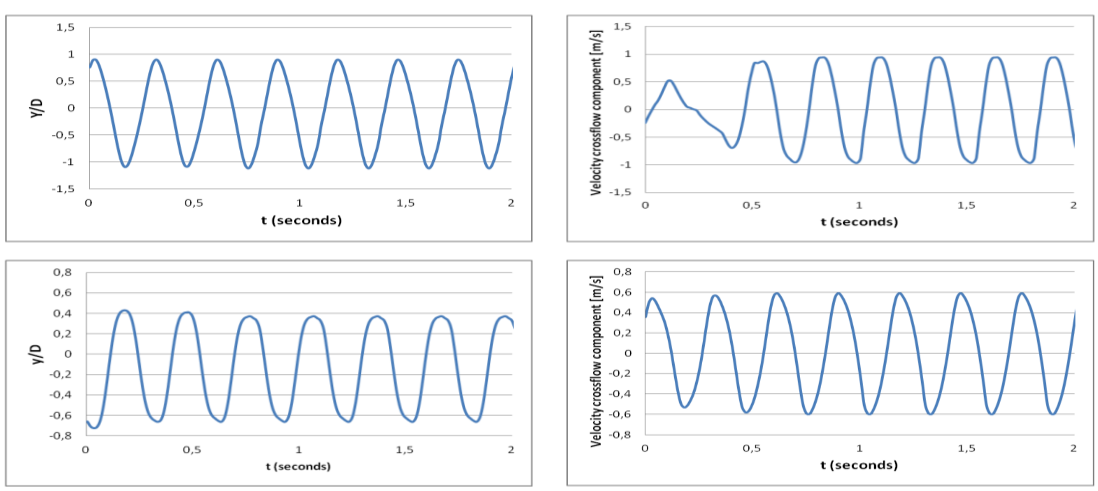

Fig. 6.1: Riser CF oscillation (left) and transversal flow velocity (right) for sections Z/D = 237.5 (upper) and Z/D = 125 (lower) and for the three Reynolds numbers: a) Re = 42K, b) Re = 84K and c) Re = 126K.

6.3. Results

The synchronization or lock-in phenomenon is analyzed for the three Reynolds number cases. In figure 6.1 the riser CF lateral oscillation at the two displayed riser sections is shown again on the left side. The transversal component of the flow velocity at a point 15 riser diameters downstream of the riser and at the same riser spanwise point can be seen on the right side. The comparison of frequency values for both the CF riser oscillation and the transversal velocity component as a means of quantifying the vortex shedding frequency is the method to analyze synchronization, Bourghet et al. (2011a). The analysis is carried out for the same riser spanwise values Z/D = 125 and 237.5 taken in chapter 3.

For the Reynolds number 42K case the results show that the periods between curve nodes, that is, where oscillation curves cross the y = 0 axis, for both the oscillation frequency of the transversal component of the flow velocity, and the frequency of CF vibrations, are 1.32 $\pm$ 0.005 Hz for both spanwise points.

The other way to measure these frequency values is shown in figure 6.2, which displays the CF oscillation and transversal velocity component results in the frequency domain instead of in the time domain. The frequency-domain results are obtained by applying the Fast Fourier Transform to the time-dependent results. The frequency value 1.32 Hz is again obtained. This frequency is lower than the natural frequency for such vibration modes, 1.67 Hz. This effect has also been found by other authors, Bourghet et al. (2011a, 2013) and assigned to damping produced by water.

a)

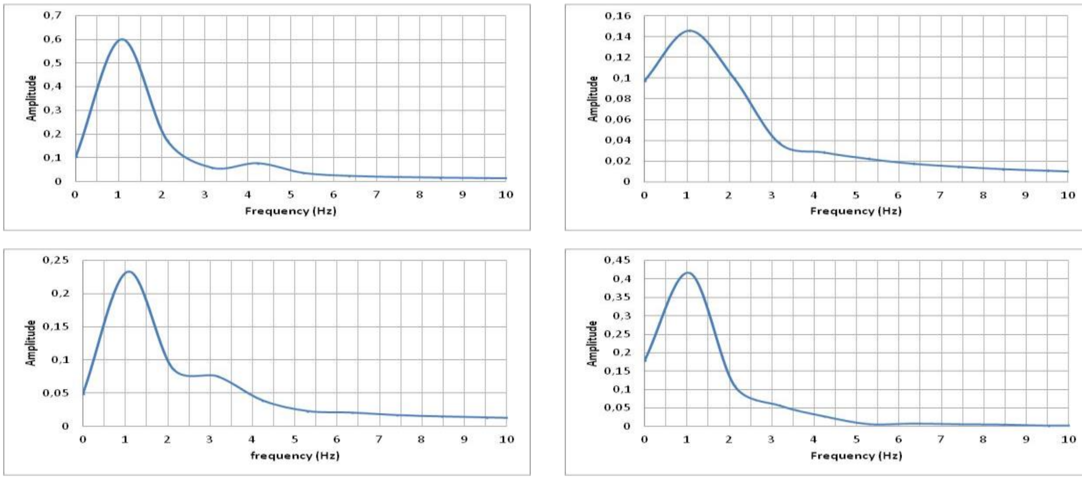

b)

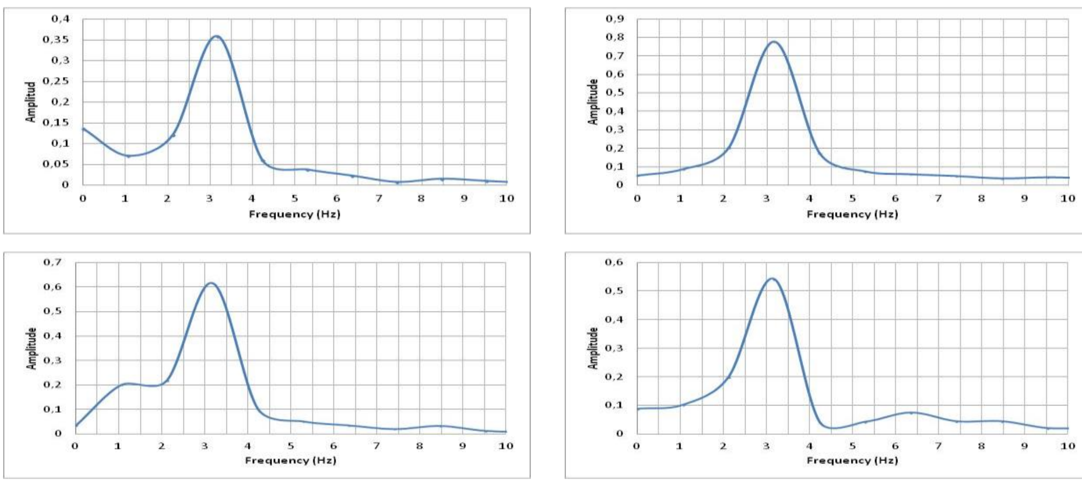

c)

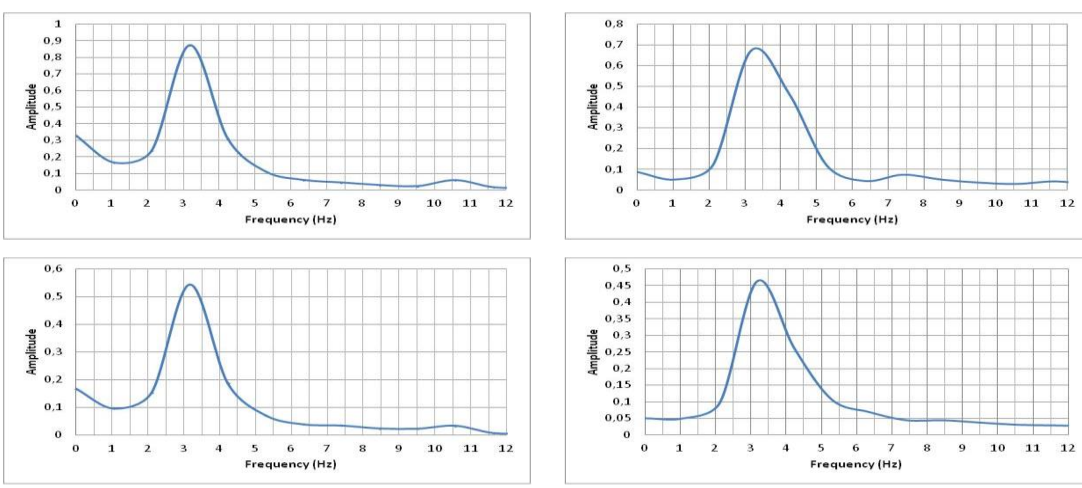

Fig. 6.2: Frequency spectra of the riser CF oscillation (left) and transversal flow velocity (right) for sections Z/D = 237.5 (upper) and Z/D = 125 (lower) and for the Reynolds numbers: a) Re = 42K, b) Re = 84K and c) Re = 126K.

Figure 6.2 also shows that the riser oscillation presents two peaks, one at the above main frequency, and a second one at about three times this frequency and of smaller amplitude. For Reynolds number 42K the first frequency of the spectrum is the frequency with larger amplitude meanwhile for Reynolds number 84K and 126K the amplitude for the first frequency value is small and it is the third frequency the one with larger amplitude. This is the second harmonic of the oscillation. The transversal velocity spectrum shows only one frequency peak, the vortex shedding frequency.

Lock-in takes place at the main frequency, defined this main frequency as the frequency of the largest oscillation amplitude (to be remembered that real oscillation can be decomposed in several harmonic oscillation, each one with a different frequency of the frequency spectrum and different amplitude) as observed by Bourghet et al. (2011a). The difference in values between the CF oscillation and the transversal velocity component is small enough to be considered lock-in.

Figure 6.3 shows the trajectories of different Z/D sections in their X – Y planes. The forms that appear are typical of tensioned risers, and like those observed by Xiao and Wang (2016) with some differences due to the much higher Reynolds number range. These differences are: first, that both the IL and CF amplitudes are much larger, and second, that both the IL and CF oscillation amplitudes increase with Reynolds number. However, the IL amplitude increases in a particular way: as the Reynolds number grows the trajectory tends to “collapse” into a thick curve. This is, as the Reynolds number increases, and for a certain CF position of the trajectory, the differences of IL amplitudes among the several oscillation periods are smaller. As an example, for Z/D = 50 the trajectory for Re = 84K is like a lemniscate, but when the Reynolds number increases to Re = 126K the trajectory “collapses” to almost a half-circumference.

The lemniscate “collapsing” occurs as the riser is already much tensioned in the IL direction. The combination of a high flow velocity and a high Young´s modulus value leads to this high tensioned riser. Hence, the vibration amplitude decreases as vortex shedding forces are not strong enough to overcome the riser tension.

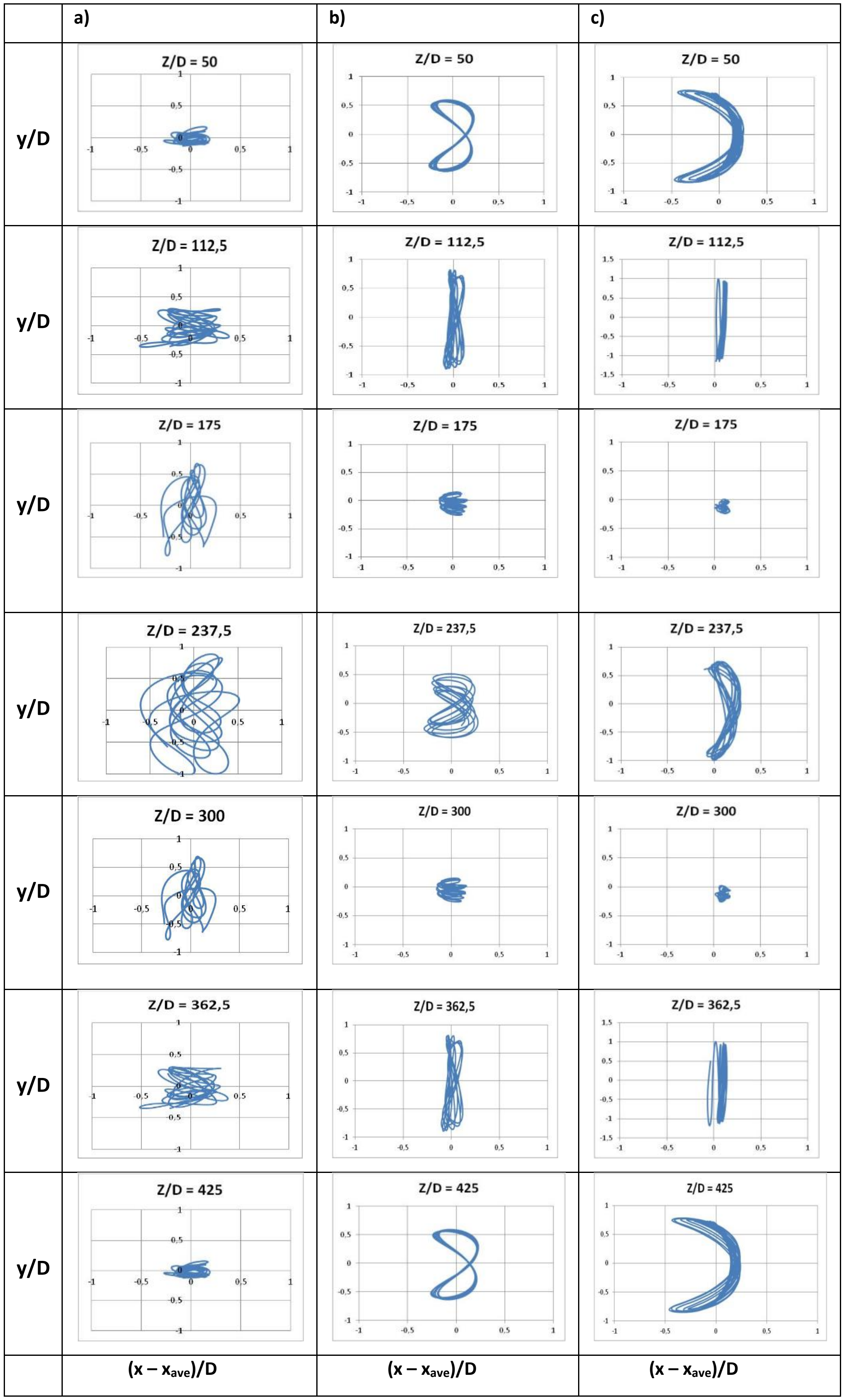

Fig.6.3: Trajectories of different riser Z/D sections for a) Re = 42K, b) Re = 84K and c) Re = 126K.

It must be noticed that this “collapsing” cannot be observed if the general IL oscillation is given, regarding this general oscillation as the x- coordinate difference in the orbital oscillation graphics. But this IL global oscillation is not really the IL oscillation, but the result of the IL oscillation transported by the CF oscillation. In example, for the bottom-right graph of figure 6.3, the one for Reynolds number 126K and y/D= 425 the global IL oscillation ranges from +0.2 to -0.4 (global maximum and minimum) meanwhile the real IL amplitude is the graph x-coordinate difference for any given y-coordinate.

Also interesting is the fact that the “non-collapsed” trajectories move counterclockwise. According to Bourghet et al. (2011b), the counterclockwise direction is predominant in the synchronization region. Thus, this movement direction corresponds well with the equality of CF oscillation and transversal velocity frequency values found in the synchronization chapter. In the “collapsed” trajectories there is no room for clockwise or counterclockwise movements.

Comparing these results with the low Reynolds numbers of Xiao and Wang (2016), much bigger amplitudes in the CF direction can be observed, but in the IL direction the higher average deformation and tension produces smaller amplitude, as the vortex shedding forces to average drag force ratio becomes smaller. The CF oscillation amplitude increases with the Reynolds number following the observations of the tests carried out for the same Reynolds number range by Resvanis et al. (2012).

Analyzing crossflow oscillation and transversal velocity component frequencies as well as orbital trajectories, it can be deduced which cases present synchronization. In the present work it will be regarded as synchronization the cases where the two requirements are fulfilled: equality of the two types of frequencies and the appearance of lemniscates orbital trajectories.

Hence, case of Reynolds 42K will not show synchronization, although both oscillation and velocity frequencies are near. The case of 84K will present a clear synchronization behavior, with equal frequencies and lemniscates trajectories. At the same time, this synchronization behavior does not imply that the oscillation amplitude grows suddenly but grows steadily with Reynolds number. This corresponds well with the results of Bourguet et al. (2011a), Resvanis et al. (2012)

and Xiao and Wang (2016) who obtained synchronization cases where the oscillation amplitudes increased with Reynolds number without the appearance of any amplitude sudden jump. This indicates that, for flexible risers, in opposite situation to rigid cylinders, the oscillation amplitude, tension and riser risk will grow steadily with Reynolds number. The reason might be that, for a rigid cylinder, therefore, not deformable, all its sections behave in the same way, this is, the body and fluid movements are the same for all the cylinder spanwise sections. This is not the case for the flexible riser where its movement is different in amplitude and velocity for each riser spanwise section.

The case of Reynolds 126K is a special case, as no other research group has published a case at such Reynolds. It shows lemniscates trajectory but almost collapsed into a curve not containing a surface. This seems the result of the impossibility of the in-line oscillation having a significant amplitude for any given crossflow trajectory point, due to the large drag force upon the riser.

6.4. Conclusions

The conclusions of this chapter are:

- Both measuring time between peaks in the oscillation or carrying out a FFT methods give the same frequency values.

- The FFT method allows observing the frequency of secondary peaks representing other frequencies of the spectrum with significant amplitudes.

- The FFT method also allows observing how, as Reynolds number increases, the main peak moves to a higher frequency value. So, for Reynolds number 42K the main peak takes place for the first value of the analytically and by simulation calculated spectrum, about 1 Hz, tables 3.7 and 3.8, regarding the vibration mode of first order. For Reynolds number 84K and 126K, the peak has moved to the frequency of the third order vibration mode, about 3.0 and 3.5 Hz, respectively.

- The orbital trajectories show different patterns:

  - For the lowest Reynolds number, 42K, no defined trajectories appear. This will indicate that there is no synchronization in this case, although crossflow oscillation and transversal velocity component frequencies are remarkably close.

  - For the medium Reynolds number, 84K, lemniscates appear. This, together with similarity of the movement and velocity frequencies indicate that it is a case of synchronization.

  - For the upper Reynolds number, 126K, lemniscates appear but almost collapsing in a one-dimensional curve. This effect is due to the high drag produced by the already high flow velocity that makes that oscillation in the In-line direction can be extremely small. It must be noticed that in the spanwise points of maximum CF amplitude the IL amplitude is not large. Viewing only the envelopes this small IL amplitude cannot be observed. Due to the shape for Z/D = 237.5 that is a lemniscate, it can be deduced that it is also a synchronization case.

- Finally, a clarification of the phenomenon of synchronization can be given.

    - The synchronization in elastic risers does not represent a condition where a sudden leap on oscillation amplitude takes place. This was the case of the elastically mounted rigid cylinder resulting of a punctual resonance condition for the given single values of the stiffness and damping of the elements (springs and dampers) that comply their connection to the place where they are installed.

    - The synchronization in elastic risers takes the form of a stabilized oscillation in both frequency and amplitude, resulting of a balance between fluid flow and riser mechanical characteristics and where oscillation amplitude keeps growing as Reynolds number increases although the synchronization condition disappears.

    - Hence, synchronization definition is that of Dahl (2008), section 1.8, taking place what he defined as wake capture, this is, the wake captures the body oscillation, changing natural frequency to an effective one. The characteristic of self-sustained represents the idea of a synchronization condition becoming constant and stable. This is, riser frequency and amplitude keeping constant as well as vortex shedding frequency, which is not the Strouhal frequency but the commented effective frequency.

Chapter 7

7. Scaling trials.

7.1. Introduction

An important observation during the development of this thesis has been the inexistence of a model to predict a certain riser behavior knowing the behavior of other risers. As an example, there is no riser scaling theory, so, it is not known how to test a reduced scale riser in a towing tank and re-scale up the results to the real size riser that can be 50, 100 or 300 m long or even more. Also, there is no knowledge of how a riser will behave if, for example, in a certain project it is decided to change its construction material, even for a similar steel but with a different Young´s modulus.

Riser behavior is defined by several factors, as it was explained in chapter 1.7, these are:

- Geometric parameters.
    - Cylinder diameter
    - Cylinder length
    - Cylinder surface rugosity.
- Fluid-dynamic parameters:
    - Fluid density
    - Fluid viscosity
    - Bulk flow velocity

- Structural parameters:
    - Body mass (without added mass)
    - Body structural damping
    - Body stiffness
- Structural parameters to add for the case of elastic cylinders:
    - Flexural rigidity
    - Tension

The geometric parameters are represented by dimensionless parameters as:

- Length/diameter ratio, L/D.
- Rugosity/diameter, μ/D.

The fluid-dynamic parameters can be unified in the Reynolds number:

- Reynolds number: $Re = \frac{\rho V D}{\mu}$, where ρ is the fluid density, V is the fluid velocity and μ the fluid viscosity.

And, finally, the structural parameters, where there is not a defined and agreed system definition.

- The Scruton number was proposed already in the 60's, defined for the rigid cylinder as, Scruton (1965):

$$S_c = \frac{2cm}{\rho D^2} \tag{7.1}$$

Where c is the structural damping, m the body mass (including the added mass), ρ the fluid density and D the cylinder diameter. To be noticed that cylinder length does not affect, being the cylinder rigid. The differential equation that represents the rigid cylinder movement is:

$$(m(z) + m_a(z))\frac{\partial^2 x}{\partial t^2} + c\frac{\partial x}{\partial t} = F_x \tag{7.2}$$

Meanwhile the elastic cylinder is governed by the equation:

$$\frac{\partial^2}{\partial z^2}\left[EI\frac{\partial^2 x}{\partial z^2}\right] - \frac{\partial}{\partial z}\left[T\frac{\partial x}{\partial z}\right] + (m(z) + m_a(z))\frac{\partial^2 x}{\partial t^2} + c\frac{\partial x}{\partial t} = F_x \tag{7.3}$$

Where two parameters appear: the flexural rigidity EI, product of the riser material Young modulus E and the riser section inertia moment I, and the riser tension T. This tension T, if it is regarded the fact that changes with the force produced by the fluid flow upon the riser as analyzed in chapter 3, depends on fluid velocity V, fluid density ρ and riser diameter D. But, even if these parameters define basically the Reynolds number, the elastic cylinder is not represented by this number. The reason is that, as tension depends on the fluid drag force, and this is a function of the squared power of velocity, two different elastic cylinders in water that fulfill that their product of flow velocity and cylinder diameter are equal will have the same Reynolds number, but not the same drag force, that will be stronger in that one immersed in a higher flow velocity, even if its diameter is smaller, due to this squared power velocity dependence.

On the other hand, without a scaling theory, research works in the field of VIV will remain being inconsistent, in the author´s opinion and according to what has been observed in the bibliography. This means that every research work will choose a towing tank riser tests of which they will have enough information and analyze it for some parameter values but will be unable to predict its performance for any other value of any of the riser parameters. Besides, all the towing tank risers are quite limited in length for riser analysis, being 38 meters, the riser chosen for the present work, the longest ever analyzed and marine wind-power devices at this depth are not in platforms but clamped to the seabed. Platforms will be used from 60-meter depth above, as explained in chapter 1.

For this reason, during the development of this thesis it was investigated the behavior of risers when changing one parameter different to the flow velocity, more precisely, the riser material Young´s modulus. To do so, the riser properties, length, diameter, etc., and flow velocity were kept constant, this last one in 0.6 m/s (Reynolds number 42K) and the Young modulus was varied.

7.2. Procedure

All the results shown until this chapter were of a riser with Young modulus 3.48e+10 N/m^2, corresponding to the material used in the SHELL experiments. Steel ASTM-A36 Young modulus is 2.00e+11 N/m^2. In the next section, devoted to results, two lower values are analyzed: 2.85e+8 N/m^2, corresponding to High-Density Polyethylene, HDPE, material known by its high-strength-to-density ratio and 1.59e+9 N/m^2, corresponding to a nylon/polystyrene, very frequently used in mooring systems.

The exact values of these Young´s modulus materials arose from a trial to define an equivalent homogeneous riser to that used in SHELL experiments. As it was commented in section 3.2, the only riser which tests reached Reynolds number above 20K was one of the three tested in the SHELL experiments which partial results were published by Resvanis et al. (2012). This riser experienced Reynolds numbers from 42K to 126K (the same range of the computational simulations of this work) by means of covering other 27 mm diameter riser with a plastic layer, until achieving a final diameter of 80 mm. Unluckily, Young modulus of such plastic layer was not published and any results for an appropriate results extract validation were not possible to be obtained (as informed by Professor Resvanis after contacting him, as those results are property of the oil company that will not share them).

The path taken was to analyze the three Young´s modulus values, ranging an e+8 to an e+10 N/m^2 range that covers the whole expected range of Young´s modulus values from material that can be once used to build the sea-wind-power platform tension legs or other mooring system, keeping constant all the other physical properties, geometry, and mesh characteristics, for the sake of correct comparison.

7.3. Results

The results obtained with a Young´s modulus of 2.85e+8 N/m^2 are shown first.

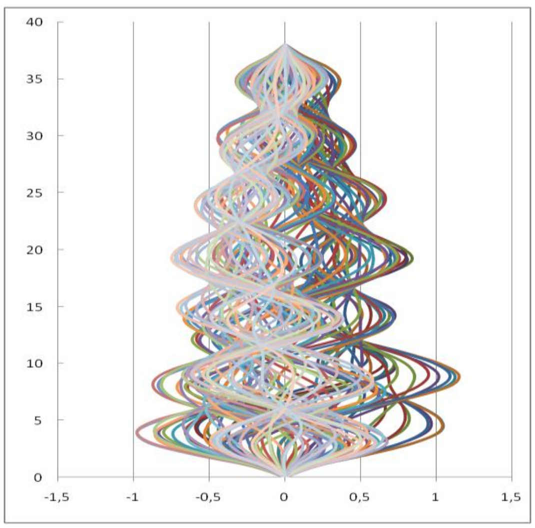

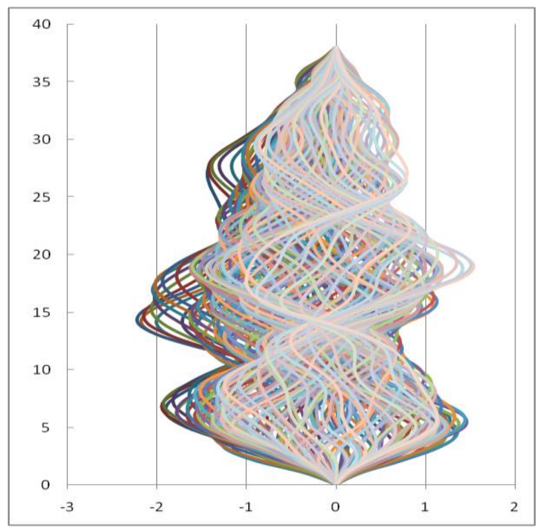

$(x\text{-}x_{mean})/D$ *y/D*

Fig. 7.1 Riser response envelopes for IL oscillation (left) and CF oscillation (right).

Figure 7.1 shows the riser envelopes for a flow velocity of 0.6 m/s, corresponding to a Reynolds number of 42K. The oscillation modes are a 7th mode for the IL oscillation and a 3rd mode for the CF oscillation, beginning to shift to a 4th mode. The amplitude of both oscillations increases with the depth, although the flow is uniform. This behavior was also observed by Xiao and Wang (2016) in one of the two uniform flow cases that they analyzed.

The CF oscillation average amplitude was about three times the IL amplitude for the highest Young´s modulus case analyzed in the previous chapters of the thesis meanwhile the CF oscillation amplitude is about double than the IL oscillation in the present case. Hence, both oscillation mode and oscillation amplitudes increase when Young´s modulus decreases. As commented before, these results cannot be compared with other authors, as no investigation keeping all the parameters, but Young´s modulus (material) has been carried out.

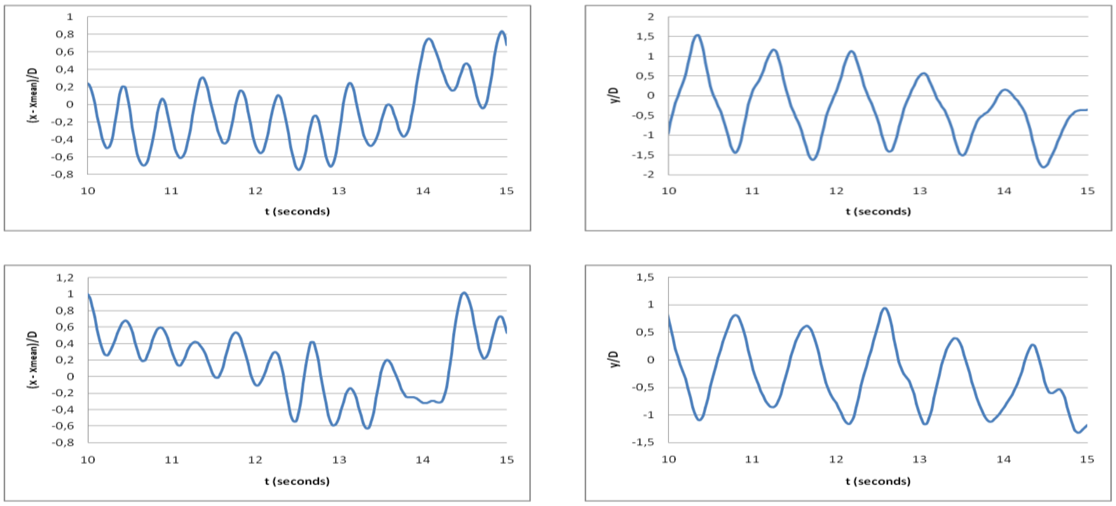

Fig. 7.2 Oscillation time histories at z = 19 m (up) and z = 10 m (down): IL oscillation (left) and CF oscillation (right).

In figure 7.2 can be observed the oscillation time stories at the same sections of former chapters (19 m section, the riser half length, above and 10 m section below) and again for the IL oscillation on figures on the left side and CF oscillation on figures of the right side. The IL oscillation shows sudden changes of oscillation range which must be linked to the behavior of travelling waves. The oscillation remains several seconds in one range, from before 10 seconds until about 13 seconds and then changes of range. His effect is observed both for the 19-meter and 10-meter sections. The CF does not show such behavior. It maintains a regular oscillation frequency pattern for both regarded sections with changes in oscillation amplitude that decreases with time. Despite this changing behavior the IL oscillation frequency is about double of the CF one, as indicated by the double number of peaks of the IL oscillation in the same period. Hence, this figure show that for lower Young´s modulus materials the oscillations will be less regular with several frequencies of their oscillation frequency spectrum being of consideration and not ruled only by its first harmonic as occurs with higher Young modulus material risers.

Finally, a case with also a flow velocity of 0.6 m/s, corresponding with a Reynolds number of 42K but with an intermediate Young´s modulus value of 1.59e+9 N/m^2, is analyzed.

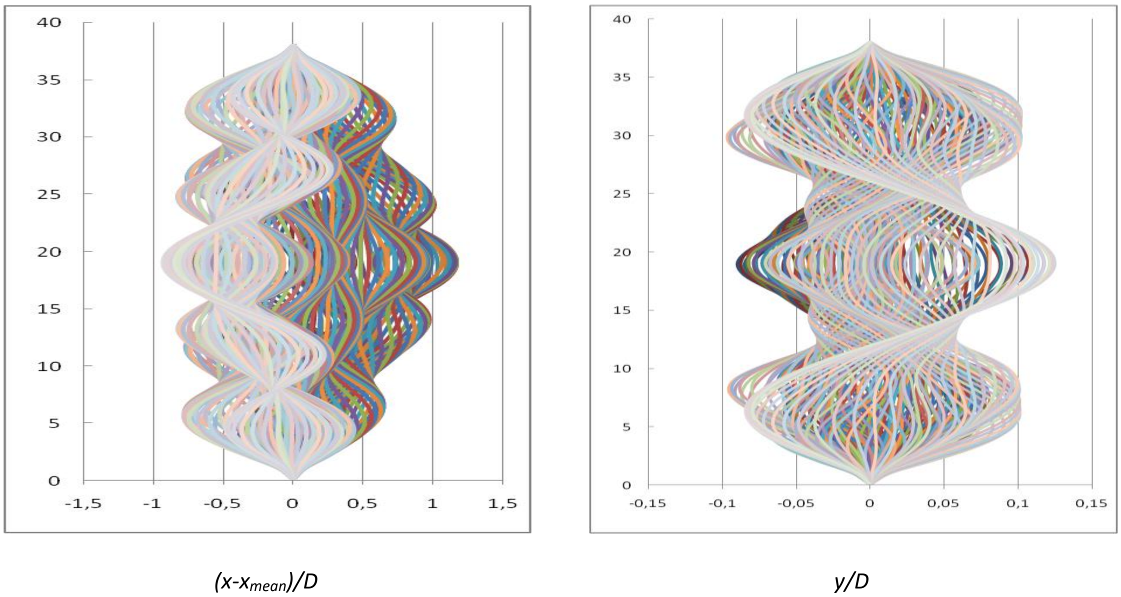

Fig. 7.3 Riser response envelopes: IL oscillation (left) and CF oscillation (right).

As it can be observed in figure 7.3 the IL oscillation shows a 5th vibration mode with the largest oscillation amplitude at the central 19-meter section and the CF vibration a 3rd order. Hence, being the Young´s modulus the intermediate one between the two former cases, also the oscillation modes show intermediate orders: 5th for the IL (between 3rd and 7th of the other cases) and a clear 3rd for the CF (between the 1st mode shifting to a 2nd mode of the highest Young´s modulus case, and the 3rd mode shifting to a 4th mode of the lowest Young´s modulus case).

Also, the IL amplitude show intermediate value between the former cases but not the CF amplitude that is quite narrower.

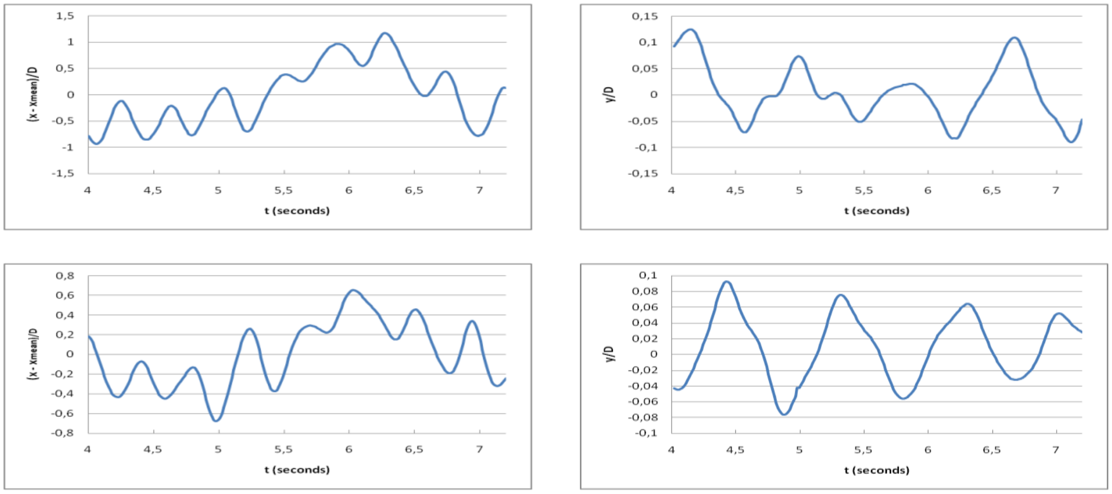

Fig. 7.4 Oscillation time histories at z = 19 m (up) and z = 10 m (down) and IL (left) and CF oscillations (right).

Figure 7.4 shows the oscillation time histories for the two regarded sections: 19 m and 10 m of the riser length. The oscillation is not regular nor for the IL oscillation neither for the CF oscillation at none of the sections. The IL remains for some oscillations in the negative amplitude range (under Y = 0 axis) during 4 oscillations to shift to the positive amplitude range (above Y = 0 axis) during another 4 oscillations, what seems to indicate a lower frequency oscillation. But the frequency measured as the time distance between maxima or minima is quite regular and keeps the double frequency for the IL oscillation than for the CF oscillation, showing 8 peaks the first, for both sections, and 4 peaks the last one, also for both sections.

7.4. Conclusions

The conclusions of this chapter are:

- Riser behavior is quite sensible to the riser material (Young modulus).
- As Young modulus decreases the riser oscillation behavior separates from harmonic oscillation pattern appearing more complex behaviors.

- As Young modulus decreases the riser oscillation modes, for both IL and CF oscillations, increases, for the same flow Reynolds number. In this way, and for Reynolds number 42K:
    - For Young´s modulus in the order 10E+10, IL oscillation order is 3 and CF oscillation order is 1 shifting towards 2 (results of chapter 3).
    - For Young´s modulus in the order 10E+9, IL oscillation order is 5 and CF oscillation order is 3.
    - For Young´s modulus in the order 10E+8, IL oscillation order is 7 and CF oscillation order is 3 shifting towards 4.
- The oscillation envelopes for both IL and CF oscillations are symmetric in the riser axial length for the two higher Young´s modulus values but they are not for the lowest value, where amplitude increases with depth.
- The two lower Young´s modulus oscillations are formed of more than one or two frequency values with significant corresponding amplitudes. This is observed as the oscillation time histories look also harmonic, in the sense of formed by sinusoidal waves, but showing much more variability, with small oscillations in some amplitude range shifting to other amplitude range, sometimes changing from riser dominion side, this is, from the part of the dominion at the riser left side, regarding the flow direction, to the part of the dominion at the riser right side. This can be observed as the amplitude sign changes.
- The research in this field of VIV from the point of view of materials must be a task to be included in the future work aims and where, hopefully, towing tank tests works will appear to allow validation.

8. Final conclusions and further work.

8.1. Conclusions

The thesis main conclusions are:

1. **FSI numerical simulations are an available method to analyze risers** of characteristics (size) and conditions (flow velocity) like those expected for real installations at sea. This is the only possible method as towing tanks cannot test them until a scaling theory was properly developed.

2. **There has been analyzed a riser at higher Reynolds numbers than usually investigated**. The differences and similarities with respect to those risers at lower Reynolds numbers are:

   2.1. For low Reynolds number the riser frequency spectrum is given only by the riser characteristics: geometry (length and diameter), material and installation (fixed ends or cantilever, pre-tensioned or not-pretensioned). For high Reynolds numbers the flow affects the riser frequency spectrum because it produces a significant tension that is added to the pre-tension. This effect makes that the riser frequency increases with respect to those where this effect does not take place.

   2.2. For risers at low Reynolds numbers, the Reynolds number parameter defines the flow affecting the riser but, for high Reynolds numbers, because of the effect commented in the previous point, the Reynolds number is not enough to define the flow. The tension induced in the riser by the flow is the result of the flow drag force upon it. And the drag force varies with the flow velocity second power. Hence, two risers, the first of diameter D and immersed in a flow of velocity V and the second of diameter 2D and immersed in a flow of velocity V/2 will have the same Reynolds numbers but they have not the same VIV behavior as the drag force upon them and therefore their tension and deformation will be different.

2.3. CF oscillation amplitude increases with Reynolds number. Hence, for high Reynolds numbers, CF oscillation amplitudes are larger than those for low Reynolds numbers.

2.4. IL oscillation amplitude grows much less with Reynolds number than the CF oscillation and even get stabilized at some flow velocity. The reason is that the riser at that velocity is already so tensioned (IL is the flow direction, so, the direction in which the riser is tensioned), that the vortices energy is no longer able to increase the oscillation amplitude.

2.5. Riser oscillation modes increase with Reynolds number for any given riser, but different risers may have the same oscillation modes even if their flows Reynolds numbers are much different. The other riser parameters: Young´s modulus and density (material) and riser diameter, are also involved in the determination of the oscillation modes.

3. **The introduction of a new variable, the flow-induced tension, which explains the variation of the riser frequency spectrum with the flow velocity**, was analyzed in a chapter devoted to this new parameter (chapter 4). The way this flow-induced tension appears is the following one: flow produces a drag upon each riser section. The sum of this force along the whole riser length yields a resultant force. According to the statics principles (branch of the mechanics concerned with the analysis of loads acting on a system in static equilibrium), this resultant force is balanced with reactions in the riser fixing points. These external force field produces a riser internal field of stress (tension) and strain (deformation).

4. Hence, an important observation of the present work is that **VIV oscillations take place in the IL tensioned, deformed, and elongated riser**, not upon the initially straight and not tensioned one. Therefore, the riser VIV oscillation frequency spectrum is the spectrum of the flow-tensioned riser which values are different, and flow velocity dependent, of the not tensioned riser values.

5. The average IL elongation is a variable to be found. Then, regarding the riser tension as that produced by tensile stress, the riser vibration frequency calculations accuracy increases significantly.

6. This average IL elongation can be found by calculating the length of the flow-deformed riser. Analytical methods, focused on a pre-design step and, therefore, accepting some loss of accuracy for the sake of simplicity, were surveyed. Four models were investigated. The main outcomes of this analysis are:

   6.1. Generally, there is only one equation relating stress and strain, with the exceptions of: a) the riser as a beam, as the two variables are linked by a riser constant depending on material and section inertia moment, b) the riser as a special case of catenary, due to catenaries initial and final length are known. The catenaries are considered as not elongating systems but of constant length. with their extremes fixed installed at two points which distance is shorter than the catenaries length.

   6.2. Therefore, two models cannot be applied without taken results from simulations, and the other two models that do not need them achieve not enough accurate results. The beam model shows quadratic behavior, following the drag force variation, which is not realistic. This discrepancy is because the riser behaves as a string and not like a beam. The catenaries model overpredict the tension, as riser would correspond with an almost straight catenary and catenary tension increases when its curvature decreases.

   6.3. It has been found a relationship between the Jhingran model and the angle-at-riser-ends model which allows predicting IL average deformation by just knowing the angle of riser deviation at its ends or the deviation in its middle length. These models seem to provide good methods to check the riser situation in real installations and a possible predictor-corrector method to estimate riser elongation and tension.

   6.4. The progressively smaller maximum riser IL deviation has been explained. The riser elongation is linear with tension but, the same increase in length supposes, by pure geometry reason, a smaller increase of maximum deviation.

7. **The C_L and C_D force coefficients have been found for higher Reynolds numbers** and compared to those at lower Reynolds numbers investigated by other authors until date. The drag coefficient decreases with Reynolds number from 1.6 to 1.5 meanwhile the lift

coefficient increases slightly from 1.35 to 1.4 Average values of 1.5 and 1.4, respectively, can be taken for design purposes.

8. Drag and lift force distributions along riser length are not constant, despite the flow being of uniform velocity. Clearly, their behavior is affected by the riser movement, showing a similar pattern and order (number of waves of the force envelope) of the riser vibration. Therefore, forces are linked to the riser relative velocity to the flow.

9. **The synchronization phenomenon has been investigated** through two effects and two methods, one numerical: the calculation of vibration period or frequency of the CF vibration and velocity transversal component, and other graphical: observation of the lemniscate appearance in the riser orbital trajectories. The conclusions are the following ones:

   9.1. Synchronization in elastic bodies is not like that affecting to rigid bodies. When the element is rigid the oscillation frequency is a single value defined by the values of the elements that connect it to the place where it is installed: the stiffness of the springs and the damping coefficient of the dampers. When the body is elastic the body itself has stiffness and damping through its whole volume, what leads to multiple modes of vibration at different frequency values. Any of these frequency values can be excited by the fluid flow.

   9.2. The synchronization process, therefore, takes place in the following manner. The flow starts to make oscillate the riser from its initial situation at rest. Oscillation amplitude and frequency grow until the riser reaches its natural frequency (modified by the flow-induced tension) closer to the flow vortex shedding frequency, that is, it would pass through values of the frequency spectrum which are lower than the closest frequency value to the vortex shedding frequency, as it was observed for the cases of Reynolds number 84K and 126K. When these values are close enough, the vortex shedding gets locked or synchronized with the riser oscillations.

   9.3. For risers at uniform flows there is a frequency of the spectrum quite close to the vortex shedding frequency. This is observed as, measuring both the riser CF oscillation period and the velocity transversal component oscillation period, both are quite similar for the three investigated cases.

9.4. The riser main frequency is the first frequency of its spectrum for Reynolds number 42K meanwhile it is the second for the Reynolds numbers 84K and 126K, as it can be observed in the FTT analysis, where peaks for both frequencies appear but of higher amplitude in the mean one.

9.5. The orbital trajectories can be taken as a discerning criterion for synchronization appearance when both riser oscillation and velocity transversal component frequencies appear to be quite close but not equal, which can be due to numerical accuracy. Therefore, the case of Reynolds number 84K is a clear synchronization case.

9.6. Although the riser is synchronized in its whole length, as immersed in a uniform flow, lemniscates appear in the zone of maximum vibration amplitudes. The appearance of vibration nodes avoids their spreading along the whole riser length.

9.7. The case for Reynolds number 126K is an interesting case with no results previously published. In this case the flow-induced tension is already so high as to reduce the IL vibration amplitude and to make lemniscates to collapse in a thick line. This effect allows distinguishing between an apparent IL oscillation amplitude and a real one.

9.8. The synchronization in elastic risers is not linked to an oscillation amplitude larger than that out of a synchronization regime. The CF oscillation amplitude grows with the Reynolds number independently of whether a synchronization situation takes place or not. The sudden oscillation amplitude observed in elastic fixed rigid cylinders is a phenomenon of such elements that cannot be generalized to elastic cylinders.

10. **VIV phenomenon in risers depends on several parameters**: geometric, as riser diameter and length, of its material, as density and Young´s modulus, and of flow, the velocity (in both linear and quadratic power, related to Reynolds number and drag coefficient, respectively). All former bibliography works focused on riser dependance on the Reynolds number. In the

present work also an investigation about the effect of Young´s modulus has been carried out. The main conclusions of this analysis are:

10.1 Riser behavior is much sensitive to the riser material Young´s modulus.

10.2 As Young´s modulus decreases the riser oscillation separates from harmonic oscillation pattern.

10.3 For the same Reynolds number, both IL and CF oscillation mode orders increase as Young´s modulus decreases.

10.4 The oscillation envelopes for both IL and CF oscillations are symmetric in the riser axial length for the higher Young´s modulus values and increases with depth in the lowest value.

10.5 The two lower Young´s modulus oscillations are formed by waves of several frequencies of significant amplitude in other way than for the highest Young´s modulus where the frequency with significant amplitude is only one.

8.2. Further work

The author of the present thesis works in a company that is already involved in four European Commission Research projects of different technical fields. The proposal of one of them, the project ASTEP (Application of Solar Thermal Energy to Processes), web of ASTEP project (2020), was developed from a former company member Ph. D thesis.

It is the purpose of this thesis author to proceed in the same way. Hence, as soon as this thesis gets accepted for its defense, a proposal writing will be started, together with different companies through all European Union, already contacted and interested in the field.

The scoop of this project will be to reach a Technology Readiness Level TRL of, at least 7, this is, to build a prototype in an operative environment.

The aims of this project will be to analyze VIV parameters not investigated yet as, for example:

- To measure experimentally riser tension as function of Reynolds number to predict the flow-induced tension for any riser and Reynolds number.

- Equal risers differing only in construction material to observe the influence of construction material in the riser behavior.

- Analysis of similar risers result of building several risers changing exclusively the scale, in example one riser and a 25%, 50% and 100% larger riser to develop a scaling theory for risers.

8.3. Publications for this thesis

There has been published the following article where outcomes included in the chapters 3: Reynolds number dependance, 5: Drag and lift forces, and 6: Synchronization analysis, were included:

J. Domingo, l. Pérez-Rojas and H.R. Díaz-Ojeda (2020). Numerical investigation of vortex-induced vibration of a vertical riser in uniform flow at high Reynolds numbers. Journal of Marine Science and Technology, Vol. 28, No. 1, pp. 25-40.

9. Bibliography.

Anaganostopoulus, P. and Iliadis, G. (1998). Numerical study of the flow pattern and the in-line response of a flexible cylinder in an oscillating stream. J. of Fluids and Structures, 12: 225-258.

ANSYS Inc., (2016) ANSYS Solver Theory Guide. Chapter 5: Transient structural analysis equations. Canonsburg. USA

Asociación de Productores de Energias Renovables, APPA, www.appa.es. Energías Renovables. “Balance Energético 2016 y Perspectivas 2017. March 17th, 2017

ASTEP project (2020): https://www.astepproject.eu/

Bachinsky, E. E. and Moan, T. (2012) “Design condiderations for tension leg platform wind turbines”. Marine Structures 29, 89-114.

Batchelor, G. K. “An introduction to Fluid Dynamics”, Cambridge Mathematical Library, 2000.

Blackburn, H. M. and Karniadakis, G.E. (1993) Two- and Three- Dimensional Simulations of Vortex-Induced Vibration of a Circular Cylinder. 3rd International Offshore and Polar Engineering Conference. Singapore.

Blevins, R.D. (1974) Fluidelastic whirling of a tube row. ASME Journal of Pressure Vessel Technology 96, pp. 263 – 267.

Blevins, R.D. (1984) Applied Fluid Dynamics Handbook. Ed. Van Nostrand Reinhold Co.

Bearman, P.W. (1984). Vortex shedding from oscillating bluff body. Annu. Rev. Fluid Mech. 16, 195-222.

Bearman, P.W. (2011). Circular cylinder wakes and vortex-induced vibrations. J. Fluids Struct. 27, 648-658.

Bishop, E.D., and Hassan, A.Y., (1964) The lift and drag forces on a circular cylinder oscillating in a flowing fluid. The Royal Society Publishing. https://doi.org/10.1098/rspa.1964.0005,

Bourghet, R. et al. (2011a). Lock-in of the vortex-induced vibrations of a long tensioned beam in shear flow. J. Fluids Struct. 27, 838-847.

Bourghet, R. et al. (2011b). Wake-body resonance of long flexible structures is dominated by counterclockwise orbits. Phys. Rev. Lett. 107 (134502), 1-4.

Bourghet, R. et al. (2012). Mono- and multi-frequency vortex induced vibrations of a long-tensioned beam in sheared flow. J. Fluids Struct. 32, 52-64.

Bourghet, R. et al. (2013). Phasing mechanisms between the in-line and cross-flow vortex-induced vibrations of a long tensioned beam in shear flow. Comput. Struct. 122, 155-163.

Bourghet, R. et al. (2015). On the validity of the independence principle applied to the vortex-induced vibrations of a flexible cylinder at 60 degrees. J. Fluids Struct. 53, 58-69.

Chaplin, J.R. et al. (2005). Laboratory measurement of vortex-induced vibrations of a vertical tension riser in a stepped current. J. Fluids Struct. 21, 3-24.

Cincotta, J.J., Jones, G.W. and Walker, R.W. (1966). Experimental investigation of wind-induced oscillation effects on cylinders in two-dimensional flow at high Reynolds number. NASA Techn. Memo X-57779.

Constantinides, Y. and Oakley, O.H. (2008). “Numerical prediction of VIV and comparison with field experiments”. Proceedings of the ASME 27th International Conference on Offshore Mechanics and Arctic Engineering, Estoril, Portugal.

Constantinides, Y. and Oakley, O.H. (2006). “Numerical prediction of bare and straked cylinder VIV”. Proceedings of the ASME 26th International Conference on Offshore Mechanics and Arctic Engineering, Hamburg, Germany.

Copple, R. W. and Capanoglu, C. (2012) Tension leg wind turbine conceptual design suitable for a wide range of deep water depths. In: 22nd international ocean and polar engineering conference.

Dahl, J. (2008) Vortex-Induced Vibration of a Circular Cylinder with Combined In-line and Cross-flow Motion. Doctoral Thesis at the M.I.T.

Domingo, J. Perez-Rojas, L. and Díaz-Ojeda, H.R. (2020) Numerical Investigation of Vortex-Induced Vibration of a Vertical Riser in Uniform Flow at High Reynolds Numbers. J. of marine Science and Technology, Vol. 28, No. 1, pp. 25 – 40.

Dong, S., Lucor, D. and Karniadakis, G.E. (2004) Flow past a stationary and moving cylinder: DNS at Re = 10,000. Proceedings of the 2004 Users Group Conference. June 2004, pp. 88 –95.

EDP (2020): https://www.edp.com/es/innovacion/windfloat

Equinor (2020): https://www.equinor.com/en/what-we-do/floating-wind.html

Energías Renovables (2019): www.energias-renovables.com/panorama/el-escenario-pinta-positivo-para-las-renovables-20191002

Energías Renovables (2018): https://www.energias-renovables.com/eolica/la-eolica-marina-factura-5-000-millones-20181026

EUROSTAT (2019) https://ec.europa.eu/eurostat/statistics-explained/index.php/ Renewable_ energy_statistics.

Evangelinos, C. and Karniadakis, G. E. (1997). Transition in the wake of flexible cables and beams. In: 7th ISOPE Conference, Honolulu, Hawaii.

Evangelinos, C. and Karniadakis, G. E. (1999). Shedding patterns in flow-structure interactions. Journal of Visualization, Volume 2, pp. 135-142.

EWEA (2009) coste de las plataformas de la energía eólica

Feng, C. C. (1968) The measurement of vortex-induced effects in flow past a stationary and oscillating circular and D-section cylincers. Master Thesis, University of British Columbia, Vancouver, B.C. Canada.

Fulton, G., Malcolm, D., Elwany, H., Stuart, W., Moroz, E. and Dempster, H. (2007) Semi-submersible platform and anchor foundation systems for wind turbine support. Tech. rep. NREL/SR-500-40282. National Renewable Energy Laboratory.

Fujarra, A.L.C., Pesce, C.P. Flemming, F. and Williamson, C. H. K. (2001). Vortex-induced vibration of a flexible cantilever. J. Fluids Struct. 15(3): 651 – 658.

Gabbai, R.D., Benaroya, H. (2005). An overview of modeling and experiments of vortex-induced vibrations of circular cylinders. J. Sound Vib. 282, 575-646.

Gao, Y. et al. (2015). VIV response of a long flexible riser fitted with strakes in uniform and linearly sheared currents. Appl. Ocean. Res. 52, 102 -114.

Garrido, C.A. (2015) "Hydrodynamic forces on heave plates for offshore systems oscillating close to the seabed or the free surface". Doctoral Thesis.

Gere, J. M. and Timoshenko, S. P. (1988) "Mecánica de Materiales". International Thomson Editores. 4th Edition. ISBN 968-7529-39-3.

Govardhan, R.N., Williamson, C.H.K. (2006). Defining the modified Griffin Plot in Vortex-induced vibration: Revealing the effect of Reynolds number using controlled damping. J. of Fluid Mechanics 561, 147-180.

Gu, J. et al. (2013). An experimental investigation by towing tank on VIV of a long flexible cylinder for deep water application. J. Mar.Sci. Technol. 18, 358-369.

Guilmineau, E. and Queutey, P. (2002) A Numerical Simulation of Vortex Shedding from an Oscillating Circular Cylinder. J. of Fluids and Structures. Volume 16. Issue 6. Pp. 773 – 794.

Guilmineau, E. and Queutey, P. (2004) Numerical simulation of vortex-induced vibration of a circular cylinder with low mass-damping in a turbulent flow. J. of Fluids and Structures 19, 449 – 466.

Griffin, O.M. (1980) Vortex-excited cross flow vibrations of a single cylindrical tube. In: Flow-induced vibrations, ASME Congress, San Francisco, California, S.S. Chen & M.S. Bernstein (eds).

Hartlen, R.T. and Currie, I.G. (1970) Lift-oscillator model of vortex-induced vibration. Journal of the Engineering Mechanics Division 96: 577-591.

Henderson, A.R., Argyriadis, K., Nichos, J. and Langston, D.(2010) Offshore wind turbines on TLPs – assessment of floating support structures for offshore wind farms in German waters. In: 10th German wind energy conference. Bremen, Germany.

Holmes, S., Constantinides, Y. and Oakley, O.H. (2006). "Simulation of riser VIV using fully three dimensional CFD simulations". OMAE2006-92124. In: Proceedings of the ASME 26th International Conference on Offshore Mechanics and Arctic Engineering, Hamburg, Germany.

Huang, S., Chen, H.C. and Chen, C.R. (2009) Vertical Riser VIV simulation in uniform currents. J. Offshore Mech. Artc. Eng. 132. Pp. 1 – 10.

Huang, S. et al. (2011a). Numerical scheme for riser motion calculation during 3D VIV simulation. J. Fluids Struct. 27, 947-961.

Huang, S. et al. (2011b). Drag amplification of long flexible riser models undergoing multi-mode VIV in uniform currents. J. Fluids Struct. 27, 342-353.

Huang. S. (2011) "CFD simulation of riser VIV". Ph. D. Thesis in Ocean Engineering. Texas A&M University.

Huber, F. (2008) "The first floating wind turbines". 2nd International Conference on Ocean Energy (ICOE 2008), 15th – 17th October 2008, Brest, France.

Humphries, J. A. and Walker, D.H. (1987) Vortex Excited Response of Large-Scale Cylinders in Shear Flow. Proc. 6th Int. Offshore Mechanics and Arctic Engineering Conf. Vol. 2, Houston, Texas, USA. ASME. 139 – 143.

Iberdrola (2014) https://www.iberdrola.com/press-room/news/detail/iberdrola-to-carry-out-tlpwind-r-d-project-with-scottish-university-of-strathclyde-1157660620141009

Iberdrola (2019) https://www.iberdrola.com/sustainability/offshore-wind-turbines-foundations

IDAE. (2011) "Plan de Energías Renovables 2011-2020".

International Renewable Energy Agency, IRENA (2019) https://www.irena.org/Statistics/View-Data-by-Topic/Capacity-and-Generation/Country-Rankings.

International Renewable Energy Agency, IRENA (2012): Renewable Energy Technologies: Costs Analysis Series. Wind Power. June 2012.

Jhingran, V. et al. (2008). Spatial variation of drag on long cylinders in sheared flow. OMAE2008-57803. In: Proceedings of the ASME 27th International Conference on Ocean, Offshore and Arctic Engineering. Estoril, Portugal.

Justesen, P. (1991). A numerical study of oscillation flow around a circular cylinder. J. of Fluid Mechanics 222, 157 – 196.

Khalak, A., Williamson, C.H.K. (1999). Motions, forces, and mode transitions in vortex-induced vibrations at low mass-damping. J. of Fluids and Structures. 13, 813-851.

La voz digital (2016), https://www.lavozdigital.es/cadiz/provincia/lvdi-regresa-carga-trabajo-dragados-contrato-eolico-201605300726_noticia.html.

La voz digital (2017), https://www.lavozdigital.es/cadiz/provincia/lvdi-dragados-offshore-ultima nuevo-contrato-eolico-germana-tennet-202008010804_noticia.html).

La voz digital (2020), https://www.lavozdigital.es/cadiz/provincia/lvdi-dragados-offshore-culmina-obra-otros-colosos-y-puja-nuevo-contrato-202003160720_noticia.html

Lehn, E. (2003) VIV Suppression Test on High L/D Flexible Cylinders. Norwegian Marine Technology Research Institute. Trondheim, Norway.

Leonard, A. and Roshko, A. (2001) Aspects of flow-induced vibration. J. of Fluids and Structures 15, 415 – 425.

Lie, H. and Kaasen, K.E., (2006). Modal analysis of measurements from a large-scale VIV model test of a riser in linerarly sheared flow. J. Fluids Struct. 22, 557-575.

Lothode, C. et al. (2015). Numerical study of VIV over a flexible riser. VI International Conference Computational Methods in Marine Engineering. Marine 2015.

Lucor, D., Imas, L. and Karniadakis, G.E. (2001). Vortex dislocations and force distributions of long flexible cylinders subjected to sheared flows. J Fluids Struct. 15: 651 – 658.

Marzouk, O.A. (2009) "Simulation, Modeling and Characterization of the Wakes of Fixed and Moving Cylinders". Ph.D. Thesis in Engineering Mechanics. Virginia Polytechnic Institute and State University.

Matha, D., Fischer, T., Kuhn, M, Jonkman, J. (2010) Model development and loads analysis of a wind turbine on a floating offshore tension leg platform. No. NREL/CP-500-46725.

Meneghini, J.R. et al. (2004). Numerical simulation of VIV on long flexible cylinders immersed in complex flow fields. Eur. J. Mech. B/Fluids 23, 51-63.

Menter, F.R. (1994). Two-equation eddy-viscosity turbulence models for engineering applications. AIAA Journal 32 (8), 1598-1605.

Menter, F.R. et al. (2006). Overview of fluid-structure coupling in ANSYS-CFX. OMAE2006-92145. In: Proceedings of the ASME 25th International Conference on Ocean, Offshore and Arctic Engineering. Hamburg, Germany.

Ministerio de Energía, Turismo y Agenda Digital, MINETAD (2017) "Primer Balance Energético Provisional 2016 y Perspectivas 2017". March 17th, 2017

Moon III, W.L. and Nordstrom, C.J. (2010) Tension-leg platform turbine: a unique integration of mature technologies. In: Proceedings of the 16th offshore symposium. Texas Section of the Society of Naval Architects and Marine Engineers, p. A25 – 34.

Newman, D. and Karniadakis, G.E. (1996). Simulations of flow over a flexible cable: a comparison of forced and flow-induced vibration. J. of Fluids and Structures, Vol. 10, 439-453.

Newman, D. and Karniadakis, G.E. (1997). A direct numerical simulation of flow past a freely vibrating cable. Journal of Fluid Mechanics, Vol. 334, 95-136.

Nihei, Y., Matsuura, M., Fujioka, H. and Suzuki, H. (2011) An approach for the optimum design of TLP type offshore wind turbines. In: Proceedings of the 30th international conference on ocean, offshore and arctic engineering, no. OMAE2011-50258.

NS Energy (2020): https://www.nsenergybusiness.com/projects/windfloat-atlantic-project/.

Offshore Mooring Lines (2020): http://dredgingengineering.com/moorings/lines/offshore mooring lines.

Oñate. E. (1992). Cálculo de estructuras por el Método de Elementos Finitos. Capítulo VII. CIMNE publications.

Pan, Z.Y., Cui, W.C., and Miao, Q.M. (2007) Numerical simulation of vortex-induced vibration of a circular cylinder at low mass-damping using RANS code. J. of Fluids and Structures 23, pp. 23 – 37.

Placzek, A., Sigrist, J.F. and Hamdouni, A. (2009) Numerical simulation of an oscillating cylinder in a cross-flow at low Reynolds number: Forced and free oscillations. Computers and Fluids 38, pp. 80 – 100.

Potanza, J. P., Chen, C.R. and Chen, H. C. (2004) "Chimera Reynolds averaged Navier-Stokes simulations of vortex-induced vibration of circular cylinders". Proceedings of the International ASCE Conference: Civil Engineering in the Oceans VI 166-176.

Potanza, J. P., Chen, C.R. and Chen, H. C. (2005a) "Simulations of high Reynolds number flow past arrays of circular cylinders undergoing vortex-induced vibrations", Proceedings of the 15th International Offshore and Polar Engineering Conference, Seoual, Korea.

Potanza, J.P., Chen, C.R. and Chen, H. C. (2005b) "Numerical simulations of riser vortex-induced vibrations", Proceedings of the 2005 Society of Marine Engineers and Naval Architects (SNAME) Conference, 52, 1-12

Potanza, J. P., Chen, H.C. and Reddy, J.N. (2005) "A local-analytic-based discretization procedure for the numerical solution of incompressible flows" Int. J. Numer. Meth.Fl., 49, 657-699.

Potanza, J.P. and Chen, H.C. (2007) "Three dimensional numerical simulations of circular cylinders undergoing two degree-of-freedom vortex-induced vibrations" J. Offshore Mech. Arct., 129(3) 158-164.

Rayleight 3rd baron of, "The aeolian harp" Phil. Mag. VII, pp. 149 –162, 1879

REE. (2018) "Informe anual de la energía en España".

Resvanis, T.L., et.al. (2012). Reynolds number effect on the vortex-induced vibration of flexible marine risers. Proceedings of the ASME 2012 31st International Conference on Ocean, Offshore and Arctic Engineering, OMAE2012 (OMAE2012-83565).

REVE (Revista Eólica y del Vehículo Eléctrico) (2019a): www.evwind.com/2019/06/02

REVE (Revista Eólica y del Vehículo Eléctrico) (2019b): https: //www. evwind.es/2019/05/31 /wind-energy-in-spain-first-offshore-wind-farm-project/67453

Robertson, A.N. and Jonkman, J.M. (2011) Loads analysis of several offshore floating wind turbine concepts. In: 21st International Offshore and Polar Engineering conference, no: NREL/CP-5000-50539.

Sachithanathamoorthy, K. (2012) "Design and Analysis of Tension Leg Anchor Systems for Floating Windmills". M. Sc. Thesis. Norwegian University of Science and Technology. Department of Marine Technology.

Saltara, F., Meneguini, J.R. and Siqueira, C.L.R. (1998) The Simulation of Vortex Shedding From and Oscillating Circular Cylinder. The 8th International Offshore and Polar Engineering Conference, 24 -29 May, Montreal, Canada.

Sarpkaya, T. (1979). Vortex-induced oscillations. J. Appl. Mech. 46, 241-258.

Sarpkaya, T. (2004). A Critical Review of the Intrinsic Nature of Vortex-Induced Vibrations. J. of Fluids and Structures 19(4), pp. 389 – 447.

Sclavoulus, P., Lee, S., DiPietro, J., Potenza, G., Caramuscio, P. and Michele, G.D. (2010) Floating offshore wind turbines: tension leg platform and taught leg buoy concepts supporting 3 – 5 MW wind turbines. In: European wind energy conference EWEC 2010, Warsaw, Poland.

Scrutton, C., (1955) Wind-excited oscillations of tall stacks. Engineer 199, 806 – 808.

Scrutton, C., (1956) Note on the Aerodynamic Stability of Truncated Circular Cones and Tapered Stacks. National Physical Laboratory, Teddington, UK.

Scruton, C., (1965) On the Wind-Excited Oscillations of Stacks, Towers and Masts. In: Conference Proceedings of 1963 National Physical Laboratory, Teddington, UK.

Shiels, D. Leonard, A. and Roshko, A. (2001) Flow-Induced Vibration of a Circular Cylinder at Limiting Structural Parameters. J. of Fluids and Structures. 15 pp. 3 – 21.

Skop, R.A. and Griffin, O. M. (1973) A Model for the Vortex-Excited Resonant Response of Bluff Cylinders. J. of Sound and Vibration, Vol. 27, pp. 225 – 233.

Stewart, G., Lackner, M., Robertson, A., Jonkman, J., and Goupee, A. (2012) Calibration and validation of a fast floating wind turbine model of the deepwind scaled tension-leg platform. In: 22nd Internationnal Offshore and Polar Engineering conference, no. NREL/CP-5000-54822.

Strouhal V., (1878) "Ueber eine besondere Art der Tonerregung" (On an unusual sort of sound excitation), *Annalen der Physik und Chemie*, 3rd series, **5** (10): 216–251.

Sun, L. Dong, J. Zong, Z. and Chen, W. (2012) Numerical simulation of flow around a cylinder of two degrees of freedom motion using the discrete vortex method. J. of Ship Mechanics.

The future of energy (2016) http://futureofenergy.web.unc.edu/2016/04/06/where-the-wind-blows-onshore-vs-offshore-wind-energy/

Tognarelli, M.A. et al. (2004). VIV response of a long flexible cylinder in uniform and linearly sheared currents. OTC 16338. In: Proceedings of the 2004 Offshore Technology Conference. Houston, USA.

Tognarelli, M.A. et al. (2008). Actual VIV fatigue response of full scale drilling risers: with and without suppression devices. OMAE2008-57046. In: Proceedings of the ASME 27th International Conference on Ocean, Offshore and Arctic Engineering. Estoril, Portugal.

Trim, A.D. at al. (2005). Experimental investigation on vortex-induced vibration of long marine risers. J. Fluids Struct. 21, 335-361.

Umemura, S., Yamaguchi, T., Shiraki, K. (1971) Vibration caused by Karman vortex on bridge members and its contermesdures. In: Proceedings of 3rd conference on wind effects on buildings and structures, Tokyo, pp. 747— 756.

University of Strathclyde: http://www.esru.strath.ac.uk/EandE/Web_sites/15-16/Floating_Windfarm_Installation

Vandiver, J.K. et al. (2006). The effectiveness of helical strakes in the suppression of high-mode-number VIV, OTC 18276. In: Proceedings of the 2006 Offshore Technology Conference. Houston, USA.

Vandiver, J.K. et al. (2009). Insights on vortex-induced, travelling waves on long risers. J. Fluids Struct. 25, 641-653.

Vickery, B.J. and Watkins, R.D. (1962) Flow-Induced Vibrations of Cylindrical Structures. University of Sydney, Australia. School of Civil Engineering. Research Report n. 34.

Wanderley, J.B.V., Souza, G.H.B., Saphier, S.H. and Levi, C. (2008). Vortex-induced vibration of an elastically mounted circular cylinder using an upwind TVD two-dimensional numerical scheme. Ocean Eng. 35, pp. 1533 – 1544.

Weaver, W., Timoshenko, S.P. and Young, D.H. (1974). Vibration Problems in Engineering. John Wiley & Sons. New York. USA.

Williamson, C.H.K. and Roshko, A. (1998) Vortex formation in the wake of an oscillating cylinder. J. Fluid Struct. 2: 355 – 381.

Williamson, C.H.K., Govardhan, R. (2004). Vortex-induced vibrations. Annual. Rev. Fluid Mech 36, 413-455.

Wincrete.com. (2015) Concrete Floating Turbine Economizes Wind Power.

Wu, X. et al. (2012). A review of recent studies on vortex-induced vibrations of long slender cylinders. J. Fluids Struct. 28, 292-308.

Xiao, Q. and Wang, E. (2016). Numerical simulation of vortex-induced vibration of a vertical riser in uniform and linearly sheared currents. Ocean Eng. 121, 492-515.

Xue, H. et al. (2015). A practical approach to predict cross-flow and in-line VIV response for deepwater risers. Appl. Ocean. Res. 52, 92-101.

Yamamoto, C.T., Meneguini, J.R., Saltara, F., Fregonesi, R.A., Ferrari, J.A. (2004). Numerical simulations of vortex-induced vibration on flexible cylinders. J. Fluids Struct. 19, pp 467 – 489.

Yang, Yi. "Experimental Investigations of Vortex Induced Vibration of a Flat Plate in Pitch Oscillation". M. Sc. Texas A. &M. University. December 2010.

Zhao, M. and Chen, L. (2011) Numerical simulation of two-degree-of-freedom vortex-induced vibration of a circular cylinder close to a plane boundary. J. of Fluids and Structures, Vol. 27, Issue 7, pp. 1097 – 1110.

Zhao, M., Chen, L., An, H. (2012). Numerical Investigation of Vortex-induced vibration of a circular cylinder in transverse direction in oscillatory flow. Ocean Engineering 41, 39 – 52.

Zhao, M., Chen, L., An, H. and Lu, L. (2014). Three-dimensional numerical simulation of vortex-induced vibration of an elastically mounted rigid circular cylinder in steady current. J. of Fluids and Structures, Vol. 50, pp. 292 – 311.

10. Appendix I

The expression of the stress tensor in the Navier-Stokes equation of motion.

The present explanation has been extracted from Batchelor (2000), sections 2.3 and 3.3. In a fluid at rest, only normal stresses are excited. The normal stress is independent of the direction of the normal to the surface element across which it acts, and the stress tensor has the form:

$$\sigma_{ij} = -p\delta_{ij} \qquad \text{I.1}$$

Where *p* is the static-fluid pressure.

But when the fluid flows the stress tensor σ_{ij} is the sum of the isotropic part $-p\delta_{ij}$ of the same form as the stress term in the fluid at rest and a remaining non-isotropic part d_{ij} that is due entirely to the existence of the motion of fluid. This non-isotropic tensor in named deviatoric stress tensor. Hence:

$$\sigma_{ij} = -p\delta_{ij} + d_{ij} \qquad \text{I.2}$$

That corresponds with eq 2.4.

There is no way of deducing the dependence of d_{ij} on the velocity gradients $\partial u_i/\partial x_j$ for fluids. Therefore, we fall back on the hypothesis that d_{ij} is approximately a linear function of the various components of these velocity gradients for sufficiently small magnitudes of those components. Analytically the hypothesis is expressed as:

$$d_{ij} = A_{ijkl}\frac{\partial u_k}{\partial x_l} \qquad \text{I.3}$$

Where A_{ijkl} is a fourth order tensor symmetrical in *I* and *j* like d_{ij}.

It is convenient at this point to write $\partial u_k / \partial x_l$ as a sum of its symmetrical part e_{kl} (the rate-of-strain tensor) and its antisymmetric part $-\frac{1}{2}\varepsilon_{klm}\omega_m$ (where ω is the vorticity) so former equation becomes:

$$d_{ij} = A_{ijkl}e_{kl} - \frac{1}{2}A_{ijkl}\varepsilon_{klm}\omega_m \qquad \text{I.4}$$

Let´s see how the tensor d_{ij} can be represented in the former way.

If we take the tensor of the velocity gradient in a certain point:

$$\partial u_i = \frac{\partial u_i}{\partial x_j}\, dx_j \qquad \text{I.5}$$

This can be decomposed in a symmetrical and a antisymmetric tensor. In matrix form eq. I.5 is represented as:

$$\begin{pmatrix} \partial u_i \\ \partial u_j \\ \partial u_k \end{pmatrix} = \begin{pmatrix} \frac{\partial u_i}{\partial x_i} & \frac{\partial u_i}{\partial x_j} & \frac{\partial u_i}{\partial x_k} \\ \frac{\partial u_j}{\partial x_i} & \frac{\partial u_j}{\partial x_j} & \frac{\partial u_i}{\partial x_k} \\ \frac{\partial u_k}{\partial x_i} & \frac{\partial u_k}{\partial x_j} & \frac{\partial u_k}{\partial x_k} \end{pmatrix} \begin{pmatrix} dx_i \\ dx_j \\ dx_k \end{pmatrix} \qquad \text{I.6}$$

But this can be decomposed in the following way:

$$\begin{pmatrix} \partial u_i \\ \partial u_j \\ \partial u_k \end{pmatrix} = \begin{pmatrix} \frac{1}{2}\left(\frac{\partial u_i}{\partial x_i} + \frac{\partial u_i}{\partial x_i}\right) & e_{ij} & e_{ik} \\ \frac{1}{2}\left(\frac{\partial u_i}{\partial x_j} + \frac{\partial u_j}{\partial x_i}\right) & e_{jj} & e_{jk} \\ \frac{1}{2}\left(\frac{\partial u_i}{\partial x_k} + \frac{\partial u_k}{\partial x_i}\right) & e_{kj} & e_{kk} \end{pmatrix} \begin{pmatrix} dx_i \\ dx_j \\ dx_k \end{pmatrix} + \begin{pmatrix} \frac{1}{2}\left(\frac{\partial u_i}{\partial x_i} - \frac{\partial u_i}{\partial x_i}\right) & \zeta_{ij} & \zeta_{ik} \\ \frac{1}{2}\left(\frac{\partial u_i}{\partial x_j} - \frac{\partial u_j}{\partial x_i}\right) & \zeta_{jj} & \zeta_{jk} \\ \frac{1}{2}\left(\frac{\partial u_i}{\partial x_k} - \frac{\partial u_k}{\partial x_i}\right) & \zeta_{kj} & \zeta_{kk} \end{pmatrix} \begin{pmatrix} dx_i \\ dx_j \\ dx_k \end{pmatrix} \qquad \text{I.7}$$

It can be observed that the first matrix represents a symmetric tensor as the elements are symmetric respect to the diagonal are the half sum of the same symmetric elements of the original matrix. The second matrix is antisymmetric, as $\zeta_{jj} = 0$ and $\zeta_{ij} = -\zeta_{ji}$

Finally, the antisymmetric tensor can be expressed as a determinant of the type:

$$\begin{vmatrix} i & j & k \\ \dfrac{\partial}{\partial x_i} & \dfrac{\partial}{\partial x_j} & \dfrac{\partial}{\partial x_k} \\ u_i & u_j & u_k \end{vmatrix} \qquad \text{I.8}$$

As, operating this determinant it can be observed that the components of the antisymmetric matrix are obtained.

And considering the definition of vorticity as:

$$\omega_i = \frac{\partial u_k}{\partial x_j} - \frac{\partial u_j}{\partial x_k} \qquad \text{I.9}$$

So finally, the expression I.4 is obtained.

Coming back to the equation I.4 and regarding the law of Cartesian tensor analysis: "all isotropic tensors of even order can be written as the sum of products of Kronecker delta tensors", then:

$$A_{ijkl} = \mu\, \delta_{ik}\delta_{jl} + \mu'\, \delta_{il}\delta_{jk} + \mu''\, \delta_{ij}\delta_{kl} \qquad \text{I.10}$$

Where μ, μ', μ'' are scalars and $\mu = \mu'$ due to symmetry in *i*, *j*.

Now A_{ijkl} I symmetrical in *k* and *l* also, and that, consequently, the term containing ω drops out of eq. I.4 giving:

$$d_{ij} = 2\mu e_{ij} + \mu''\, \Delta\delta_{ij} \qquad \text{I.11}$$

Where Δ denotes the rate of expansion $e_{kk} = \nabla \bullet u$

Finally, we recall that, by definition, d_{ij} makes zero contribution to the mean normal stress, then:

$$d_{ii} = (2\mu + 3\mu'')\Delta = 0 \qquad \text{I.12}$$

For all values of Δ. This development has been attributed to Boussinesq, Sauvier and others and it is an equivalent expression to eq. 2.9.

Hence:

$$2\mu + 3\mu' = 0 \quad \rightarrow \quad \mu' = \frac{2\mu}{3} \qquad \text{I.13}$$

Entering the value of μ' in d_{ij} equation:

$$d_{ij} = 2\mu(e_{ij} - \tfrac{1}{3}\Delta\delta_{ij}) \qquad \text{I.14}$$

Then eq. I.2 becomes:

$$\sigma_{ij} = -p\ \delta_{ij} + 2\mu\left(e_{ij} - \tfrac{1}{3}\Delta\delta_{ij}\right) \qquad \text{I.15}$$

With:

$$e_{ij} = \frac{1}{2}\left(\frac{\partial u_i}{\partial x_j} + \frac{\partial u_j}{\partial x_i}\right) \qquad \text{I.16}$$

And:

$$\Delta = e_{ii} \qquad \text{I.17}$$

Introducing σ_{ij} of eq. I.15 in the Navier-Stokes equation:

$$\rho\frac{Du_i}{Dt} = \rho F + \frac{\partial \sigma_{ij}}{\partial x_j} \qquad \text{I.18}$$

It is obtained the Navier-Stokes equation of motion:

$$\rho\frac{Du_i}{Dt} = \rho F_i - \frac{\partial P}{\partial x_i} + \frac{\partial}{\partial x_j}\left\{2\mu\left(e_{ij} - \tfrac{1}{3}\Delta\delta_{ij}\right)\right\} \qquad \text{I.19}$$